

# Prediction and characterisation of low-dimensional structures of antimony, indium and aluminium

---

**Mužević, Matko**

**Doctoral thesis / Disertacija**

**2019**

*Degree Grantor / Ustanova koja je dodijelila akademski / stručni stupanj:* **University of Zagreb, Faculty of Science / Sveučilište u Zagrebu, Prirodoslovno-matematički fakultet**

*Permanent link / Trajna poveznica:* <https://um.nsk.hr/um:nbn:hr:217:863639>

*Rights / Prava:* [In copyright](#)/[Zaštićeno autorskim pravom.](#)

*Download date / Datum preuzimanja:* **2025-01-24**



*Repository / Repozitorij:*

[Repository of the Faculty of Science - University of Zagreb](#)





University of Zagreb

FACULTY OF SCIENCE

Matko Mužević

**Prediction and characterisation of  
low-dimensional structures of  
antimony, indium and aluminium**

DOCTORAL DISSERTATION

Zagreb, 2019.



University of Zagreb

FACULTY OF SCIENCE

Matko Mužević

# Prediction and characterisation of low-dimensional structures of antimony, indium and aluminium

DOCTORAL DISSERTATION

Supervisors:

Associate Professor Igor Lukačević

Assistant Professor Sanjeev K. Gupta

Zagreb, 2019.



Sveučilište u Zagrebu

PRIRODOSLOVNO-MATEMATIČKI FAKULTET

Matko Mužević

**Predviđanje i karakterizacija  
nisko-dimenzionalnih struktura  
elemenata antimona, indija i aluminija**

DOKTORSKI RAD

Mentori:

izv. prof. dr. sc. Igor Lukačević

doc. dr. sc. Sanjeev K. Gupta

Zagreb, 2019.

## Supervisors' curriculum vitae

Igor Lukačević was born in Osijek, Croatia, on 10th March 1978. After high school he started to study Mathematics and Physics at the Josip Juraj Strossmayer University of Osijek, where he graduated. He has completed his PhD at the age of 29 years from University of Zagreb, Croatia, at the Faculty of Natural Sciences in the field of high-pressure material science. He is currently employed as the Associate Professor at the Josip Juraj Strossmayer University of Osijek, Croatia, Department of Physics, and carries out the duty of the Vice Head of Department of Physics for the scientific research activities. His newest interests are low-dimensional nano-materials and their applications in electronic, optical and green energy industry. He has over 20 publications that have been cited over 370 times, and his publication H-index is 9. He has been serving as a reviewer of several reputed Journals.

Dr. Sanjeev Gupta received his Ph.D in Condensed Material Physics from the M. K. Bhavnagar University, Bhavnagar, India in 2010, and spent time as a postdoctoral researcher at the Università di Modena e Reggio Emilia, Italy and Department of Physics, M. K. Bhavnagar University, Gujarat, India. He joined Dr. Pandey's group in 2012 as a Post Doctoral fellow, under the framework of Nehru-Fulbright Post-doc Fellowship. His current projects involve studying the electronic, structural, transport properties and Nano-bio hybrid systems using ab-initio methods. Gupta will help design advanced materials that can be future building blocks for solar cells, sensors, and energy harvesting and optoelectronic devices. He is currently the Assistant Professor in the department of physics and electronics at the St. Xavier's College, Ahmedabad, Affiliated with Gujarat University, Gujarat. He has over 160 peer reviewed publications that have been cited over 1000 times, and his publication H-index is 18. He has been serving as a reviewer of several reputed Journals.

# Contents

<b>Summary</b>	<b>vi</b>
<b>Sažetak</b>	<b>vii</b>
<b>Keywords</b>	<b>xii</b>
<b>Introduction</b>	<b>1</b>
<b>1 Theoretical background</b>	<b>4</b>
1.1 Born-Oppenheimer approximation . . . . .	4
1.2 Crystal structure . . . . .	7
1.2.1 Structural optimization . . . . .	8
1.3 Density functional theory (DFT) . . . . .	9
1.3.1 The Hohenberg-Kohn theorems . . . . .	9
1.3.2 Kohn-Sham approach . . . . .	10
1.3.3 Approximations for the exchange-correlation functional . . . . .	11
1.3.4 Solving Kohn-Sham equations . . . . .	12
1.3.5 Pseudopotentials . . . . .	14
1.3.6 Ab initio molecular dynamics . . . . .	15
1.4 Density functional perturbation theory (DFPT) . . . . .	16
1.4.1 Response function . . . . .	16
1.4.2 DFPT . . . . .	17
1.4.3 Phonons . . . . .	18
1.4.4 Elastic properties . . . . .	19
1.5 Dielectric function . . . . .	20
1.6 Computer codes . . . . .	21
1.6.1 Quantum ESPRESSO . . . . .	22
1.6.2 ABINIT . . . . .	22

<b>2</b>	<b>Two-dimensional crystal structures</b>	<b>23</b>
2.1	Description of crystal lattices . . . . .	23
2.1.1	Planar honeycomb . . . . .	23
2.1.2	Buckled honeycomb . . . . .	25
2.1.3	Planar triangular . . . . .	26
2.1.4	Puckered . . . . .	27
2.2	Results and discussion . . . . .	29
2.2.1	Relaxed structures . . . . .	29
2.2.2	Lattice dynamics . . . . .	34
<b>3</b>	<b>Strain engineering</b>	<b>39</b>
3.1	Types of strain in two-dimensional structures . . . . .	40
3.2	Results and discussion . . . . .	42
3.2.1	Stress-strain relations . . . . .	42
3.2.2	Lattice dynamics under strain . . . . .	45
<b>4</b>	<b>Substrates</b>	<b>51</b>
4.1	Results and discussion . . . . .	55
4.1.1	Structures on substrates . . . . .	55
4.1.2	Molecular dynamics on substrates . . . . .	60
<b>5</b>	<b>Characterization of predicted structures</b>	<b>63</b>
5.1	Electronic band structure . . . . .	63
5.2	Optical properties . . . . .	65
5.3	Elastic properties . . . . .	71
<b>6</b>	<b>Conclusions</b>	<b>74</b>
<b>A</b>	<b>Computational details</b>	<b>77</b>
A.1	Pseudopotentials . . . . .	77
A.2	Convergence . . . . .	78
<b>B</b>	<b>Indiene and aluminene in buckled and puckered allotropic modifications</b>	<b>80</b>
<b>C</b>	<b>Lattice dynamics under compressive strain</b>	<b>81</b>

<b>D Characterization of triangular structures</b>	<b>82</b>
D.1 Electronic band structure . . . . .	82
D.2 Optical properties . . . . .	83
<b>List of figures</b>	<b>88</b>
<b>List of tables</b>	<b>89</b>
<b>Bibliography</b>	<b>90</b>
<b>Curriculum vitae</b>	<b>97</b>



## **Acknowledgements**

Thank you to my supervisors, Associate Professor Igor Lukačević, for patience and help in research and with writing of this thesis, and Assistant Professor Sanjeev Kummar Gupta for help with research. Also, I would like to thank Assistant Professor Maja Varga Pajter for help with conducting research included inside this thesis.

Thank you to University Computing Centre of University of Zagreb (SRCE) and EPCC of University of Edinburgh for computational resources used in making of this thesis and their timely IT support.

Finally, thank you to my parents for 29 years of continued support. This is for you.

# Summary

Since the discovery of graphene, a new field of two-dimensional (2D) materials research has opened up, with different types of two-dimensional materials subfields. One such subfield are the monoelemental two-dimensional materials, in analogue to graphene, e.g. silicene, phosphorene and borophene. We study possible two-dimensional allotropes of antimony, indium and aluminium, called antimonene, indiene and aluminene, with structures chosen in analogue to other monoelemental two-dimensional materials due to the similarities in the valence electron configurations. Using density functional theory, lattice dynamics of structures are studied in a free-standing and strained forms. Some of the structures, such as  $\alpha$ -In and  $\alpha$ -Al, show stable lattice dynamics under imposed strain, giving hope for the experimental synthesis. As substrates are a critical component in synthesis of most two-dimensional materials, we have placed the proposed structures on the substrates Ag(111), Cu(111) and graphene. As lattice dynamics of antimonene allotropes are unstable under any imposed strain, interaction of the monolayer with the substrate is what stabilizes their structure. Our results for certain substrates are in agreement with experiment results for which allotrope forms on its surface. Potential substrates for experimental synthesis of  $\alpha$ -In and  $\alpha$ -Al are identified. We have obtained electronic band structures, optical and elastic properties of proposed materials. Electronic band structures, in part, confirm results of previous studies. Optical properties show similarities with other two-dimensional materials, such as strong anisotropy with regard to polarization of the incident electromagnetic wave. Elastic properties show similarities to other two-dimensional materials.

# Sažetak

Nove tehnologije ključ su civilizacijskog napretka, a jedan od temelja koji omogućava primjenu novih tehnologija su novi, poboljšani materijali. Poželjne karakteristike uređaja zasnovanih na novim materijalima su niža cijena izrade, manje dimenzije i bolja svojstva. Dvodimenzionalni materijali se ovdje pojavljuju kao nova vrsta materijala koja može ispuniti ove uvjete - manje dimenzije na očiti način, a nižu cijenu izrade barem što se tiče potrebnih sirovina.

Otkrićem grafena 2004. godine dolazi do eksplozije istraživanja dvodimenzionalnih materijala. Osim grafena, često su istraživani dihalkogenidi prijelaznih metala, od kojih je najpoznatiji  $\text{MoS}_2$ , a po uzoru na grafen, proučavane su i dvodimenzionalne strukture ostalih, sličnih elemenata. Kao posljedica istraživanja uspješno su sintetizirani silicen, germanen, fosforen, borofen, antimonen, i tinen. Dvodimenzionalni materijali pokazuju svojstva primjenjiva u elektroničkoj i optoelektroničkoj industriji, kao i mehanička svojstva različita (ponekad i egzotična) u odnosu na svoje volumne oblike. No, polje istraživanja dvodimenzionalnih materijala i dalje ima potencijala, jer nijedan materijal nema savršena svojstva i ne ispunjava sve zahtjeve razvoja tehnologija.

Antimon je već istraživani u dvodimenzionalnim oblicima te su eksperimentalno sintetizirane tri različite strukture. U svom niskodimenzionalnom obliku pokazuje iznimnu stabilnost u zraku, što daje nadu za njegovu primjenu u atmosferskim uvjetima. Prijašnja istraživanja niskodimenzionalnih oblika indija i aluminijska su malobrojna, no vodimo se primjerom bora, koji poprima dvodimenzionalne oblike, te zbog slične konfiguracije valentnih elektrona očekujemo da i ovi elementi imaju stabilne dvodimenzionalne strukture. Aluminijska niska cijena, reciklabilnost i niska specifična masa su motivacija za njegovo proučavanje, a indijska rasprostranjena uporaba u slitinama, poluvodičkim materijalima i premazima obećava raširenu primjenu u niskodimenzionalnom obliku.

U istraživanju smo koristili teoriju funkcionala gustoće, koja je već obilno korištena za

predviđanje još neotkrivenih dvodimenzionalnim materijala, kao i potvrdu eksperimentalnih rezultata. Prednost ovog teorijskog pristupa je svakako brzina proračuna. No, ono što ovom pristupu daje s jedne strane i prednost je što su kroz njega dostupni različiti uvjeti, strukture i veliki broj svojstava, što bi, s druge strane, u eksperimentalnom pristupu zahtjevalo velike financijske troškove i više vremena.

## Dvodimenzionalne kristalne strukture

Koristeći analogiju s drugim postojećim dvodimenzionalnim materijalima, pretpostavili smo da će moguće dvodimenzionalne strukture antimona, indija i aluminijske poprimiti jedan od četiri oblika. To su ravninska saćasta (Slika 2.1), označena kao  $\alpha$ , svijena saćasta (Slika 2.3), označena kao  $\beta$ , ravninska trokutasta (Slika 2.4), označena kao  $\gamma$ , i naborana (Slika 2.5), označena kao  $\delta$ . Nakon što su atomi antimona, indija i aluminijske stavljeni u pretpostavljene strukture, relaksacijom jedinične ćelije i položaja atoma (Tablica 2.1) dobiveno je da antimon poprima  $\alpha$ ,  $\beta$  i  $\delta$  strukturu, a indij i aluminij  $\alpha$  i  $\gamma$ . Za  $\beta$  i  $\delta$  oblike indija i aluminijske pokazano je da su dvoslojni  $\gamma$  strukture (Slika 2.8 i Dodatak B), odnosno, da indij i aluminij energetski ne podržavaju dvo-dimenzionalne strukture sastavljene od dva podsloja. Za sve strukture dobiveno je slaganje sa prijašnjim teorijskim rezultatima i eksperimentalnim veličinama, osim u slučaju  $\delta$ -Sb kod kojega se jedna od konstanti rešetke razlikuje za 4%. U skladu s nazivljem ostalih dvodimenzionalnih materijala, naše strukture nazivamo antimonen, indijen i aluminen.

Za dobivene strukture izračunate su fononske disperzije. Realne fononske disperzije nužan su preduvjet stabilnosti kristalne rešetke. Za  $\beta$ -Sb dobivene su realne fononske disperzije, što je u skladu s prijašnjim teorijskim istraživanjima, no kod  $\alpha$ -Sb i  $\delta$ -Sb u određenim smjerovima duž Brillouinove zone postoje imaginarne frekvencije (nestabilni fononski modovi). Naši rezultati za  $\delta$ -Sb nisu u skladu s prijašnjim istraživanjima, no razlike se javljaju zbog ranije spomenute razlike u konstantama rešetke.  $\alpha$ -In ima realne fononske disperzije, dok  $\alpha$ -Al posjeduje dva nestabilna fononska moda.  $\gamma$  strukture oba elementa imaju nestabilne fononske disperzije.

## Deformacija struktura i stabilnost

Deformacija je iznimno jednostavan način za moduliranje svojstava dvodimenzionalnih materijala te se u eksperimentima može na različite načine nametnuti na dvodimenzion-

alnu strukturu. Stoga je proučavan utjecaj deformacije na jediničnu ćeliju istraživanih struktura. Bilo koja deformacija u dvodimenzionalnim kristalima može se opisati deformacijom u *armchair* i *zigzag* smjeru. Homogena deformacija u svim smjerovima naziva se biaksijalna deformacija. Koristili smo izravnu deformaciju heksagonalne rešetke (Slika 3.3) što nije bio slučaj u prijašnjim istraživanjima. Ovakav pristup omogućio nam je konzistentnost pri promatranju utjecaja deformacije na slobodnu strukturu, posebno pri računanju fononskih disperzija. Također, velika prednost je manje trajanje simulacija u odnosu na pravokutne jedinične ćelije kakve su korištene u ostalim istraživanjima (nije potrebno povećavati broj atoma u jediničnoj ćeliji). Deformacija je simulirana u koracima od 2% od -20% do +40%. Dobivene su relacije odnosa naprezanja i deformacija (Slika 3.4) iz kojih su iščitane kritične deformacije,  $\varepsilon_{crit}$ , kao maksimum naprezanja (Tablica 3.1). Kritične deformacije su nam dale granične vrijednosti deformacije za koju bi se struktura mogla vratiti u izvorni, nedeformirani, oblik. Iznosi kritičnih deformacija razlikuju se od pojedinih ranije izračunatih vrijednosti, ali pokazuju anizotropnost i sličnu razinu anizotropije.

Izračunate su, također, i fononske disperzije deformiranih struktura. Deformacija uzrokuje promjenu u međusobnim udaljenostima između atoma unutar jedinične ćelije te time mijenja frekvenciju fonona. Fononske disperzije svih struktura za sažimajuće deformacije posjeduju imaginarne frekvencije pojedinih modova (Dodatak C). Sve strukture antimonena posjeduju imaginarne fononske frekvencije za bilo koji iznos deformacije, što ukazuje da deformacija kristalne rešetke nije čimbenik koji ju stabilizira, jer sve tri su eksperimentalno ostvarene. Za strukture indijena i aluminena dobivena su područja stabilnosti za određene iznose deformacije što ukazuje na mogućnost njihove eksperimentalne sinteze. Rezultati su sažeti na Slici 3.12.

## Supstrati

Pošto se deformacija javlja prirodno pri sintezi na supstratima, identificirane su metalne površine i drugi dvodimenzionalni materijali koji mogu poslužiti kao supstrat. Računi su konvergirani za Ag(111), Cu(111) i grafen. PdTe<sub>2</sub> kao supstrat je korišten samo u slučaju  $\alpha$ -Sb i  $\beta$ -Sb. Pri postavljanju dvodimenzionalne strukture na supstrat, javlja se *a priori* biaksijalna deformacija kristalne rešetke, no pošto se atomi relaksiraju u energetski najpovoljnije položaje, ova deformacija može poprimiti *armchair* ili *zigzag* karakter (Tablica

4.1).

Za strukture antimonena dobiveno je ponašanje u skladu s eksperimentalnim rezultatima. Na ravnim metalnim površinama,  $\beta$ -Sb prelazi u  $\alpha$ -Sb i posjeduje iste parametre rešetke. Obavljen je i pomoćni račun na  $\text{PdTe}_2$ , s neravnom površinom, na kojem  $\alpha$ -Sb prelazi u  $\beta$ -Sb. Ovi rezultati pokazuju da tip i izgled supstrata utječu na strukturu antimonena koja će se sintetizirati na njegovoj površini. Pri postavljanju  $\beta$ -Sb na grafen, on zadržava svoj  $\beta$  oblik. Postavljanje  $\delta$ -Sb na ranije spomenute supstrate daje različite oblike dvosloja  $\alpha$ -Sb i  $\beta$ -Sb.

Za  $\alpha$ -In i  $\alpha$ -Al identificirani su supstrati koji, u skladu s deformacijama koje vrše na njihovu kristalnu rešetku, mogu služiti kao supstrat za njihovu eksperimentalnu sintezu. U  $\alpha$ -In slučaju to su  $\text{Ag}(111)$ ,  $\text{Cu}(111)$  i grafen, a u  $\alpha$ -Al slučaju to su  $\text{Cu}(111)$  i grafen.

Simulacijama molekularne dinamike dvodimenzionalnih struktura na supstratima ispitana je njihova stabilnost na sobnoj temperaturi. One pokazuju termičko gibanje oko ravnotežnih položaja, bez raspadanja struktura na više različitih vremenskih skala, što je i potvrđeno i funkcijama radijalnih distribucija atoma (Slika 4.6).

## Karakterizacija

Izračunate su elektronska struktura vrpce (Slike 5.1 i 5.2), optička (Slike 5.3 - 5.7) i elastična svojstva (Tablica 5.1).  $\alpha$ -Sb i  $\beta$ -Sb pokazuju poluvodički karakter s procjepima od 1.31 eV i 0.06 eV. Isključivo p-orbitale pridonose najvišim stanjima valentne vrpce i najnižim stanjima vodljive vrpce. Sve  $\alpha$  strukture pokazuju metalni karakter. Rezultati se kvalitativno slažu s prijašnjim istraživanjima. Optička svojstva pokazuju anizotropnost ovisno o polarizaciji upadnog elektromagnetskog značenja, karakterističnu dvodimenzionalnim materijalima. Optička svojstva  $\alpha$ -In i  $\alpha$ -Al pokazuju aktivnost u optičkom dijelu spektra, poput većeg postotka refleksije nego slični dvodimenzionalni materijali. Elastična svojstva su slična ostalim dvodimenzionalnim materijalima, uz to da  $\alpha$ -Sb pokazuje izvanredno visok Poissonov omjer, dok  $\alpha$ -In niži nego ostali materijali. Razlike dolaze od različite karakteristike vezanja i jakosti vezanja. U slučaju  $\alpha$ -In radi se o vezi kovalentnije prirode i slabije jakosti, dok kod  $\alpha$ -Sb veza je više metalnog karaktera (Slika 5.7).

---

## Zaključak

Rezultati ove disertacije proširili su bazu poznatih dvodimenzionalnih materijala i predviđeli su eksperimentalne uvjete potrebne za njihovu sintezu - vrsta i simetrija korištenog supstrata, potrebna deformacija da bi se ostvarila stabilna dinamika kristalne rešetke i odgovarajuća temperatura na kojoj bi se mogla vršiti sinteza. Korištena je nova metoda deformacije kristalne rešetke kako bi istražili dinamičku stabilnost kristalne rešetke. Ispitana su strukturna svojstva i dana je karakterizacija novih potencijalnih dvodimenzionalnih struktura antimona, indija i aluminijskih. Za proširenje rezultata ove disertacije, potrebno je istražiti dodatne supstrate radi šireg izbora pri eksperimentalnoj sintezi, a njihove karakteristike bi se trebale ispitati nekima od kompleksnijih aproksimacija teorije funkcionala gustoće. Iako rezultati istraživanja daju nadu u eksperimentalnu sintezu ovih materijala, treba spomenuti njihovu tendenciju da oksidiraju u atmosferi. Za njihovu eventualnu primjenu, potrebno je istražiti načine njihove zaštite. Također, proučavanje niskodimenzionalnih oksida ovih elemenata je možda ključan korak u budućem istraživanju i njihovoj primjeni.

# Keywords

two-dimensional materials, antimony, indium, aluminium, density functional theory, strain engineering



# Introduction

New science and technology are the driving forces for the progress of human race. This is almost not to be contested, it seems logical enough - we can see the mankind's progress all around us and the world is much more different than, for example, one hundred years ago - mostly due to the breakthroughs in science and new technologies that follow from it. Since the dawn of the human race, new materials were what gave us the advantage over our competitors and against the force of nature. As a grim example, one could mention the introduction of iron smelting was what gave the figurative and literal edge to new civilizations, or, as newer, more positive example, the new materials for semiconductors that improve IT technology or new materials for solar cells that improve our capabilities of harvesting the almost infinite energy of the Sun.

The requirements of the modern world for new materials for potential applications are lower manufacturing costs, smaller dimensions (the everlasting need for miniaturization) and improved properties. So, the research should be focused to at least improve some of the, if not all the requirements. In the last 15 years, a new field of materials has developed - the field of low-dimensional materials - whose at least one dimension is degrees of magnitude smaller than the others. A subfield of low-dimensional materials are two-dimensional materials, whose third dimension is suppressed and consists of only a few layers or even one layer of atoms. Two-dimensional materials fulfil the first two conditions in a natural way. The smaller dimensions are obvious and lower manufacturing costs also, at least in the amount of raw material needed for their production. The third condition, improved properties, can be accounted for by modifying their structure with state-of-the-art theoretical and experimental procedures, if they do not possess them outright.

Since the first experimental realisation of single sheet of carbon atoms - graphene - two-dimensional materials have been subject to numerous scientific research, both theoretical and experimental. Two-dimensional materials present a door to interesting new physics,

---

but also have immense application potential.

Graphene was first obtained by Geim and Novoselov[1] in 2004 from graphite, with a simple method called micromechanical cleavage. Since then, new methods for obtaining graphene were developed, such as chemical vapour deposition (CVD), thermal decomposition of compounds, etc. Mechanical cleavage, however, remains one of the primary methods of obtaining high-quality graphene crystals. Graphene is known for its honeycomb lattice, in which every carbon atom is bound with three others. Since carbon contains four valence electrons, it undergoes  $sp^2$  hybridization to form strong  $\sigma$  in-plane bonds between them, while out-of-plane they are bound with weak  $\pi$  bonds. Graphene is a zero-gap semiconductor, with valence and conducting bands meeting at the K-point of the Brillouin zone. But, due to its unique linear dispersion around it, forming the so-called Dirac cones, the charge carriers have high velocities, on the order of  $10^6$  m/s [2]. Experimental measurements give many excellent properties of graphene, such as room-temperature electron mobility of  $2.5 \times 10^5$   $\text{cm}^2\text{V}^{-1}\text{s}^{-1}$ [3], Young's modulus of 1 TPa [4] and a very high thermal conductivity [5]. However, its zero-gap characteristics are a problem for applications in electronic devices.

Also belonging to the field of high-researched two-dimensional materials are transition metal dichalcogenides (TMDs), whose monolayer consists of a transitional metal atom (Mo, W, Pd etc.) layer sandwiched between two layers of chalcogen atoms (S, Se, Te). These monolayers are direct-gap semiconductors, and they can be used in transistors. Like graphene, they can be obtained by mechanical exfoliation from their bulk form, but they can also be obtained by other, chemical methods. They have direct band gap, strong spin-orbit coupling and applicable electronic and mechanic properties [6].

Due to the same valence configuration as carbon, other Group IV elements can possess allotropes in analogue to carbon. Silicon, germanium and tin two-dimensional allotropes, called silicene, germanene and stanene, have been predicted and synthesized[7–9]. Two-dimensional allotropes of other elements have also been found, like borophene[10], phosphorene[11] and antimonene[12].

Although various two-dimensional allotropes and materials have been predicted and acquired in the experiment, there is still much room for growth, given the still relatively new nature of the field and no material with ideal properties. Hence, there is place for new materials and their potential application. Inside this thesis, we focus on two dimensional

---

allotropes of antimony, indium and aluminium.

Two-dimensional antimony allotropes have already been experimentally acquired [13–16] and there has been research studying its electronic, optical and mechanical properties [17–19]. However, what remains unclear is what governs the antimonene synthesis and the preferred allotrope acquired, which we try to inspect in this thesis. Also, antimonene has showed remarkable stability in air, which promises potential use in every day situations.

Although boron two-dimensional allotropes have been found, the experimental realization still remains sparse [20]. Other elements of the boron group - aluminium and indium - have not been researched in great detail. Some theoretical studies exist and we will be drawing upon them in the remainder of this thesis, however, no conclusive results have been published on aluminium and indium two-dimensional allotropes. The basic motivation to study these two elements comes from the facts that aluminium is the most abundant metal in the Earth's crust. It is low cost, has recyclable nature and has lightweight characteristics, while indium is widely used in different alloys, semi-conducting materials and coatings, promising wide potential use of devices based on its two-dimensional allotropes.

The hypothesis of this thesis is that among the so far unconsidered elements of Group IIIA and VA, stable allotropic modifications of monolayer structures can be found. These structures should have elastic, electronic and optical properties which surpass or complement the properties of known monolayer materials. The studied materials are to be connected with applications in the electronic and optical industry through the insights into the ability to experimentally synthesize the studied structures. This thesis will expand on the knowledge of known mono-element two-dimensional structures which provides possibilities on their application in novel devices at the nanoscale.

In this thesis, using density functional theory (DFT) we focus on structural properties of antimony, indium and aluminium two-dimensional allotropes, their behaviour under strain and their structure on substrates, as well as their characteristics of identified allotropes. Density functional theory has been extensively used as an *ab initio* theoretical method for prediction of stable two-dimensional structures and verification of experimental results. However, as with any theoretical approach which uses approximations, one should be careful proceeding with results acquired, as they depend on the level of theory and pseudopotentials used.

# Chapter 1

## Theoretical background

### 1.1 Born-Oppenheimer approximation

We are presented with a system of nuclei and electrons in some arrangement. What we would like to do is find the states and energies of the given system. The Hamiltonian is given by

$$\begin{aligned} \hat{H} = & -\frac{\hbar^2}{2m_e} \sum_i \nabla_i^2 - \frac{1}{4\pi\epsilon_0} \sum_{i,I} \frac{Z_I e^2}{|\mathbf{r}_i - \mathbf{R}_I|} + \frac{1}{8\pi\epsilon_0} \sum_{i \neq j} \frac{e^2}{|\mathbf{r}_i - \mathbf{r}_j|} \\ & - \frac{\hbar^2}{2M_I} \sum_I \nabla_I^2 + \frac{1}{8\pi\epsilon_0} \sum_{I \neq J} \frac{Z_I Z_J e^2}{|\mathbf{R}_I - \mathbf{R}_J|} , \end{aligned} \quad (1.1)$$

where electrons and nuclei are denoted by uncapitalized and capitalized subscripts, respectively. The first and the fourth terms are the kinetic energies of electrons and nuclei, respectively, second is the Coulomb interaction between the electrons and the nuclei and the remaining two terms are the Coulomb electron-electron and nuclei-nuclei interaction. The wavefunction of the system is given by the stationary Schrödinger's equation:

$$\hat{H}\psi = E\psi , \quad (1.2)$$

which is, but for the simplest of cases, unsolvable. From here on out, we will be using Hartree atomic units where  $\hbar = e = m_e = 4\pi\epsilon_0 = 1$ .

As the mass of the nuclei is orders of magnitude larger than the mass of the electrons, nucleonic motion, from the electron point of view, appears frozen. With that in mind, in (1.1), the kinetic energy of the nuclei,

$$\hat{T}_N = \frac{1}{2M_I} \sum_I \nabla_I^2 , \quad (1.3)$$

can be considered "small" relative to the other terms, so we can treat it as an perturbation:

$$\hat{H} = \hat{H}_{e,n} + \hat{T}_n . \quad (1.4)$$

The unperturbed part,  $\hat{H}_{e,n}$ , only depends on  $\mathbf{R}_I$  (the position of the nuclei) parametrically. Ignoring the kinetic nuclear part, hamiltonian for electrons of the starting system is:

$$\hat{H} = \hat{T} + \hat{V}_{ee} + \hat{V}_{en} + E_{nn} , \quad (1.5)$$

where  $\hat{T}$  is kinetic energy operator of the electrons

$$\hat{T} = \frac{1}{2} \sum_i \nabla_i^2 , \quad (1.6)$$

$\hat{V}_{ee}$  is the electron-electron interaction

$$\hat{V}_{ee} = \frac{1}{2} \sum_{i \neq j} \frac{1}{|\mathbf{r}_i - \mathbf{r}_j|} , \quad (1.7)$$

$\hat{V}_{en}$  is the electron-nuclei interaction, which in the exact case is the Coulumb interaction, but also can be expressed as a fixed potential acting on the electrons of the system

$$\hat{V}_{en} = \sum_{i,I} V_I(|\mathbf{r}_i - \mathbf{R}_I|) , \quad (1.8)$$

and  $E_{nn}$  is the nuclei-nuclei interaction that only contributes to the total energy of the system but does not influence our quantum mechanical description of the electrons. For the purpose of finding the solution to (1.2) it can be neglected and added later.

We are left with a form of hamiltonian that is called the electronic hamiltonian:

$$\hat{H}_e = \hat{T} + \hat{V}_{ee} + \hat{V}_{en} . \quad (1.9)$$

Its solution gives us the electronic wavefunctions  $\psi_e$  which are functions of electronic coordinates  $\mathbf{r}_i$ , but are parametrically dependent on the positions of the nuclei  $\mathbf{R}_I$  - meaning that changing the coordinates of the nuclei changes the form of  $\psi_e$ . Inserting (1.9) into (1.2) instead of full  $\hat{H}$

$$\hat{H}_e \psi_e = E_e \psi_e \quad (1.10)$$

gives us the electronic energy -  $E_e$  - in some outer potential  $\hat{V}_{en}$  due to the nuclei. Adding back the  $E_{nn}$ , we acquire the total energy of the system

$$E_{tot} = E_e + E_{nn} \quad (1.11)$$

for a given set of nuclei positions  $\mathbf{R}_I$ .

Now we go back to the full hamiltonian of the system, (1.1). Looking at electronic motion from the nuclei point of view, it is orders of magnitude greater than nucleonic motion. What nuclei "see" is the average of the electronic motion and it is reasonable to replace all the electronic contributions in (1.1) by their average over the electronic wavefunction  $\psi_e$

$$\begin{aligned} \hat{H} = & \left\langle -\frac{1}{2} \sum_i \nabla_i^2 - \sum_{i,I} \frac{Z_I}{|\mathbf{r}_i - \mathbf{R}_I|} + \frac{1}{2} \sum_{i \neq j} \frac{1}{|\mathbf{r}_i - \mathbf{r}_j|} \right\rangle, \\ & - \frac{1}{2M_I} \sum_I \nabla_I^2 + \frac{1}{2} \sum_{I \neq J} \frac{Z_I Z_J}{|\mathbf{R}_I - \mathbf{R}_J|} \end{aligned} \quad (1.12)$$

which is nothing other than electronic energy  $E_e$  and together with the last term (which produces  $E_{nn}$ )

$$\hat{H} = -\frac{1}{2M_I} \sum_I \nabla_I^2 + E_e + E_{nn}, \quad (1.13)$$

we acquire the hamiltonian for the nucleonic motion

$$\hat{H} = -\frac{1}{2M_I} \sum_I \nabla_I^2 + E_{tot}(\mathbf{R}_I), \quad (1.14)$$

where we have written dependence of the  $E_{tot}$  on  $\mathbf{R}_I$  explicitly. (1.14) gives us the motion of the nuclei in a potential formed by solving the electronic motion.

## Molecular dynamics

If we treat the problem of nucleonic motion classically, we can write

$$M_I \frac{\partial^2 \mathbf{R}_I}{\partial t^2} = \mathbf{F}_I(\mathbf{R}) = -\frac{\partial}{\partial \mathbf{R}_I} E(\mathbf{R}). \quad (1.15)$$

To acquire the motion of nuclei, we can use a numerical solution to the above equation using discrete time steps, such as the Verlet algorithm or any other type numerical solution to a differential equation. Using the Verlet algorithm, positions of nuclei at the next time instance,  $t + \Delta t$  (where  $\Delta t$  is the time step) depend on the forces in the present time step

$$\mathbf{R}_I(t + \Delta t) = 2\mathbf{R}_I(t) + \mathbf{R}_I(t - \Delta t) + \frac{(\Delta t)^2}{M_I} \mathbf{F}_I\{\mathbf{R}_I(t)\}. \quad (1.16)$$

In the above equation, the second derivative with respect to time was replaced with an approximation

$$f''(x) \approx \frac{f(x+h) - 2f(x) + f(x-h)}{h^2}. \quad (1.17)$$

The correct forces on nuclei are determined by the electronic motion and nucleonic positions, so correct solution to electronic motion is necessary for obtaining the correct nucleonic motion.

What was presented here was qualitative description of finding a solution for a given system of atoms. There are different ways of finding the solution to electronic problem and consequently the full state of the system, but the one that will be used in the scope of this thesis is the density functional theory (DFT).

## 1.2 Crystal structure

The crystal structure is determined by a primitive cell, together with positions of atoms inside of it, called the basis, and a set of translations that produce the periodicity. The set of all translations forms a lattice in space (Bravais lattice) and any translation can be written as integral multiples of the primitive cell vectors  $\mathbf{a}_1, \mathbf{a}_2, \dots$

$$\mathbf{T}(n_1, n_2, \dots) = n_1 \mathbf{a}_1 + n_2 \mathbf{a}_2 + \dots \quad (1.18)$$

With each lattice there is an associated reciprocal lattice, defined (in 3D) as

$$\mathbf{b}_i = 2\pi \frac{\mathbf{a}_j \times \mathbf{a}_k}{|\mathbf{a}_i(\mathbf{a}_j \times \mathbf{a}_k)|}, \quad (1.19)$$

where  $i, j, k$  are cyclical permutations of coordinates. Primitive cell in reciprocal space is called the first Brillouin zone. For a crystal that possesses translational symmetry, the Bloch theorem allows for eigenstates of translation operators to differ from one cell to another only by a phase factor

$$\mathbf{T}\psi(\mathbf{r}) = e^{i\mathbf{k}\cdot\mathbf{T}}\psi(\mathbf{r}), \quad (1.20)$$

where  $\mathbf{k}$  is any wavevector inside the Brillouin zone. Applying it to Schrödinger's equation for a system with a periodic Hamiltonian, like a crystal, we can further use the Bloch theorem to write

$$\psi_{\mathbf{k}}(\mathbf{r}) = e^{i\mathbf{k}\cdot\mathbf{r}} u_{\mathbf{k}}(\mathbf{r}), \quad (1.21)$$

where  $u_{\mathbf{k}}$  is a periodic function with the same periodicity as the crystal.

For a large enough volume, i.e. macroscopic crystal,  $\mathbf{k}$  values become continuous. The Hamiltonian is defined for each  $\mathbf{k}$  and by solving it we get discrete eigenstates

$$\psi_{i,\mathbf{k}}(\mathbf{r}) = e^{i\mathbf{k}\cdot\mathbf{r}} u_{i,\mathbf{k}}(\mathbf{r}), \quad (1.22)$$

with eigenvalues  $\epsilon_{i,\mathbf{k}}$ . The eigenvalues  $\epsilon_{i,\mathbf{k}}$  form what is called energy bands - with possibility that there exists a range of energies that have no associated states, for any  $\mathbf{k}$ , called energy gaps.

For certain properties of the crystal, like total energy, a sum over all  $\mathbf{k}$  states is needed. For a general function  $f_i(\mathbf{k})$ , where  $i$  is a set of discrete states at a certain  $\mathbf{k}$  the average value per cell is

$$\bar{f}_i = \frac{1}{N_k} \sum_{\mathbf{k}} f_i(\mathbf{k}), \quad (1.23)$$

where  $N_k$  is the number of  $\mathbf{k}$  values. With  $N_k$  going to infinity, the sum becomes an integral of the form

$$\bar{f}_i = \frac{1}{\Omega_{BZ}} \int_{BZ} d\mathbf{k} f_i(\mathbf{k}), \quad (1.24)$$

where  $\Omega_{BZ}$  is the volume of the Brillouin zone. In practice we choose a discrete set of points for the approximation of this integral. A general method proposed by Monkhorst and Pack gives a uniform set of points given by [21]

$$\mathbf{k}_{n_1, n_2, n_3} = \sum_i^3 \frac{2n_i - N_i - 1}{2N_i} \mathbf{b}_i. \quad (1.25)$$

A grid defined as above has useful properties, such as being offset from the points  $\mathbf{k} = 0$  and, if chosen to be even, omits the high-symmetry points.

### 1.2.1 Structural optimization

In a periodic crystal, the optimized structure is given by the vectors of the unit cell and positions of the atoms inside it. The equation (1.14) gives us the Hamiltonian for nucleonic motion. By finding the minima of the potential surface we obtain the optimized structure of the system. From the Hellman-Feynman theorem [22], forces on the nuclei can be obtained by

$$\mathbf{F}_I = -\frac{\partial E}{\partial \mathbf{R}_I}, \quad (1.26)$$

where  $E$  is the total energy and  $\mathbf{R}_I$  are the positions of the nuclei. By finding a configuration where the forces on atoms are zero, we in principle arrive at the optimized structure. Since this is a calculation problem in parameter space of  $\{\mathbf{R}_I\}$  ( $3N$  variables), specialized algorithms are used for structure optimizations. In this thesis, we have used the BFGS algorithm developed by Broyden, Fletcher, Goldfarb and Shanno [23] implemented inside the used computer code.



## 1.3 Density functional theory (DFT)

The usual method of dealing with quantum mechanical problems is solving the Schrödinger's equation for some potential  $\hat{V}$  and acquiring wavefunctions  $\psi_n$  of the system as the eigenfunctions of the hamiltonian. If our problem dealt with a system of electrons, for example like in (1.9), hamiltonian depends on electron coordinates,  $\mathbf{r}_i$ , the number of which is  $3N$ , where  $N$  is the number of electrons. From that set of eigenfunctions, the one with the lowest energy is the ground state  $\psi_0(\mathbf{r}_i)$  and using it, we can find different properties of the system, including the ground state density  $n_0(\mathbf{r})$ .

What density functional theory proposes is solving the problem in terms of electron density  $n(\mathbf{r})$ , and reducing the number of variables from  $3N$  to only 3.

### 1.3.1 The Hohenberg-Kohn theorems

The Hohenberg-Kohn theorems deal with many-body interacting systems, such as the one from 1.9. We can write hamiltonian of such a system in general as

$$\hat{H} = -\frac{1}{2} \sum_i \nabla_i^2 - \sum_i V_{ext}(\mathbf{r}_i) + \frac{1}{2} \sum_{i \neq j} \frac{1}{|\mathbf{r}_i - \mathbf{r}_j|}, \quad (1.27)$$

where  $V_{ext}$  is some kind of external potential acting on the electrons of the system. Theorems are stated as follows[24]:

**Theorem I** - For any system of interacting particles in an external potential  $V_{ext}(\mathbf{r})$ , the  $V_{ext}(\mathbf{r})$  is determined uniquely, except for a constant, by the ground state particle density  $n_0(\mathbf{r})$ .

**Theorem II** - A universal functional for the energy  $E[n]$  in terms of the density  $n(\mathbf{r})$  can be defined, valid for any external potential  $V_{ext}(\mathbf{r})$ . For any particular  $V_{ext}(\mathbf{r})$ , the exact ground state energy of the system is the global minimum value of this functional, and the density  $n(\mathbf{r})$  that minimizes the functional is the exact ground state density  $n_0(\mathbf{r})$ .

The proof to both is simple and can be found in original paper by Hohenberg and Kohn [25]. What follows from the theorems is that since the ground state density  $n_0(\mathbf{r})$  determines the external potential  $V_{ext}(\mathbf{r})$ , the hamiltonian of the system is also determined,

and from hamiltonian *all* of the wavefunctions follow, meaning that ground state density  $n_0(\mathbf{r})$  also determines all the properties of the system. Also, the functional  $E[n]$  is enough to determine the ground state density  $n_0(\mathbf{r})$  of the system. The total energy functional is given by

$$E[n] = T[n] + E_{int}[n] + \int d^3r V_{ext}(\mathbf{r})n(\mathbf{r}) + E_{nn} \quad (1.28)$$

and finding it's minimum in respect to density  $n(\mathbf{r})$  gives us the ground state density  $n_0(\mathbf{r})$ .

### 1.3.2 Kohn-Sham approach

In principle, (1.28) gives us a way to find the ground state density  $n_0(\mathbf{r})$  of the system. What it does not answer is how we extract any meaningful information from it - like we could from the wavefunction of the system. Also, multi-body interacting systems are difficult to solve. To deal with this problem, we assume that there exists a non-interacting system of particles with the same ground state density  $n_0(\mathbf{r})$  as the starting system - finding solution to such a system gives us the properties of the fully interacting system because they share the same ground state density  $n_0(\mathbf{r})$ .

The energy functional (1.28) is rewritten as

$$E_{KS} = -\frac{1}{2} \sum_i \langle \psi_i | \nabla^2 | \psi_i \rangle + \frac{1}{2} \int d^3r d^3r' \frac{n(\mathbf{r})n(\mathbf{r}')}{|\mathbf{r} - \mathbf{r}'|} + \int d^3r V_{ext}(\mathbf{r})n(\mathbf{r}) + E_{nn} + E_{xc}[n], \quad (1.29)$$

with

$$n(\mathbf{r}) = \sum_i |\psi_i(\mathbf{r})|^2, \quad (1.30)$$

where  $\psi_i$  are the wavefunctions of the non-interacting electrons.

In (1.29) the first term is the kinetic energy of non-interacting electrons  $T_s[n]$ , second term is the Coulomb interaction of the density with itself (called Hartree energy). The third term is the energy of electrons in the potential of the nuclei and the fourth is the energy of the nuclei-nuclei interaction. The fifth term is called the exchange-correlation energy, incorporating both Hartree-Fock exchange of electrons with the same spin, as well as correlated motion of electrons due to Pauli exclusion principle[26]. Finding the minimum of the new energy functional brings us to Schrödinger-like set of equations for  $\psi_i$  called Kohn-Sham[27] equations:

$$H_{KS} \psi_i = \epsilon_i \psi_i, \quad (1.31)$$

where  $H_{KS}$  is the effective hamiltonian of the electrons

$$H_{KS} = -\frac{1}{2}\nabla^2 + V_{ext}(\mathbf{r}) + V_{Hartree}(\mathbf{r}) + V_{xc}(\mathbf{r}) . \quad (1.32)$$

All the terms in (1.32) are well defined except the final -  $V_{xc}(\mathbf{r})$  - and quality of our solution to Kohn-Sham equations will depend on the right description or approximation of the exchange-correlation effects.

### 1.3.3 Approximations for the exchange-correlation functional

#### Local-density approximation (LDA)

We get the simplest form for exchange-correlation effects by making an assumption that it only depends on the density at a certain point (local density). Writing

$$E_{xc}^{LDA}[n] = \int d^3r \epsilon_{xc}(n) n(\mathbf{r}) , \quad (1.33)$$

where  $\epsilon_{xc}$  is the exchange-correlation energy per particle, we get the exchange-correlation energy depending only on the form of  $\epsilon_{xc}$ . The local dependence can be written in many ways, but for LDA it is usually taken as the exchange-correlation energy per particle of homogeneous electron gas -  $\epsilon_{xc}^{HEG}$  - which can be separated into independent terms for exchange and correlation:

$$\epsilon_{xc}^{HEG} = \epsilon_e + \epsilon_c . \quad (1.34)$$

Exchange energy per particle for homogeneous electron gas is know explicitly, and given with

$$\epsilon_x = -\frac{3}{4\pi} \left(\frac{9\pi}{4}\right)^{1/3} r_s^{-1} , \quad (1.35)$$

where  $r_s$  is parameter describing the density of the system, given as a radius of the sphere containing a single electron

$$\frac{4\pi}{3} r_s^3 = \frac{1}{n} . \quad (1.36)$$

Correlation energy can only be given approximately [Ref].

#### Generalized gradient approximations - GGA

Further step in improving our approximation is including the dependence of the exchange-correlation energy on the changes in the density at a certain point - it's gradient:

$$E_{xc}^{GGA}[n] = \int d^3r \epsilon_{xc}(n, \vec{\nabla}n) n(\mathbf{r}) \quad (1.37)$$

with

$$\epsilon_{xc} = \epsilon_x^{HEG} F_{xc}, \quad (1.38)$$

where  $F_{xc}$  is dimensionless function of the density gradient. The form of this function is not given exactly and depends on the type of the generalized gradient approximation used, like PW91[28] or PBE[29].

### Further improvements of XC approximations

For materials with localized and strongly interacting electrons, often an additional orbital-dependant interaction term is introduced, with the form same as the Hubbard model [30]. Such approach is called "DFT+U" and it improves on the the results of LDA and GGA calculations (such as the band gap of materials) of strongly correlated systems such as transition metal oxides.

Although not used in the research present in this thesis, there are further ways to enhance the exchange-correlation energy functional. The next "logical step" could be including dependence on higher gradients of density, going by the name of meta-GGA. Also, combining DFT expression for the exchange-correlation with a term calculated using Hartree-Fock theory produces the so-called "hybrid functionals", with the mixing of different contributions depending on the type of functional used [31].

### 1.3.4 Solving Kohn-Sham equations

Now we approach the solving of Kohn-Sham equations

$$\left[ -\frac{1}{2}\nabla^2 + V_{eff}(\mathbf{r}) \right] \psi_i(\mathbf{r}) = \epsilon_i \psi_i(\mathbf{r}) \quad (1.39)$$

with

$$V_{eff}(\mathbf{r}) = V_{ext}(\mathbf{r}) + V_{Hartree}(\mathbf{r}) + V_{xc}(\mathbf{r}) \quad (1.40)$$

being the effective potential acting on the electrons. Assuming we choose  $V_{xc}(\mathbf{r})$ , we start by making an initial guess of the density of the system  $n(\mathbf{r})$ . We calculate the effective potential in the system, (1.40) and use it to solve the set of Kohn-Sham equations (1.39). Once  $\psi_i$  are calculated, we calculate the electron density

$$n(\mathbf{r}) = \sum_i |\psi_i(\mathbf{r})|^2 \quad (1.41)$$

and then check the self-consistency, i.e. test if the density differs from the initial guess (to a chosen degree of precision). If the solution is not self-consistent, we take the output density as our new initial guess and repeat the calculation. The loop is done until the self-consistency is reached. Once we find a self-consistent solution, one can proceed to calculating physical quantities of the system. The algorithm is shown in Fig. 1.1.

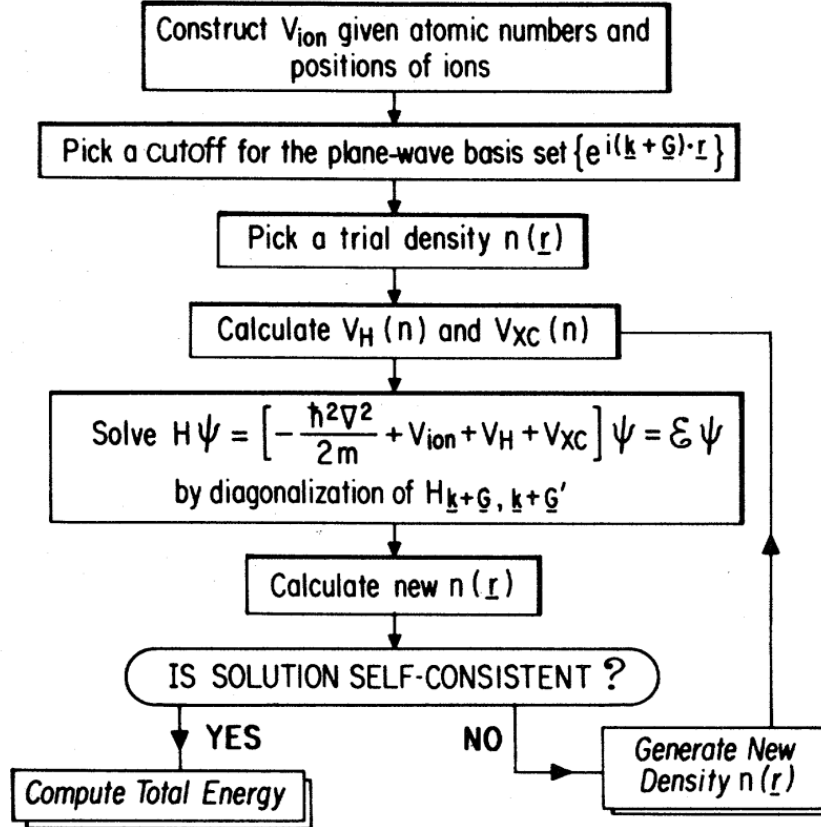


Figure 1.1: Algorithm for iterative self-consistent solution to Kohn-Sham equations. Taken from reference [32].

### Plane wave basis

If we perform a Fourier transform of  $u_{i,\mathbf{k}}(\mathbf{r})$  from 1.22, we get

$$u_{i,\mathbf{k}}(\mathbf{r}) = \sum_m c_{i,m} e^{i\mathbf{G}_m \cdot \mathbf{r}}, \quad (1.42)$$

where  $\mathbf{G}_m$  are wavevectors in reciprocal space with integer number periodicity of the crystal. Inserting it back to 1.22, we get

$$\psi_{i,\mathbf{k}}(\mathbf{r}) = \sum_m c_{i,m} e^{i(\mathbf{G}_m + \mathbf{k}) \cdot \mathbf{r}}. \quad (1.43)$$

In principle, the sum in above equation is infinite, but for all practical purposes a cut-off energy is chosen, such that the expansion in (1.43) satisfies some chosen degree of precision.

### 1.3.5 Pseudopotentials

Broadly speaking, we can separate electrons in atoms into two categories - tightly bounded inner electrons ("core") and outer, more loosely bounded electrons ("valence"). In general, bonding of molecules or solids is done through the interactions between valence electrons. Also, the true valence wavefunctions are extremely oscillatory near the core (having a large amount of nodes), to ensure the orthogonality with core wavefunctions. To ensure accurate enough expansion of wavefunctions, a lot of plane waves have to be included in the basis (1.43), increasing the complexity of calculation.

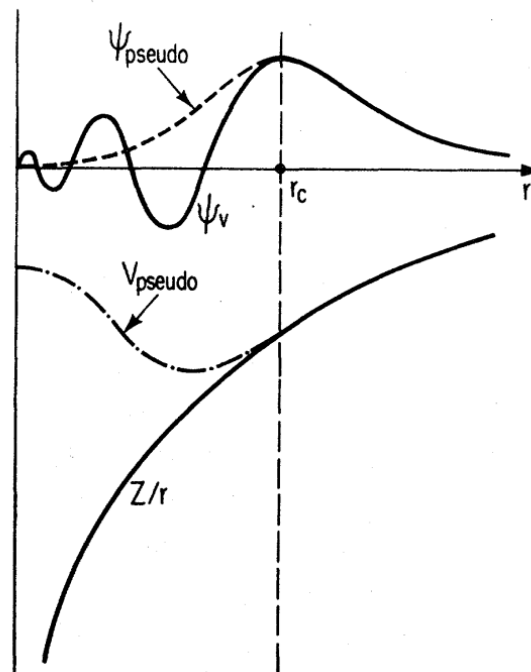


Figure 1.2: Illustration of an all-electron wavefunction and potential (solid lines) and pseudowavefunction and pseudopotential (dashed lines). Radius beyond which they match is designated with  $r_c$ . Taken from reference [32].

The aim of pseudopotentials is to simplify the electronic problem by dealing with both issues - by only including the valence electrons and replacing their Coulomb interaction

with the nucleus and inner electrons with an effective potential (the frozen core approximation) while also "smoothing out" their form near the core. Pseudopotentials replace the all-electron wavefunctions with pseudo-wavefunctions which match beyond some core cutoff radius  $r_c$  to ensure right kind of behaviour in the space between atoms where most of bonding and physical properties take shape, while differing inside where the exact physical description is not necessary (Fig. 1.2).

Details on the types of pseudopotentials used in our calculations are shown in Appendix A.

### Norm-conserving pseudopotentials

Norm-conserving pseudopotentials are characterized by the norm-conserving condition which demands that both the radial all-electron wavefunction and pseudo-wavefunction integrate to the same amount of charge in the chosen core radius  $r_c$

$$Q = \int_0^{r_c} dr r^2 |\psi(r)|^2 = \int_0^{r_c} dr r^2 |\psi^{PS}(r)|^2 . \quad (1.44)$$

Beyond the cutoff radius  $r_c$  all-electron and pseudo valence wavefunctions have to match, with their eigenvalues also being the same. Also, the logarithmic derivatives of all-electron and pseudo wavefunctions have to agree at  $r_c$ .

### Ultrasoft pseudopotentials

Ultrasoft pseudopotentials relax the norm-conserving condition (1.44) by adding auxiliary functions around ion cores which take into account the oscillatory character of all-electron wavefunctions. This allows for increased smoothness of the pseudowavefunctions, reducing the complexity of calculation, but increasing the accuracy to some extent.

## 1.3.6 Ab initio molecular dynamics

Within the Born-Oppenheimer approximation, also called the adiabatic approximation, the electrons stay in their instantaneous ground state as the nuclei move. The total energy of the system of electrons and nuclei, within the Kohn-Sham approach is

$$E[\{\psi_i\}, \{R_I\}] = 2 \sum_{i=1}^N \int \psi_i^*(\mathbf{r}) \left( -\frac{1}{2} \nabla^2 \right) \psi_i(\mathbf{r}) d\mathbf{r} + E_e[n] + E_{nn}[\{R_I\}] , \quad (1.45)$$

where

$$E_e[n] = \frac{1}{2} \int d\mathbf{r} d\mathbf{r}' \frac{n(\mathbf{r})n(\mathbf{r}')}{|\mathbf{r} - \mathbf{r}'|} + \int d\mathbf{r} V_{ext}(\mathbf{r})n(\mathbf{r}) + E_{xc}[n]. \quad (1.46)$$

The forces on the nuclei are then obtained using the Hellman-Feynman theorem, here repeated as

$$\mathbf{F}_I = -\frac{\partial E}{\partial \mathbf{R}_I}. \quad (1.47)$$

When forces on nuclei are known, the molecular dynamics (movement of nuclei) are solved with (1.16) or a similar method for solving differential equations. We have used exactly Verlet algorithm for nucleonic motion.

## 1.4 Density functional perturbation theory (DFPT)

### 1.4.1 Response function

If the strength of some small perturbation to the hamiltonian is described by the parameter  $\lambda$ , we can expand the energy, potential or the wavefunctions of the system in terms of  $\lambda$ , i.e.

$$E = E^{(0)} + \lambda E^{(1)} + \lambda^2 E^{(2)} + \dots, \quad (1.48)$$

where

$$E^{(n)} = \frac{1}{k!} \frac{d^k E}{d\lambda^k}. \quad (1.49)$$

The first order corrections to the wavefunctions of the system are given by

$$\Delta\Psi_i = \sum_{j \neq i} \Psi_j \frac{\langle \Psi_j | \Delta\hat{H} | \Psi_i \rangle}{E_i - E_j}. \quad (1.50)$$

In the perturbation theory, a "2n+1" theorem is used, which states that if the wavefunction is determined to all orders from 0 to n, the energy of the system to order 2n + 1 is determined. Applying the perturbation theory to density functional theory, we can write for the first order perturbation

$$\frac{\partial E}{\partial \lambda_i} = \frac{\partial E_{nn}}{\partial \lambda_i} + \int \frac{\partial V_{ext}(\mathbf{r})}{\partial \lambda_i} n(\mathbf{r}) d\mathbf{r} \quad (1.51)$$

and for the second order perturbation

$$\frac{\partial^2 E}{\partial \lambda_i \partial \lambda_j} = \frac{\partial^2 E_{nn}}{\partial \lambda_i \partial \lambda_j} + \int \frac{\partial^2 V_{ext}(\mathbf{r})}{\partial \lambda_i \partial \lambda_j} n(\mathbf{r}) d\mathbf{r} + \int \frac{n(\mathbf{r})}{\partial \lambda_i} \frac{\partial V_{ext}(\mathbf{r})}{\partial \lambda_j} d\mathbf{r}. \quad (1.52)$$



What we get is the response of the energy to the perturbation in the second order perturbation theory. The problematic term is the  $\partial n(\mathbf{r})/\partial\lambda_i$ , representing the change of the density with respect to the perturbation (to the first order). This is equivalent to knowing the first order change of the wavefunctions to obtain the second order correction to the energy. Using the chain rule, we can write the problematic third term in (1.52) as

$$\int \frac{\partial V_{ext}(\mathbf{r}')}{\partial\lambda_i} \frac{\partial n(\mathbf{r})}{\partial V_{ext}(\mathbf{r}')} \frac{\partial V_{ext}(\mathbf{r})}{\partial\lambda_j} d\mathbf{r}d\mathbf{r}' = \int \frac{\partial V_{ext}(\mathbf{r}')}{\partial\lambda_i} \chi(\mathbf{r}, \mathbf{r}') \frac{\partial V_{ext}(\mathbf{r})}{\partial\lambda_j} d\mathbf{r}d\mathbf{r}' , \quad (1.53)$$

where  $\chi(\mathbf{r}, \mathbf{r}')$  is the density response function.  $\chi(\mathbf{r}, \mathbf{r}')$  can be found using the relation

$$\chi = \chi^0[1 + K\chi] , \quad (1.54)$$

where  $\chi^0$  is the response function, defined as

$$\chi_n^0(\mathbf{r}, \mathbf{r}') = \frac{\delta n(\mathbf{r})}{\delta V_{eff}(\mathbf{r}')} = 2 \sum_{i=1}^{occ} \sum_j^{empty} \frac{\psi_i^*(\mathbf{r})\psi_j(\mathbf{r})\psi_j^*(\mathbf{r}')\psi_i(\mathbf{r}')}{\epsilon_i - \epsilon_j} , \quad (1.55)$$

and  $K$  is the kernel defined as

$$K(\mathbf{r}, \mathbf{r}') = \frac{1}{\mathbf{r} - \mathbf{r}'} - \frac{\delta^2 E_{xc}[n]}{\delta n(\mathbf{r})\delta n(\mathbf{r}')} , \quad (1.56)$$

which incorporates the Coulomb interaction and the exchange-correlation effects.  $\chi$  can also be found by using its relation with the inverse dielectric function

$$\epsilon^{-1} = 1 + \frac{\chi}{|\mathbf{r} - \mathbf{r}'|} . \quad (1.57)$$

Although the answer to the perturbation is given by finding the right form for the density response function  $\chi$ , the correct form is difficult to obtain except in the simplest of cases, such as homogeneous electron gas. The response function  $\chi^0$  and the inverse dielectric function  $\epsilon^{-1}$  are calculated using unoccupied states the system, of which there could be an infinite number. In principle, we would sum over enough unoccupied states until arbitrary convergence threshold is reached, which is often a problematic task.

## 1.4.2 DFPT

A simpler solution is given by applying the formalism of the perturbation theory to the Kohn-Sham equations directly. The first order change in density is given by

$$\Delta n(\mathbf{r}) = 2 \operatorname{Re} \sum_{i=1}^N \psi_i^*(\mathbf{r})\Delta\psi_i(\mathbf{r}) . \quad (1.58)$$

First order changes to the wavefunctions are given by

$$(H_{KS} - \epsilon_i)|\Delta\psi_i\rangle = -(\Delta V_{KS} - \Delta\epsilon_i|\psi_i\rangle), \quad (1.59)$$

where  $\Delta\epsilon_i = \langle\psi_i|\Delta V_{KS}|\psi_i\rangle$  and

$$\Delta V_{KS}(\mathbf{r}) = \Delta V_{ext}(\mathbf{r}) + \int d(\mathbf{r}')K(\mathbf{r}, \mathbf{r}')\Delta n(\mathbf{r}) \quad (1.60)$$

with  $K(\mathbf{r}, \mathbf{r}')$  defined in (1.56). This approach simplifies the problem of finding corrections to the wavefunctions, given in (1.59), by taking into account that only the unoccupied states contribute to the first-order corrections while the contributions from occupied states cancel out in pairs. By projecting the right-hand side of (1.59) to the unoccupied states, we get

$$(H_{KS} - \epsilon_i)|\Delta\psi_i\rangle = -\hat{P}_{unocc}(\Delta V_{KS}|\psi_i\rangle), \quad (1.61)$$

where

$$\hat{P}_{unocc} = 1 - \hat{P}_{occ} = 1 - \sum_{i=1}^N |\psi_i\rangle\langle\psi_i|. \quad (1.62)$$

By solving the above equation for the corrections, with  $\Delta V_{KS}$  given in terms of  $\Delta n(\mathbf{r})$ , which are itself given by  $\Delta\psi_i$ , we get a self-consistent method of finding the perturbation on the system. Unlike the general approach of the response function, which gives the answer to all possible perturbations, application of DFPT depends on the type of perturbation.

### 1.4.3 Phonons

Expanding the energy of the system (1.15) in powers of displacements, the first order derivatives are nothing else than equilibrium condition of the nuclei, i.e. the set of equations (1.47) equal to zero, and the higher derivatives describe the zero-point, thermal or perturbed motion of the nuclei

$$C_{I,\alpha;J,\beta} = \frac{\partial^2 E(\mathbf{R})}{\partial \mathbf{R}_{I,\alpha} \partial \mathbf{R}_{J,\beta}}, \quad C_{I,\alpha;J,\beta;K,\gamma} = \frac{\partial^3 E(\mathbf{R})}{\partial \mathbf{R}_{I,\alpha} \partial \mathbf{R}_{J,\beta} \partial \mathbf{R}_{K,\gamma}}, \dots, \quad (1.63)$$

where  $C$ 's are the quantities called force constants, and  $\alpha, \beta, \dots$  are cartesian coordinates.

Using the harmonic approximation, vibrational modes of frequency  $\omega$  are given by

$$\mathbf{u}_I(t) = \mathbf{R}_I(t) - \mathbf{R}_I^0 = \mathbf{u}_I e^{i\omega t}. \quad (1.64)$$

Inserting the above equation into 1.15 we get an equation

$$-\omega^2 M_I u_{I\alpha} = - \sum_{J,\beta} C_{I,\alpha;J,\beta} u_{J\beta} , \quad (1.65)$$

whose solution is given by setting the determinant of the system to zero

$$\det \left| \frac{1}{\sqrt{M_I M_J}} C_{I,\alpha;J,\beta} - \omega^2 \right| = 0 . \quad (1.66)$$

In a crystal structure, where atomic displacement eigenvectors also obey the Bloch theorem, the above equation decouples for different  $\mathbf{k}$  with frequencies  $\omega_{i,\mathbf{k}}$ , where  $i = 1, \dots, 3N_n$ :

$$\det \left| \frac{1}{\sqrt{M_s M_{s'}}} C_{s,\alpha;s',\alpha'} - \omega_{i,\mathbf{k}}^2 \right| = 0 . \quad (1.67)$$

These atomic oscillations in a lattice are called phonons. The set of all  $\omega_{\mathbf{k}}$  for a given  $i$  is called a phonon mode, of which 3 behave as  $\omega \rightarrow 0$  as  $\mathbf{k} \rightarrow 0$  and are called acoustic modes, while the rest are called optic modes. As  $\omega_{i,\mathbf{k}}$  are frequencies of oscillation they have to be real. If somehow one acquires imaginary frequencies, this result is non-physical and could indicate instability in the lattice dynamics.

Applying the DFPT for finding the phonon dispersions of a crystal, one would calculate the energy of the system under the perturbation, in this case a phonon of wavevector  $\mathbf{k}$  and then expand the energy in the second order:

$$E = E^0 + \frac{1}{2} \sum_{I,\alpha} \sum_{J,\beta} C_{I,\alpha;J,\beta} u_{I,\alpha} u_{J,\beta} , \quad (1.68)$$

where  $C_{I,\alpha;J,\beta}$  are the force constants defined in (1.63) and  $u_{I,\alpha}, u_{J,\beta}$  are the displacements of the atoms. First order of the expansion is ignored, as it is zero in the energy minimum. Force on a particular atom is then

$$F_{I,\alpha} = - \sum_{J,\beta} C_{I,\alpha;J,\beta} u_{J,\beta} \quad (1.69)$$

and the Fourier transform of  $C_{I,\alpha;J,\beta}$ , the dynamical matrix  $D_{I,\alpha;J,\beta}$ , gives us the phonon dispersions by finding it's eigenvalues for a particular wavevector  $\mathbf{k}$  and phonon mode  $i$

$$\sum_{J,\beta} D_{I,\alpha;J,\beta} \epsilon_{i,\mathbf{k}} = \omega_{i,\mathbf{k}}^2 \epsilon_{i,\mathbf{k}} . \quad (1.70)$$

#### 1.4.4 Elastic properties

The stress tensor  $\sigma_{\alpha\beta}$  for a particular structure is given by

$$\sigma_{\alpha\beta} = - \frac{1}{\Omega} \frac{\partial E_{tot}}{\partial u_{\alpha\beta}} , \quad (1.71)$$

where  $u_{\alpha\beta}$  is the strain tensor defined as

$$u_{\alpha\beta} = \frac{1}{2} \left( \frac{\partial u_\alpha}{\partial r_\beta} + \frac{\partial u_\beta}{\partial r_\alpha} \right), \quad (1.72)$$

with  $u$ 's being the displacements. Elastic properties are described by stress strain relations, with elastic constant, to linear order, given as

$$C_{\alpha\beta;\gamma\delta} = \frac{1}{\Omega} \frac{\partial^2 E_{tot}}{\partial u_{\alpha\beta} \partial u_{\gamma\delta}} = - \frac{\partial \sigma_{\alpha\beta}}{\partial u_{\gamma\delta}}. \quad (1.73)$$

For a two-dimensional structure of square, rectangular or hexagonal symmetry, non-zero elastic constants are  $C_{11}, C_{22}, C_{12}, C_{66}$ [33], where 1, 2, 6 are shorter notations for double indices  $xx, yy$  and  $xy$ , respectively. Hexagonal structures also have an additional relation which gives  $C_{66}$  as

$$C_{66} = \frac{1}{2}(C_{11} - C_{12}). \quad (1.74)$$

The in-plane stiffness (2D Young's moduli) in [10] and [01] directions[33] are given by

$$Y_{[10]} = \frac{C_{11}C_{22} - C_{12}^2}{C_{22}}, \quad Y_{[01]} = \frac{C_{11}C_{22} - C_{12}^2}{C_{11}}, \quad (1.75)$$

with Poisson's ratios

$$\nu_{[10]} = \frac{C_{12}}{C_{22}}, \quad \nu_{[01]} = \frac{C_{12}}{C_{11}} \quad (1.76)$$

which for hexagonal structures simplify to

$$Y = C_{11}(1 - \nu^2), \quad \nu = \frac{C_{12}}{C_{11}} \quad (1.77)$$

as  $C_{11} = C_{22}$ .

Treatment of strain in DFPT is given, in great detail, by Hamman, Wu, Rabe and Vanderbilt in [34]. Strain is treated as a perturbation only trough the metric tensor, and as such the elastic properties can be acquired trough DFPT with the same treatment as other types of perturbation.

## 1.5 Dielectric function

The imaginary part of the complex dielectric function  $\epsilon_{\alpha,\beta}^2(\omega)$ , when treated within the adiabatic perturbation theory, can be viewed as a response function

$$\begin{aligned} \epsilon_{\alpha,\beta}^2(\omega) = 1 + \frac{4\pi e^2}{\omega m^2} \sum_{n,n'} \sum_{\mathbf{k}} \frac{\hat{M}_{\alpha,\beta}}{(E_{k,n'} - E_{k,n})^2} \cdots \\ \cdots \left\{ \frac{f(E_{k,n})}{E_{k,n'} - E_{k,n} + \hbar\omega + i\hbar\Gamma} + \frac{f(E_{k,n})}{E_{k,n'} - E_{k,n} - \hbar\omega - i\hbar\Gamma} \right\}, \end{aligned} \quad (1.78)$$

where  $\Gamma$  is the adiabatic parameter,  $E_{k,n}$  are the energy eigenvalues,  $f(E_{k,n})$  is the Fermi distribution indicating the occupation of bands and  $\hat{M}_{\alpha,\beta}$  are the matrix elements

$$\hat{M}_{\alpha,\beta} = \langle u_{k,n'} | \hat{p}_\alpha | u_{k,n} \rangle \langle u_{k,n} | \hat{p}_\beta | u_{k,n'} \rangle , \quad (1.79)$$

with  $n$  and  $n'$  being occupied and unoccupied bands respectively.  $u_{k,n'}$  are the periodic parts of the Bloch wavefunctions which are further expanded in a plane wave basis set. The real part of the dielectric function can be obtained through Kramers-Kronig relations:

$$\epsilon_{\alpha,\beta}^1(\omega) = 1 + \frac{2}{\pi} \int_0^\infty \frac{\omega' \epsilon_{\alpha,\beta}^2(\omega')}{\omega'^2 - \omega^2} d\omega' \quad (1.80)$$

Dielectric function defined as in (1.78) does not take into account the non-local contributions to the Hamiltonian, meaning that the kernel  $K$  used in derivation of a response function (1.56) has the exchange-correlation energy set to zero. This is called the "random phase approximation". Once the dielectric tensor is obtained, one can proceed to calculate the various optical spectra[35], like the absorption spectrum

$$\alpha(\omega) = \sqrt{2}\omega \sqrt{|\epsilon(\omega)| - \epsilon^1(\omega)} , \quad (1.81)$$

refractive index

$$n(\omega) = \sqrt{\frac{|\epsilon(\omega)| + \epsilon^1(\omega)}{2}} , \quad (1.82)$$

extinction coefficient

$$k(\omega) = \sqrt{\frac{|\epsilon(\omega)| - \epsilon^1(\omega)}{2}} , \quad (1.83)$$

reflection spectrum

$$R(\omega) = \frac{[n(\omega) - 1]^2 + k^2(\omega)}{[n(\omega) + 1]^2 + k^2(\omega)} \quad (1.84)$$

and energy loss spectrum

$$L(\omega) = \frac{\epsilon^2(\omega)}{(\epsilon^1(\omega))^2 + (\epsilon^2(\omega))^2} . \quad (1.85)$$

## 1.6 Computer codes

Throughout this thesis, we have used the theoretical framework of density functional theory implemented inside two software packages. A major feature of both is that they are Open-Source and free to use software.

### 1.6.1 Quantum ESPRESSO

Quantum ESPRESSO[36] is an integrated suite of Open-Source computer codes for electronic-structure calculations and materials modeling at the nanoscale, based on density functional theory, pseudopotentials and plane waves. It is an open collaboration, available to everyone, coordinated by the Quantum ESPRESSO Foundation. It includes a set of components, each designed for a different part of density functional theory. Some capabilities of Quantum ESPRESSO include the ground-state calculations, structural optimization and molecular dynamics, response properties by the DFPT and more. On their official web pages, a database of pseudopotentials that were used in published scientific work is readily available for download. Majority of work carried out in this thesis was done in Quantum ESPRESSO.

### 1.6.2 ABINIT

ABINIT[37] is a software package whose main code allows, using DFT, calculations of total energy, charge density and electronic structure system composed from electrons and nuclei. ABINIT uses pseudopotentials or projector augmented wave (PAW) atomic data and planewave basis. Using DFPT, ABINIT can calculate the response functions such as phonons, effective charges and similar. ABINIT is distributed under the GNU General Public License.

# Chapter 2

## Two-dimensional crystal structures

We have chosen the planar honeycomb, buckled honeycomb, planar triangular and puckered structures in analogy with other monoelemental two-dimensional materials, as we expect possible structures of proposed elements will be the other elements due to similar valence electron structure. Graphene[38], borophene[10], silicene[7], germanene[9] and phosphorene[39] are materials we base our possible structures of antimony, indium and aluminium on.

### 2.1 Description of crystal lattices

#### 2.1.1 Planar honeycomb

Planar honeycomb structure is chosen in analogue to graphene. Planar honeycomb crystal structure is of hexagonal symmetry ( $R\bar{3}m$ ), with Bravais lattice containing two atoms in a lattice basis. Throughout this thesis, we will use shorthand  $\alpha$  to refer to planar honeycomb structure. We can choose the unit cell vectors as

$$\begin{aligned}\mathbf{a}_1 &= a (1, 0, 0) \\ \mathbf{a}_2 &= a \left( -\frac{1}{2}, \frac{\sqrt{3}}{2}, 0 \right) \\ \mathbf{a}_3 &= c (0, 0, 1),\end{aligned}\tag{2.1}$$

where  $a$  is the lattice constant (Fig. 2.1) and  $c$  is the height of the unit cell. Height  $c$  is necessary for the definition of the simulation unit cell, despite the two-dimensional nature of the planar structure. In practice, it is chosen to be large enough to act as a vacuum

above the plane where atoms are placed, and eliminate the interaction between periodic images of the crystal. Each atom has three equidistant neighbours, with distance given by  $d = a/\sqrt{3}$ . The angle between bonds is  $120^\circ$ . The unit cell used in computations is shown in Fig. 2.1 as the shaded rhombus. The chosen reduced coordinates of the atoms in the cell are

$$\begin{aligned} \text{Atom 1} &: \left( \frac{1}{3}, \frac{2}{3}, 0 \right) \\ \text{Atom 2} &: \left( \frac{2}{3}, \frac{1}{3}, 0 \right) . \end{aligned} \quad (2.2)$$

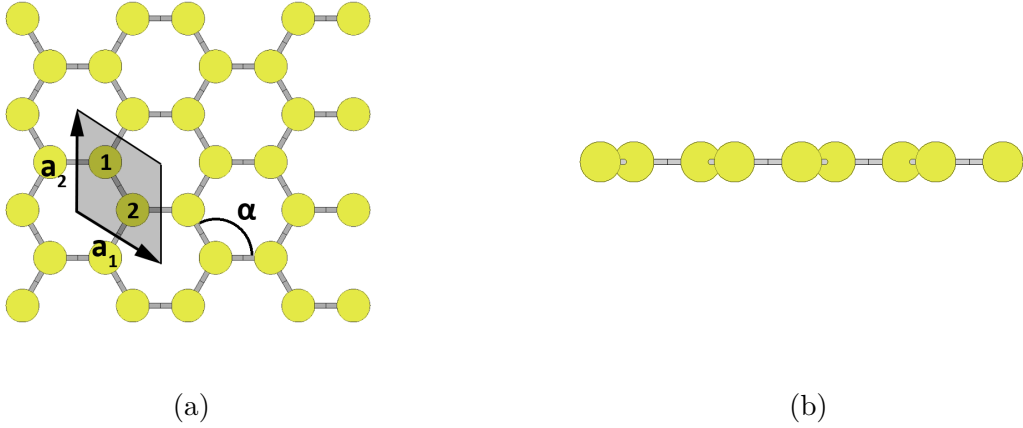


Figure 2.1: (a) top and (b) side view of  $\alpha$ -structure, with in-plane unit cell vectors  $\mathbf{a}_1$  and  $\mathbf{a}_2$ , and bond angle  $\alpha$ . Unit cell is shaded gray. Numbers denote atomic positions from 2.2.

The reciprocal lattice vectors are given by

$$\begin{aligned} \mathbf{b}_1 &= \frac{2\pi}{a} \left( 1, \frac{1}{\sqrt{3}}, 0 \right) \\ \mathbf{b}_2 &= \frac{2\pi}{a} \left( -\frac{1}{2}, \frac{2}{\sqrt{3}}, 0 \right) \\ \mathbf{b}_3 &= \frac{2\pi}{c} (0, 0, 1) . \end{aligned} \quad (2.3)$$

The first Brillouin zone with its in-plane high symmetry points is shown in the Fig.2.2.



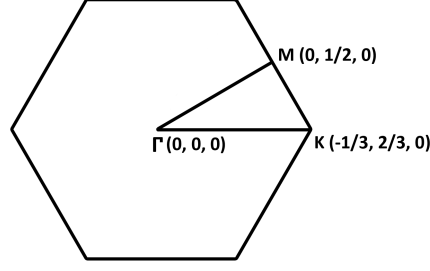


Figure 2.2: The first Brillouin zone of hexagonal unit cell and its high symmetry points.

### 2.1.2 Buckled honeycomb

Buckled honeycomb structure is chosen in analogue to silicene and germanene. Buckled honeycomb crystal structure is of hexagonal symmetry ( $R\bar{3}m$ ), with Bravais lattice containing two atoms in a basis. Throughout this thesis, we will use shorthand  $\beta$  to refer to buckled honeycomb structure. We can choose the unit cell vectors again as

$$\begin{aligned} \mathbf{a}_1 &= a (1, 0, 0) \\ \mathbf{a}_2 &= a \left( -\frac{1}{2}, \frac{\sqrt{3}}{2}, 0 \right) \\ \mathbf{a}_3 &= c (0, 0, 1), \end{aligned} \tag{2.4}$$

where  $a$  is the lattice constant (Fig. 2.3) and  $c$  is the height of the simulation unit cell. In the buckled structure, one atom in the basis is found at height  $h$  above the lattice plane, also called interlayer distance, thus creating two triangular sublattices. Each atom has three equidistant neighbours with the same angle between bond  $\alpha$ . The unit cell used in computations is shown in Fig. 2.3 as the shaded rhombus. The chosen reduced coordinates of the atoms in the cell are

$$\begin{aligned} \text{Atom 1} &: \left( \frac{1}{3}, \frac{2}{3}, 0 \right) \\ \text{Atom 2} &: \left( \frac{2}{3}, \frac{1}{3}, \frac{h}{c} \right). \end{aligned} \tag{2.5}$$

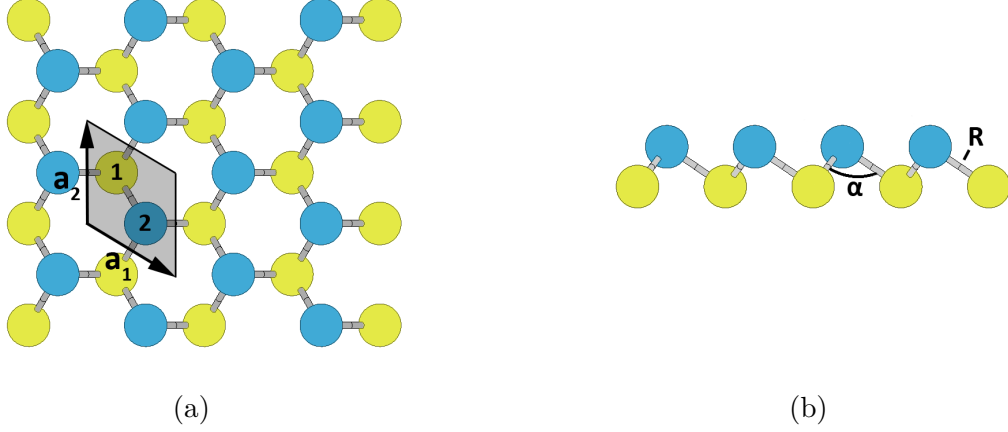


Figure 2.3: (a) top and (b) side view of  $\beta$ -structure, with in-plane unit cell vectors  $\mathbf{a}_1$  and  $\mathbf{a}_2$ . Two sublattices are designated with different colors. Bottom sublattice atoms are coloured yellow, while top sublattice atoms are coloured blue. Bond length is designated as  $R$  and the angle between bonds is designated as  $\alpha$ . Unit cell is shaded gray. Numbers denote atom positions from 2.5.

The reciprocal lattice vectors are given by

$$\begin{aligned}
 \mathbf{b}_1 &= \frac{2\pi}{a} \left( 1, \frac{1}{\sqrt{3}}, 0 \right) \\
 \mathbf{b}_2 &= \frac{2\pi}{a} \left( -\frac{1}{2}, \frac{2}{\sqrt{3}}, 0 \right) \\
 \mathbf{b}_3 &= \frac{2\pi}{c} (0, 0, 1) .
 \end{aligned} \tag{2.6}$$

The first Brillouin zone with its in-plane high symmetry points is shown in Fig. 2.2.

### 2.1.3 Planar triangular

Planar triangular structure is chosen in analogue to borophene. Planar triangular crystal structure is of hexagonal symmetry ( $R\bar{3}m$ ), with Bravais lattice containing one atom in a basis. Throughout this thesis, we will use shorthand  $\gamma$  to refer to planar triangular structure. We can choose the unit cell vectors in the same manner as for the honeycomb structure

$$\begin{aligned}
 \mathbf{a}_1 &= a (1, 0, 0) \\
 \mathbf{a}_2 &= a \left( -\frac{1}{2}, \frac{\sqrt{3}}{2}, 0 \right) \\
 \mathbf{a}_3 &= c (0, 0, 1) ,
 \end{aligned} \tag{2.7}$$

where  $a$  is the lattice constant (Fig. 2.4), and height  $c$  is used in the same manner as in the case of  $\alpha$ -structure. Each atom has six equidistant neighbours with the distance given by  $d = a$ . The angle between bonds is  $60^\circ$ . The unit cell used in computations is shown in Fig. 2.4 as the shaded rhombus. The chosen reduced coordinates of the atom in the cell is

$$\text{Atom 1 : } \left( \frac{1}{2}, \frac{1}{2}, 0 \right) \quad (2.8)$$

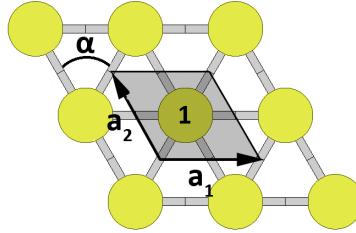


Figure 2.4: Top view of  $\gamma$ -structure, with in-plane unit cell vectors  $\mathbf{a}_1$  and  $\mathbf{a}_2$ , and bond angle  $\alpha$ . Unit cell is shaded gray. Numbers denote atom positions from 2.8.

The reciprocal lattice vectors are given by

$$\begin{aligned} \mathbf{b}_1 &= \frac{2\pi}{a} \left( 1, \frac{1}{\sqrt{3}}, 0 \right) \\ \mathbf{b}_2 &= \frac{2\pi}{a} \left( -\frac{1}{2}, \frac{2}{\sqrt{3}}, 0 \right) \\ \mathbf{b}_3 &= \frac{2\pi}{c} (0, 0, 1) . \end{aligned} \quad (2.9)$$

The first Brillouin zone with its in-plane high symmetry points is shown in the Fig. 2.2.

### 2.1.4 Puckered

Puckered structure is chosen in analogue to phosphorene. Puckered structure is of orthorhombic symmetry ( $Cmca$ ), with Bravais lattice containing four atoms in a basis. Throughout this thesis, we will use shorthand  $\delta$  to refer to puckered structure. Unit cell

vectors are given as

$$\begin{aligned}\mathbf{a}_1 &= a (1, 0, 0) \\ \mathbf{a}_2 &= b (0, 1, 0) \\ \mathbf{a}_3 &= c (0, 0, 1) ,\end{aligned}\tag{2.10}$$

with  $a$ ,  $b$  being the in-plane lattice parameters and  $c$  being the height of the simulation unit cell. Puckered structure also has two distinct sublattices, one being at the height  $h$  above the lattice plane. Each atom has 3 neighbours, with two distinct bond lengths  $R_1$  and  $R_2$ , as shown in Fig. 2.5. The structure has two unique bond angles,  $\alpha$  and  $\beta$ . The unit cell used in computations is shown in Fig. 2.5 as the shaded rectangle. The chosen reduced coordinates of the atoms in the unit cell are

$$\begin{aligned}\text{Atom 1} &: (0, 0, 0) \\ \text{Atom 2} &: (0.50, 0.35, 0) \\ \text{Atom 3} &: (0, 0.85, h/c) \\ \text{Atom 4} &: (0.50, 0.50, h/c) .\end{aligned}\tag{2.11}$$

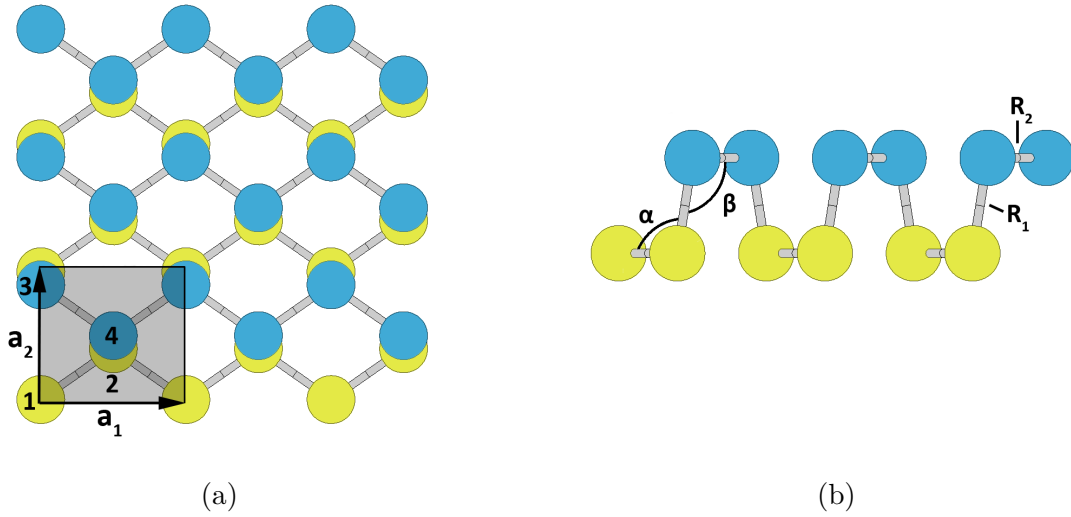


Figure 2.5: (a) top and (b) side view of  $\delta$ -structure, with in-plane unit cell vectors  $\mathbf{a}_1$  and  $\mathbf{a}_2$ . Two sublattices are designated with different colors. Yellow colour is the bottom, while blue is the top sublattice. Bonds are designated with  $R_1$  and  $R_2$ , while bond angles are designated as  $\alpha$  and  $\beta$ . Unit cell is shaded gray. Numbers denote atom positions from 2.11.

The reciprocal lattice vectors are given by

$$\begin{aligned}\mathbf{b}_1 &= \frac{2\pi}{a} (1, 0, 0) \\ \mathbf{b}_2 &= \frac{2\pi}{b} (0, 1, 0) \\ \mathbf{b}_3 &= \frac{2\pi}{c} (0, 0, 1) .\end{aligned}\tag{2.12}$$

The first Brillouin zone with its in-plane high symmetry points is shown in the Fig. 2.6.

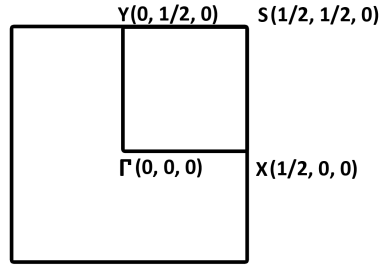


Figure 2.6: The first Brillouin zone of orthorhombic unit cell and its high symmetry points.

## 2.2 Results and discussion

### 2.2.1 Relaxed structures

Each of the three studied elements were initially put in the structures outlined above. By analogy, if they were to form two-dimensional crystals, it was expected they would form a structure similar to elements for which two-dimensional allotropes were already synthesized. From here on out, we will refer to two-dimensional allotropes of antimony, indium and aluminium using the usual convention for naming two-dimensional structures - by adding the suffix "-ene" - *antimonene*, *indiene* and *aluminene*. Optimized structural parameters of antimonene, indiene and aluminene are given in Table 2.1.

Table 2.1: Optimised parameters of aluminium, indium and antimony in the relaxed monolayer structures, where  $E_{coh}/\text{atom}$  is the cohesion energy per atom of the unit cell,  $a$  and  $b$  are lattice constants,  $h$  is the interlayer distance,  $\alpha$  and  $\beta$  are angles between bonds and  $R_1$  and  $R_2$  are bond lengths as denoted in Section 2.1.

Struct.	Elem.	$E_{coh}$ (eV/atom)	$a$ (Å)	$b$ (Å)	$h$ (Å)	$\alpha, \beta$ (degrees)	$R_1, R_2$ (Å)	Ref.
$\alpha$								
	Al	-2.32	4.46			120.00	2.57	
	In	-1.62	5.02			120.00	2.89	
	Sb	-3.01	4.99			120.00	2.88	
	C	-7.91	2.47			120.00	1.43	[40]
	In	-1.81	4.96			120.00	2.86	[41]
	Al	-1.96	4.49			120.00	2.59	[42]
$\beta$								
	Sb	-3.54	4.12		1.62	91.34	2.88	
	Si	-4.57	3.87		0.44	116.30	2.28	[40, 43]
	Ge	-3.20	4.06		0.64	112.30	2.44	[43]
	As	-2.99	3.61		1.39	92.22	2.50	[44]
	Sb	-4.03	4.12		1.65	90.8	2.89	[17]
	Sn	-2.68	4.47		0.73	113.50	2.70	[45]
$\gamma$								
	Al	-2.76	2.68			60.00	2.68	
	In	-1.83	3.16			60.00	3.16	
	B	-5.99	2.89		0.80	60.00	2.93	[46]
$\delta$								
	Sb	-3.54	4.33	4.92	2.74	95.16, 110.03	2.85, 2.91	
	Sb	-4.03	4.36	4.74	2.93	95.3, 102.4	2.87, 2.94	[17]
	As	-2.95	3.68	4.77	2.70	94.6, 100.8	2.50, 2.49	[47]
	P	-3.48	3.31	4.56	2.16	96.3, 103.1	2.24, 2.22	[48]

Cohesion energy is of prime importance for stability of a certain structure. We have defined cohesion energy as the difference between total energy of the crystal structure and

energy of a free constituting atoms

$$E_{coh} = E_{crystal} - NE_{free} , \quad (2.13)$$

where  $E_{crystal}$  is total electronic energy of the crystal cell,  $E_{free}$  is electronic energy of a single isolated atom and  $N$  is the number of atoms in the unit cell. All of the elements have negative cohesive energies which indicates that forming the predicted crystal structure is more favourable than atoms remaining in an isolated form (table 2.1).

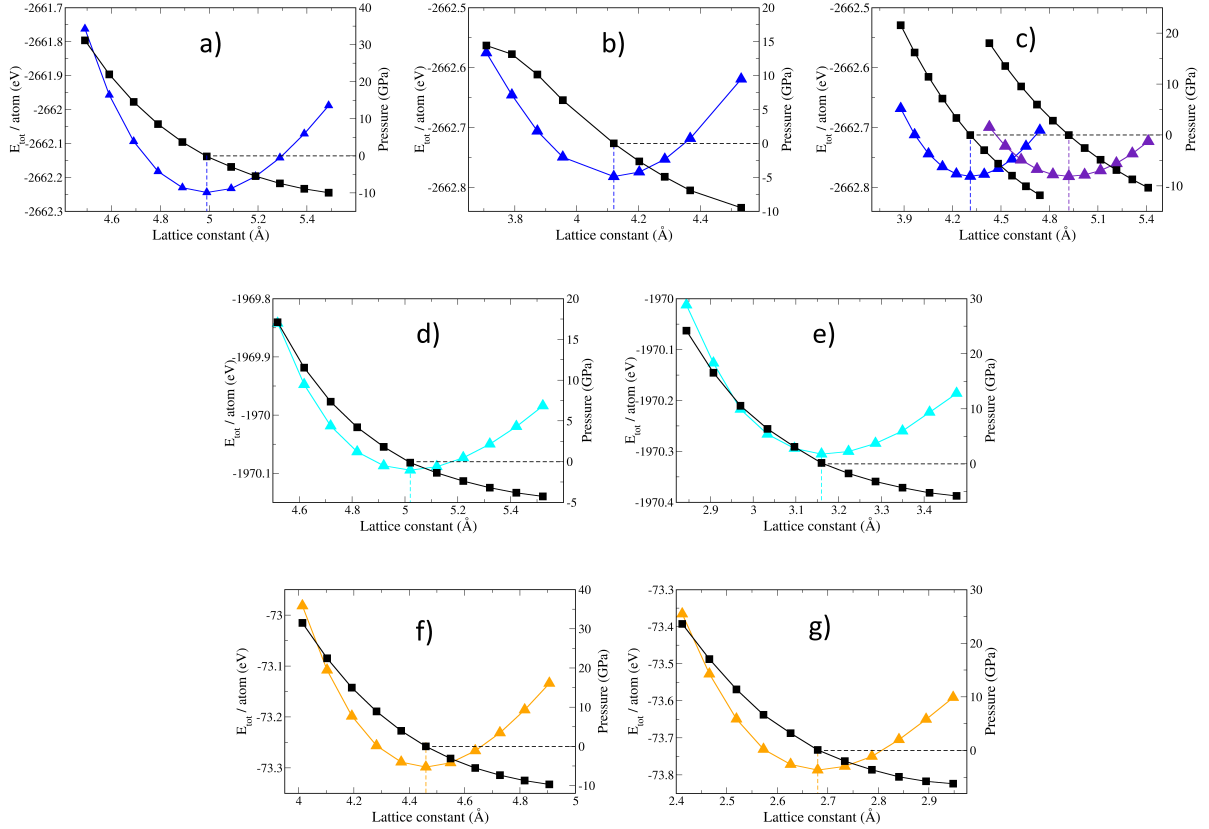


Figure 2.7: Dependence of total electronic energy  $E_{tot}$  per atom (coloured triangles) and pressure (black squares) on lattice constant for (a)  $\alpha$ , (b)  $\beta$ , (c)  $\delta$  antimonene allotropes, (d)  $\alpha$  and (e)  $\gamma$  indiene allotropes and (f)  $\alpha$  and (g)  $\gamma$  aluminene allotropes from table 2.1. Dashed lines give equilibrium lattice constants  $a_0$  (blue for Sb, cyan for In, orange for Al) and  $b_0$  (purple for Sb).

Equilibrium lattice constant(s) can be found from the total energy minimum and zero pressure conditions (no stress acting on the crystal unit cell), as the stress is related to

the total energy through:

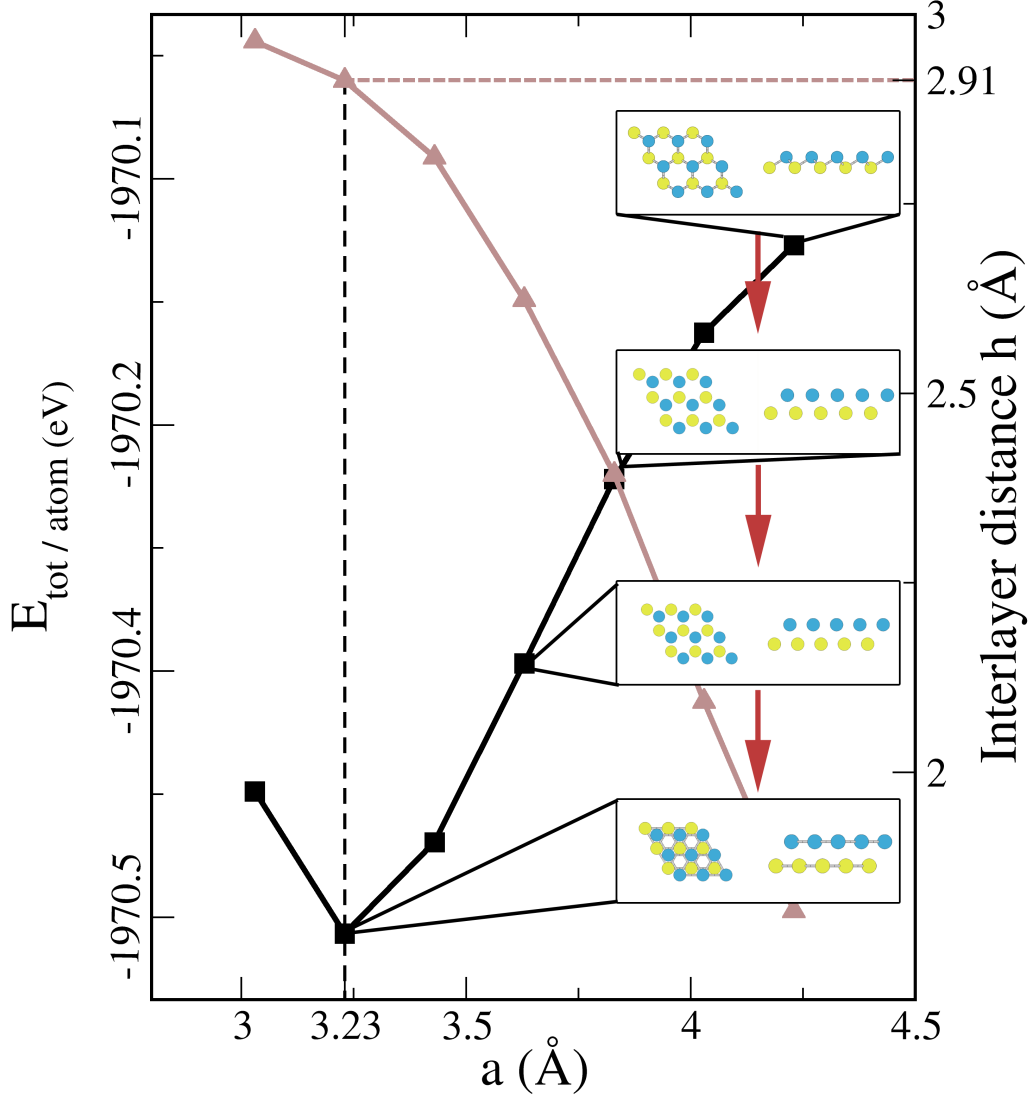
$$\sigma_{\alpha,\beta} = -\frac{1}{\Omega} \frac{\partial E_{tot}}{\partial \epsilon_{\alpha,\beta}}. \quad (2.14)$$

Figure 2.7 shows the dependence of total electronic energy per atom of a given structure on lattice constant, with the minima  $a_0$  and  $b_0$  corresponding to the lattice constants from table 2.1.

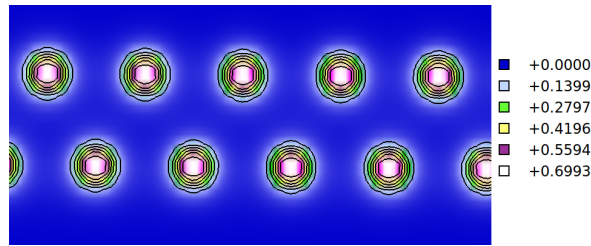
If indium and aluminium are placed initially into a buckled or puckered structure and then allowed to undergo unit cell optimization, the result is a structure that is formed by two layers of the planar triangular structure. Fig. 2.8 shows that the minimum of total electronic energy  $E_{tot}$  for the proposed  $\beta$ -In is found for lattice constant of  $a = 3.23 \text{ \AA}$  with an interlayer distance of  $h = 2.91 \text{ \AA}$ . This gives a smaller bond length between atoms in the same sublattice than between the atoms in different sublattices, which is not the case in the true  $\beta$  type structure, as found for example in silicene and germanene [7, 9]. Total energy landscape supports this stand-point. We manually changed the interlayer distance and observed the behaviour of the total energy. As the distance between the sublayers increases, the total energy decreases along with the lattice constant. This happens until the two sublayers separate enough to constitute two layers - a bilayer - instead of a single buckled monolayer. The hypothesis is that separated layers are energetically more stable than the buckled monolayer. To verify the true nature of the relaxed structure, we have calculated the charge density in-between the sublayers of the final, relaxed structure (Fig. 2.8). As can be seen, there is no charge density between the sublayers, indicating that this is the case of a triangular bilayer instead of a single buckled monolayer.

Structural relaxation for puckered type of structure has the same result, only with a different stacking of two triangular layers. Starting  $\beta$ -In and  $\beta$ -Al end with AB stackings of layers, while  $\delta$ -In and  $\delta$ -Al end with AA stackings of two triangular layers. Thus, we conclude that buckled or puckered structures of indium and aluminium relax through the unit cell optimization algorithm to the bilayers of planar triangular structure.





(a)



(b)

Figure 2.8: (a) Dependence of total electronic energy  $E_{tot}$  (black squares) and interlayer distance  $h$  (brown triangles) on lattice constant  $a$  for the proposed structure of  $\beta$ -In. Equilibrium  $E_{tot}$  and  $h$  are emphasized with broken lines. Insets show the relaxed structures for a given lattice constant. Red arrows indicate progression of the starting, two intermediate and the final  $\beta$ -In structure. (b) Charge density between sublayers of fully relaxed " $\beta$ -In", showing no charge in the interlayer space.

We compared the results of Table 2.1 with previous published studies, either with the same elements or with similar elements that form the same 2D structures. Different possible structures of antimonene were studied in reference [17], of which we can directly compare  $\beta$ -Sb and  $\delta$ -Sb. As seen in Table 2.1, parameters of  $\beta$ -structure are in excellent agreement. However, we are unable to reproduce the results for  $\delta$ -Sb at the GGA level of theory. Although one lattice constant agrees well (4.36 Å compared to our 4.33 Å), we notice larger discrepancy in the other lattice constant (4.74 Å compared to our 4.92 Å). We have used two different types of pseudopotentials, one ultrasoft and one norm-conserving, leading to the same lattice constant. Lattice constant of  $\alpha$ -In is in an agreement with reference [41], as well as the  $\alpha$ -Al with reference [42]. We are unable to compare  $\gamma$ -In, as there are no previous studies of it, up to our knowledge, as well as  $\gamma$ -Al since in reference [42] the Authors didn't consider this kind of allotropic modification.

As all three antimonene allotropes were synthesized experimentally, we can make the comparison of the lattice constants.  $\alpha$ -Sb synthesized on Ag(111) in [13] has a lattice constant of 5.01 Å which is in excellent agreement with our calculated lattice constant of 4.99 Å.  $\beta$ -Sb was synthesized on two different substrates, on PdTe<sub>2</sub>[14] and on germanene[15]. On PdTe<sub>2</sub> it has the lattice constant of 4.13 Å which is almost in perfect agreement with our results of 4.12 Å. On germanene, the lattice constant is 4.07 Å which differs the previous experimental value and our calculations by 1%, indicating that the choice of substrate influences the lattice constant of  $\beta$ -Sb. For  $\delta$ -Sb, obtained on WTe<sub>2</sub> [16], experimental lattice constants are 4.8 Å and 4.4 Å, which are in a good agreement with our calculated results of 4.92 Å and 4.33 Å.

### 2.2.2 Lattice dynamics

Obtaining the relaxed structures (in terms of forces) is the first step in investigating the stability of a certain crystal structure. Requiring the forces to go to zero at equilibrium ensures that the further application of higher order DFPT will not contain any residual forces, which might influence the subsequent calculations of phonon frequencies. Second step is to verify the lattice dynamical stability of the structures, and whether or not the crystal is stable with respect to small atomic displacements, i.e. all phonon frequencies have to be real[49]. For the structures given in table 2.1, we have, thus, calculated full phonon dispersions using DFPT. This allows us to check for lattice dynamical instabilities

throughout the Brillouin zone.

### Antimonene

Calculated phonon dispersions of different antimonene allotropes are shown in Fig. 2.9. We can see that the  $\beta$ -Sb has real phonon frequencies along the high symmetry directions of the Brillouin zone. Therefore, it satisfies the second condition of crystal stability.  $\alpha$ -Sb has two modes, out-of-plane acoustic and optic modes, with imaginary frequencies across the Brillouin zone, while  $\delta$ -Sb has one acoustic and one optic mode with imaginary frequencies around the  $\Gamma$ -point.

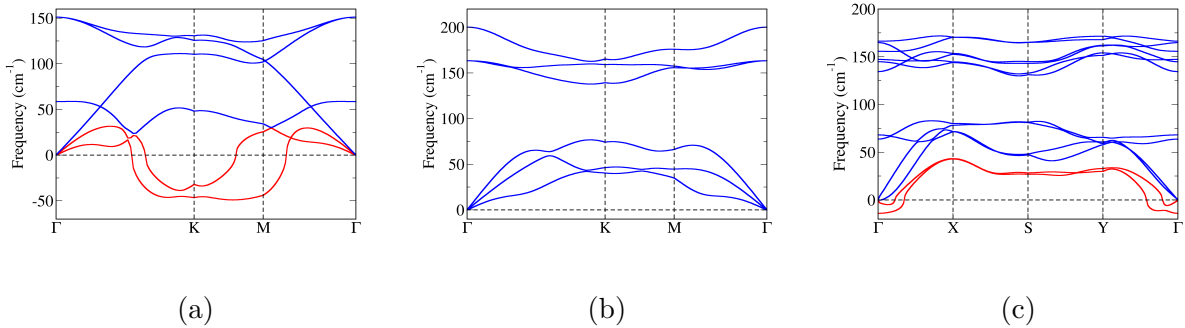


Figure 2.9: Phonon dispersions of (a)  $\alpha$ , (b)  $\beta$  and (c)  $\delta$  antimonene allotropes. Phonon modes with imaginary frequencies are shown in red colour.

As lattice dynamics of antimonene was a subject of earlier research, we have compared the obtained phonon dispersions with the ones from references [17] and [12]. The dispersions for  $\beta$ -Sb are in excellent agreement with already published theoretical results. Comparing the acoustic modes, in all cases they are real with the highest frequencies around  $70 \text{ cm}^{-1}$  at the  $K$ -point and with optical modes in good agreement at the  $\Gamma$ -point. Minor differences in the shapes of dispersion curves can be attributed to different pseudopotentials and methods of calculations used: we have used DFPT implemented inside Quantum ESPRESSO, while in reference [17] Phonopy code, based on the frozen phonon method, was used to obtain phonon dispersions.

$\delta$ -Sb is sometimes in literature referred as  $\alpha$ -Sb, although we reserve prefix  $\alpha$  for planar honeycomb structures. Although agreeing with phonon dispersions of ref. [17] in highest optic modes in both general shape and frequencies at high-symmetry points, the most striking difference is that we acquire imaginary frequencies for two of the phonon modes.

To verify our results, we have calculated phonon dispersions of  $\delta$ -Sb with a different type of pseudopotential (norm-conserving) and obtained similar results, with same phonon modes unstable as with the first pseudopotential (ultrasoft). These differences could be accounted by the discrepancies in optimized lattice constants, as one of the lattice constants of  $\delta$ -Sb is 3.8% larger than the one Authors have published in ref [17]. As lattice constants determine bond length and relative positions of atoms in regard to one another, thus are force constants that influence phonons affected - leading to different phonon frequencies.

For  $\alpha$ -Sb no comparison can be given, as there are no other studies on the lattice dynamics of this allotrope of antimony up to our knowledge. However, antimonene was experimentally synthesized with planar honeycomb structure on a Ag(111) substrate in a recent work [13], indicating that  $\alpha$ -Sb can have stable lattice dynamics. The discussion on the substrate dependent stability of antimonene allotropes is continued in the next chapter.

## Indiene

Calculated phonon dispersions of two indiene allotropes are shown in Fig. 2.10.  $\alpha$ -In has real frequencies along all high-symmetry directions of the Brillouin zone. It, thus, satisfies the second condition for crystal stability.  $\gamma$ -In has the lowest phonon mode's, the out-of-plane transverse acoustic (TA) mode, frequencies entirely imaginary.

We compared the obtained dispersions with the previous study [41]. For the  $\alpha$ -structure, we were not able to fully reproduce the results. Though both show real frequencies, they differ in shape of the modes, as well as numerically e.g. with the highest optical modes at the  $\Gamma$ -point being  $150 \text{ cm}^{-1}$ , compared to  $\sim 140 \text{ cm}^{-1}$  from reference [41]. We attribute the differences to different pseudopotentials used. While in our studies the In pseudopotential included the d-electrons, in Ref. [41] the pseudopotential contained only 3 electrons (two s-and one p-electron).

As the mentioned study did not include a type of  $\gamma$ -In structure, we are unable to give any comparison.

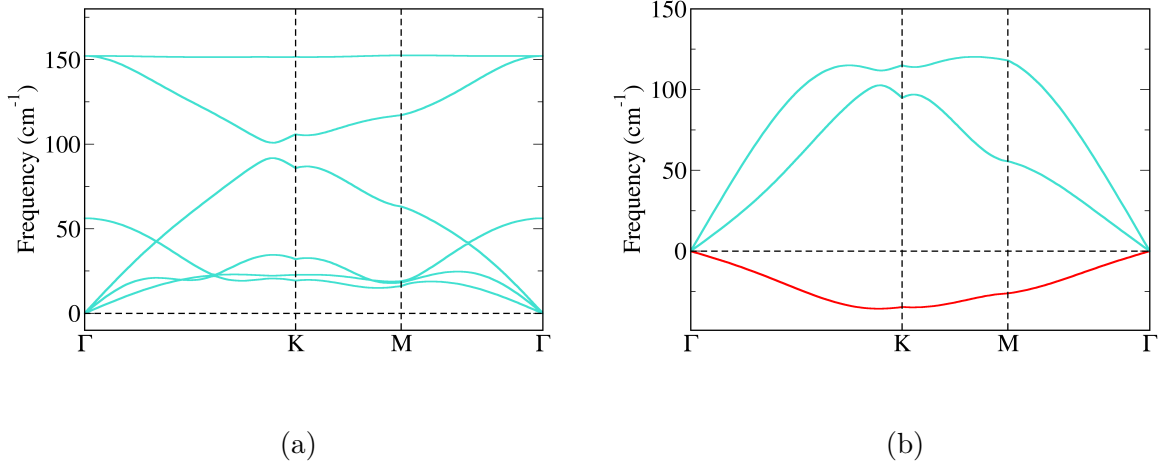


Figure 2.10: Phonon dispersions of (a)  $\alpha$  and (b)  $\gamma$  indiene allotropes. Phonon mode with imaginary frequencies are shown in red colour.

### Aluminene

Calculated phonon dispersions of two aluminene allotropes are shown in Fig. 2.11. Both structures have imaginary frequencies in the lowest acoustic mode(s), thus not satisfying the conditions of crystal stability. In the  $\alpha$ -Al the unstable phonon modes are the in-plane TA mode and out-of-plane TA mode, while with  $\gamma$ -Al the unstable mode is the out-of-plane TA mode.

Aluminene was studied previously by Kamal et al.[42]. We are unable to reproduce the results for the  $\alpha$ -structure. In the study by Kamal et al., all phonon frequencies are real. What we do note is that the frequencies of optical modes at the  $\Gamma$ -point do match at  $125 \text{ cm}^{-1}$  and  $\sim 350 \text{ cm}^{-1}$  and modes have an overall similar behaviour. We also could not fully reproduce the  $\gamma$ -structure phonon dispersions, with main differences being the maximum phonon frequencies at the  $M$ -point with  $\sim 350 \text{ cm}^{-1}$  and ours  $\sim 450 \text{ cm}^{-1}$ . We attribute the differences to pseudopotentials used.

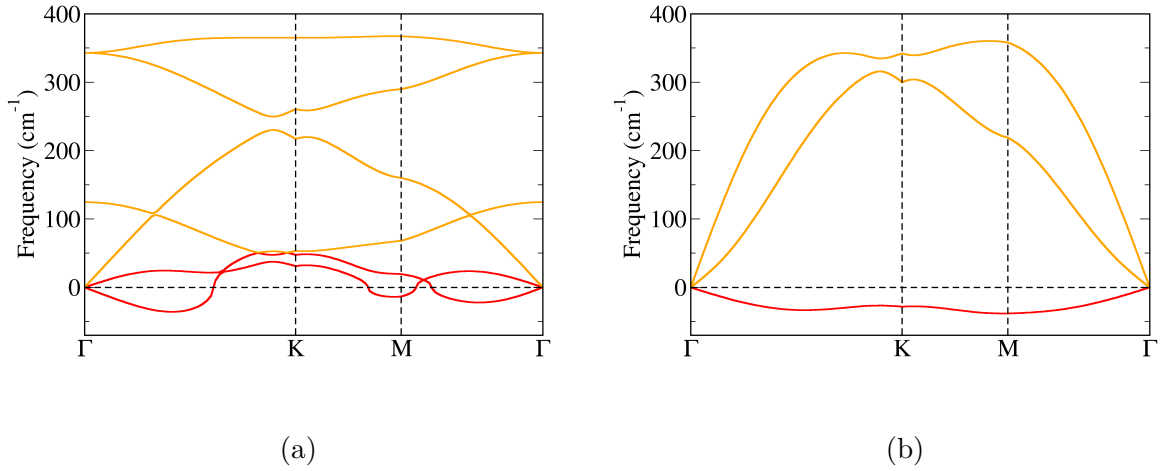


Figure 2.11: Phonon dispersions of (a)  $\alpha$  and (b)  $\gamma$  aluminene allotropes. Phonon modes with imaginary frequencies are shown in red colour.

At this stage of research on 2D allotropes of aluminium and indium (prior to experimental verification) it is very difficult to give any further comment based purely on theoretical simulations. Several factors, including both the lattice dynamics and substrate interaction, simultaneously influence the 'true' stability of their 2D allotropes. Therefore, it is ambiguous to regard any of the up to know published results as the correct ones, without carrying out further theoretical analyses. With that in mind, we continued to study their stability by taking into account the strain modifications caused by the suitable substrates.

# Chapter 3

## Strain engineering

Strain is used as a fairly straightforward way of modifying the properties of two-dimensional materials. It is readily achievable by experimental methods, such as using a cantilever-beam arrangement [50] or a four-point bending apparatus in which the substrate is usually held by titanium clamps [51]. Its effects on electronic and optical properties of a wide range of two-dimensional materials were studied in great detail [52–55]. Two-dimensional materials are extremely suitable for strain engineering since they can handle much higher mechanical stresses than their bulk counterparts [4]. Because of that stronger effects can be expected. Imposed strains can be separated in compressive (shrinking) and tensile (stretching) strain. On a unit cell level, strain is taken into account through appropriate modifications of the lattice constants.

Phonon modes which are unstable i.e. have imaginary frequencies in phonon dispersions (Figures 2.9-2.11), are exclusively acoustic modes, except in the case of  $\delta$ -Sb, where it is one acoustic and one optic mode. Acoustic phonon modes are products of in-phase movements of atoms in the crystal lattice. As in-plane strain changes the crystal lattice by modifying the distances between atoms, the possible consequence is the change in force constants that determine phonons, given in (1.63). Thus, strain can influence phonon modes of a crystal and potentially stabilize them. Our motivation is to use strain engineering to try to modify the lattice dynamical stability of the studied two-dimensional allotropes of indium and aluminium. Antimony already has stable lattice dynamics, proven experimentally and theoretically in references [13, 14, 17]. However, its lattice dynamics will nevertheless be studied in order to reveal the behaviour of phonons under external strain.

### 3.1 Types of strain in two-dimensional structures

As we are dealing with plane geometries, we can separate any direction of strain into two components. Taking the example of the honeycomb structure, the unit cell is of hexagonal symmetry with two atoms in the basis. By convention, chosen axes for probing strain effects are along the bond between two atoms and perpendicular to it, called armchair and zigzag, respectively. The names come from the fact that if we were to cut the crystal along the mentioned directions, their shape would remind of an armrest of a chair for armchair and a zig-zag shape for zigzag (Fig. 3.1). A special case is strain equal in both directions, called biaxial strain.

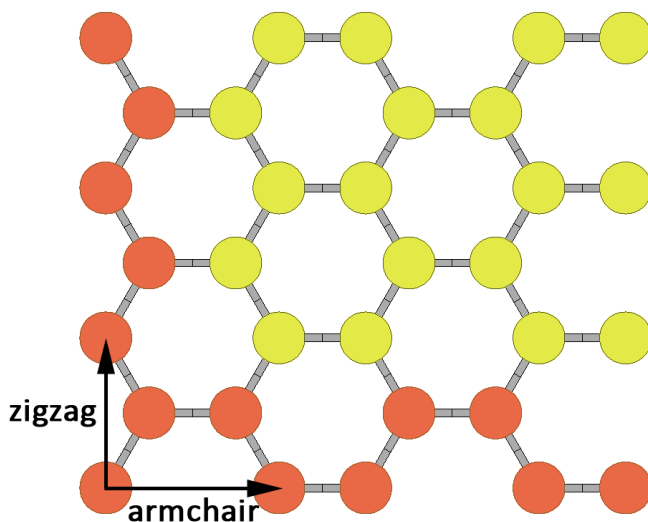


Figure 3.1: Armchair and zigzag strain directions. Left cut of the lattice is the zigzag termination of the crystal, while on the bottom (top) one is the armchair termination.

For puckered and triangular structures we keep the nomenclature even though they do not carry the same literal meaning. In the puckered case, strain is applied along the unit cell axes while in the triangular case it is along one bond and perpendicular to it (Fig. 3.2).



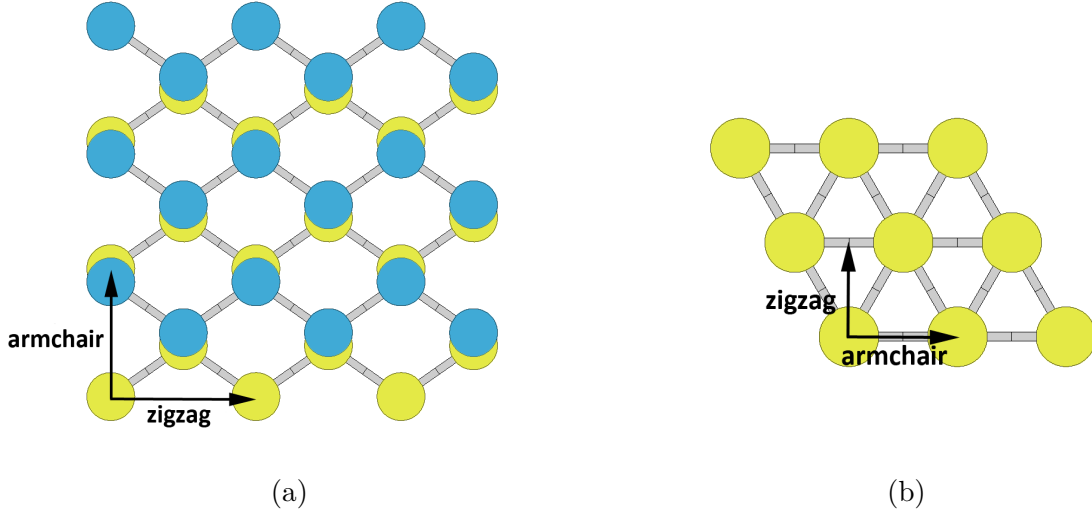


Figure 3.2: Strain directions for (a) puckered and (b) triangular structure.

Formally, strain is defined as

$$\varepsilon = \frac{a - a_0}{a_0}, \quad (3.1)$$

where  $a_0$  is the lattice constant of the non-strained structure and  $a$  is the lattice constant of the strained structure. Computationally, we modify the unit cells of hexagonal symmetry as indicated in Fig. 3.3.

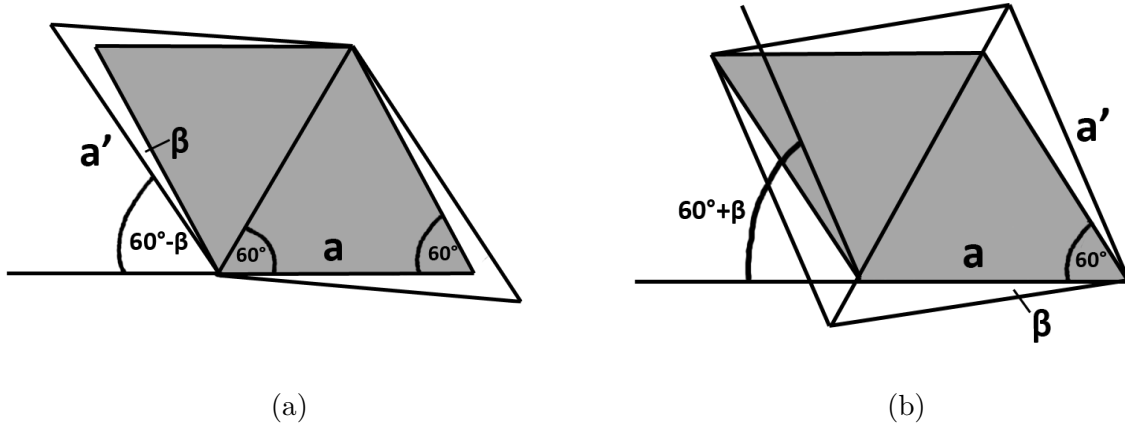


Figure 3.3: Strain-modified unit cell of honeycomb and triangular structures in (a) armchair and (b) zigzag directions.  $a$  is the unstrained lattice constant while  $a'$  is the new, strained, lattice constant. Unstrained unit cell is shaded in gray.

The lattice constant and unit cell vectors are then modified in armchair case as

$$\begin{aligned} a' &= \frac{1}{2}a\sqrt{1+3p^2} \\ \mathbf{a}_1 &= a'(\cos\beta, -\sin\beta, 0) \\ \mathbf{a}_2 &= a'(-\cos(60^\circ - \beta), \sin(60^\circ - \beta), 0) \end{aligned} \quad (3.2)$$

and

$$\begin{aligned} a' &= \frac{pa}{2} \frac{1}{\sin(30^\circ + \beta)} \\ \mathbf{a}_1 &= a'(\cos\beta, \sin\beta, 0) \\ \mathbf{a}_2 &= a(-\cos(60^\circ + \beta), \sin(60^\circ + \beta), 0) \end{aligned} \quad (3.3)$$

in zigzag case, where  $p$  is the percentage of strain imposed. After the unit cells are modified as per above equations, we allow the relaxation of atomic positions.

## 3.2 Results and discussion

### 3.2.1 Stress-strain relations

We have obtained the stress-strain relations for antimonene, indiene and aluminene allotropes using the procedure similar to methods used in references [17, 48, 56]. A range of strains from 80% to 140% was imposed in steps of 2% (Fig. 3.4). From the stress-strain relations we can obtain the critical strains as the minima of the stress-strain functions. Critical strain indicates the elastic range of strain a certain structure can undertake. This information is very useful, as they give predictions on how much one could stretch the materials before inelastic or plastic effects occur. From the graphs, we have read out the critical strains of each strained structure (table 3.1). What can be observed is that most of the structures show elastic anisotropy with regard to different strain directions, found also in other monoelemental 2D materials, like phosphorene [48], with notable exception of  $\alpha$ -In and  $\alpha$ -Al, which show almost isotropic properties in both strain directions (See Section 5.3).

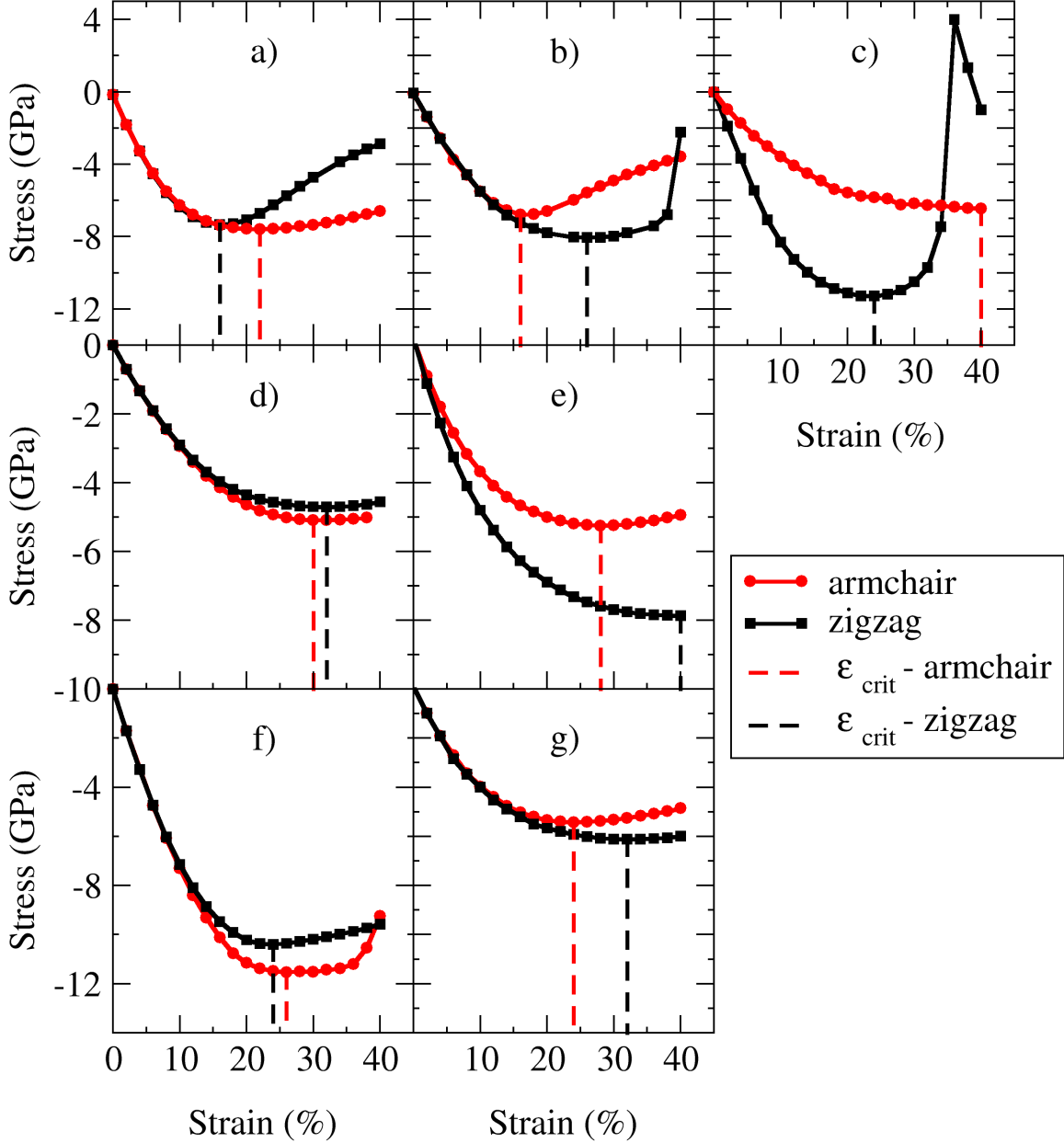


Figure 3.4: Stress-strain relations for (a)  $\alpha$ -Sb, (b)  $\beta$ -Sb and (c)  $\delta$ -Sb allotropes, (d)  $\alpha$ -In and (e)  $\gamma$ -In allotropes and (f)  $\alpha$ -Al and (g)  $\gamma$ -Al allotropes. Critical strains are denoted as  $\epsilon_{crit}$ . Missing points indicate failures in the convergence of the calculations.

For  $\beta$ -Sb and  $\delta$ -Sb we can directly compare the results with reference [17]. Critical strains for  $\beta$ -Sb from reference [17] are 18% and 15% for armchair and zigzag directions, respectively, while we acquire critical strains of 16% and 26%. We note large difference in the zigzag directions, which we attribute to difference in methods of calculations - different computer code, pseudopotential and simulated unit cell. We have used ultrasoft

Table 3.1: Critical strains in armchair and zigzag strain directions of antimonene, indiene and aluminene allotropes.

Struct.	Elem.	$\epsilon_{crit}$	$\epsilon_{crit}$	$\epsilon_{crit}$	Ref.
		- armchair (%)	- biaxial (%)	- zigzag (%)	
Planar - $\alpha$					
	Al	26	14	24	
	In	30	18	30	
	Sb	20	18	16	
	C	19	-	27	[57]
Buckled - $\beta$					
	Sb	16	18	26	
	Si	-	20	-	[58]
	Sb	18	-	15	[17]
Triangular - $\gamma$					
	Al	24	14	32	
	In	28	18	38	
Puckered - $\delta$					
	Sb	40	14	24	
	P	30	-	27	[48]
	Sb	32	-	18	[17]

pseudopotentials and a strained hexagonal unit cell with 2 atoms in the lattice basis, while in reference [17] the Authors have used PAW pseudopotentials and a rectangular unit cell with 4 atoms in the lattice basis. To better compare the results, we have also run our calculations for a rectangular unit cell to minimize the calculation differences and better compare the results, which confirmed our results of critical strain of 16% and 26% in armchair and zigzag directions, respectively. Critical strains for  $\delta$ -Sb from [17] are 32% and 18%, while we acquire critical strains of 40% and 24%. The discrepancy is substantial, though we also obtain a strong anisotropy with regard to armchair and zigzag critical strains, with similar difference between them (14% in reference [17] and 16% in our calculations).

### 3.2.2 Lattice dynamics under strain

To examine the influence of strain on lattice dynamics, we have calculated the phonon dispersions of structures from Table 2.1 in steps of 2% strain up to 20%. It has been verified that larger strains, although still under the critical values (Section 3.2.1), do not lead to different behaviour of lattice dynamics. All the compressive strains lead to instabilities in the lattice dynamics, i.e. to the imaginary frequencies of the phonon modes, so we will not be discussing them in detail in the main text. Some illustrative examples can be seen in the Appendix C.

#### Antimonene

Freestanding  $\alpha$ -Sb has two unstable acoustic modes (Fig 2.9). However, no amount of tensile strain stabilizes all of them. When subjected to strain, both out-of-plane phonon modes become unstable but one of the in-plane acoustic modes becomes unstable in all cases of strains. Thus, we conclude that the stability of  $\alpha$ -Sb will not be due to the influence of strain on its lattice dynamics (see Section 4.1.1). We show an example of influence of strain on  $\alpha$ -Sb phonon dispersions in Fig. 3.5.

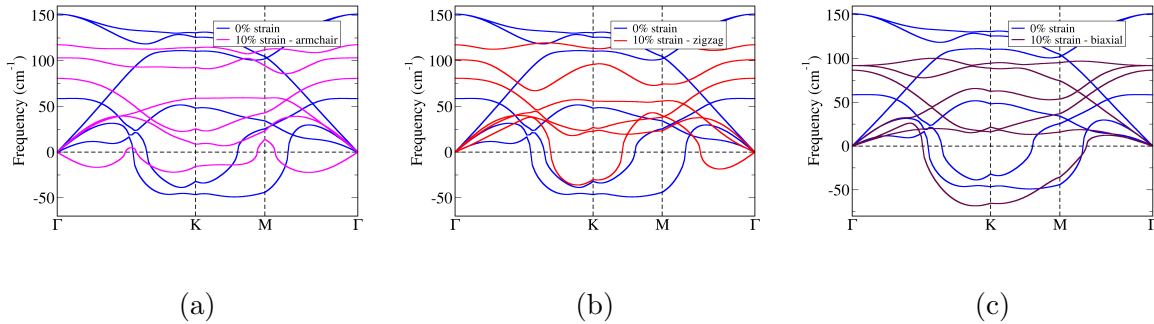


Figure 3.5: (a) Phonon dispersions of (a) armchair, (b) zigzag and (c) biaxially strained  $\alpha$ -Sb. A stabilization of one of the modes can be seen. Strain percentages are given in legends.

The case of freestanding  $\beta$ -Sb under strain is interesting, since unstrained  $\beta$ -Sb had stable lattice dynamics (Fig 2.9). However, when any kind of strain is applied,  $\beta$ -Sb lattice dynamics become unstable around the  $\Gamma$ -point. We notice this effect for all strains in all directions. In Fig. 3.6 we show an example of phonon dispersion of  $\beta$ -Sb under strain.

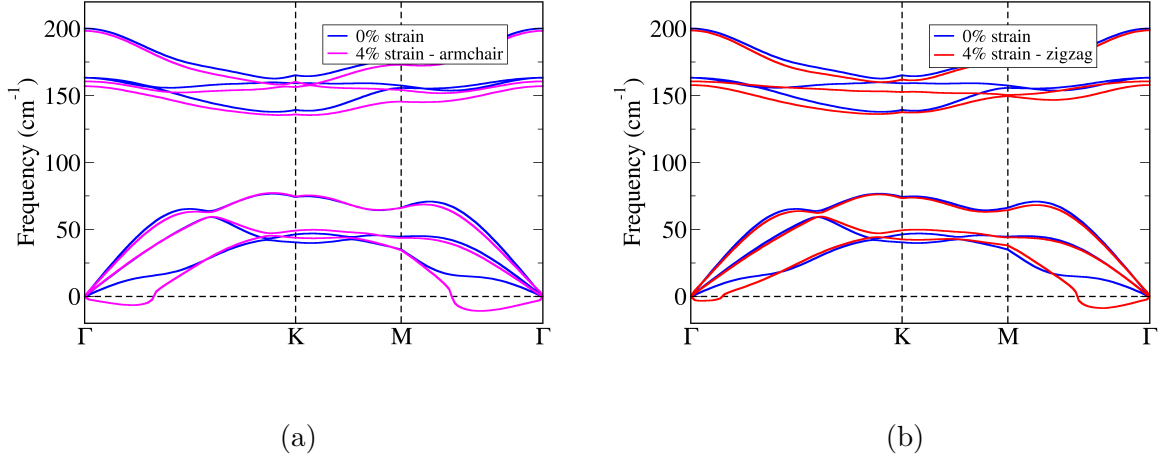


Figure 3.6: (a) Phonon dispersions of armchair strained  $\beta$ -Sb. (b) Phonon dispersions of zigzag strained  $\beta$ -Sb. Strain percentages are given in legends.

$\delta$ -Sb also has unstable lattice dynamics (Fig 2.9). As in the  $\alpha$ -Sb case, no amount of tensile strain stabilizes them. We can see the stabilization of the optic mode, but the out-of-plane TA mode remains unstable for all percentages of strain. In Fig. 3.7, we show examples of phonon dispersions of  $\delta$ -Sb under strain.

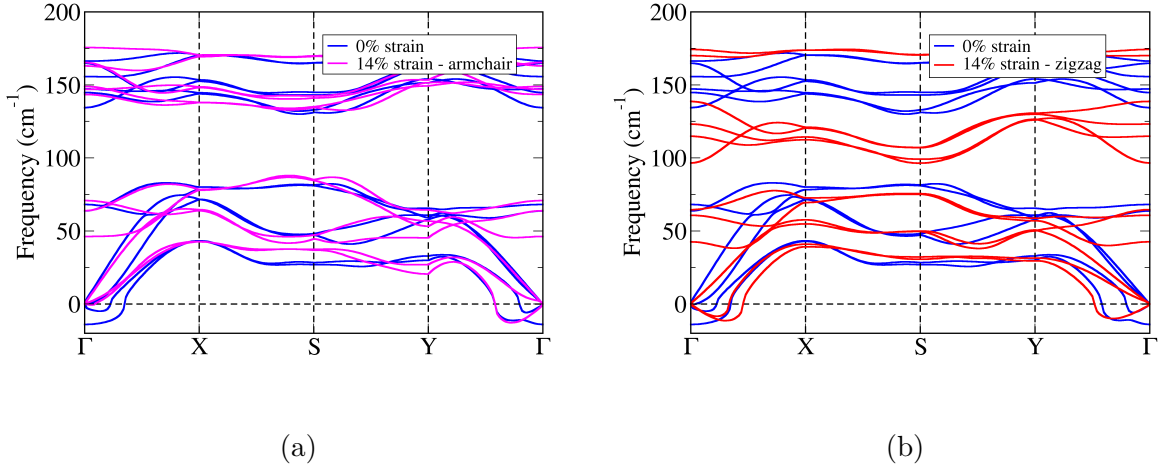


Figure 3.7: (a) Phonon dispersions of armchair strained  $\delta$ -Sb. (b) Phonon dispersions of zigzag strained  $\delta$ -Sb. Strain percentages are given in legends.

The lattice dynamics of freestanding antimonene are counterintuitive, as they all have been synthesized in experiment. Since the lattice dynamics do not become stable due to strain, possible source of their structural stability most probably could be the interaction

with the substrate they are synthesized on. The discussion on antimonene allotropes is continued in the next chapter, where we examine the influence of substrates.

## Indiene

Freestanding  $\alpha$ -In, as seen in Fig. 2.10, already has stable lattice dynamics. Under tensile strain, phonon frequencies remain real throughout the Brillouin zone for the entire range of strains in the armchair direction, while in the zigzag direction the frequencies remain real up to 14% strain. After 14% strain the lowest out-of-plane TA phonon mode becomes unstable. We show in Fig. 3.8, as an example, phonon dispersions of  $\alpha$ -In for armchair and zigzag strains of 10% and strain that shows imaginary frequencies in zigzag direction - 18%. Under biaxial strain,  $\alpha$ -In maintains stable lattice dynamics even up to 20% strain.

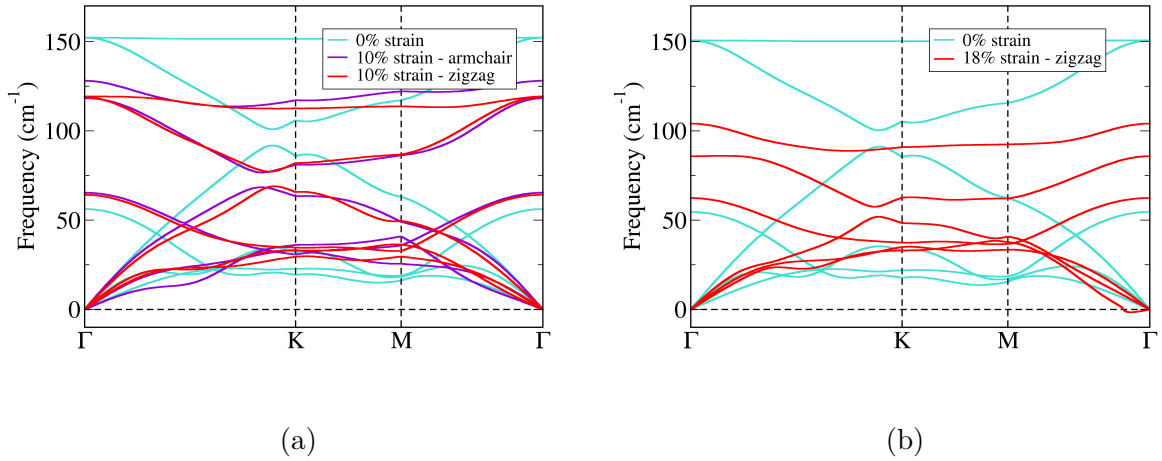


Figure 3.8: (a) Phonon dispersions of armchair and zigzag strained  $\alpha$ -In. (b) Phonon dispersions of  $\alpha$ -In strained in the zigzag direction by 18%, showing imaginary frequencies near the  $\Gamma$  point in the M- $\Gamma$  direction. Strain percentages are given in legends.

Freestanding  $\gamma$ -In has an unstable mode, as seen in Fig. 2.10. When strained in the armchair direction, the unstable phonon mode becomes stable for the range of strains of 12-14%, while in the zigzag direction the phonon mode is stable for the strain of 12%. When strained biaxially, the unstable phonon mode becomes stable for the strains of 6-8%. Lattice dynamics for different strain percentages of  $\gamma$ -In are shown in Fig. 3.9.

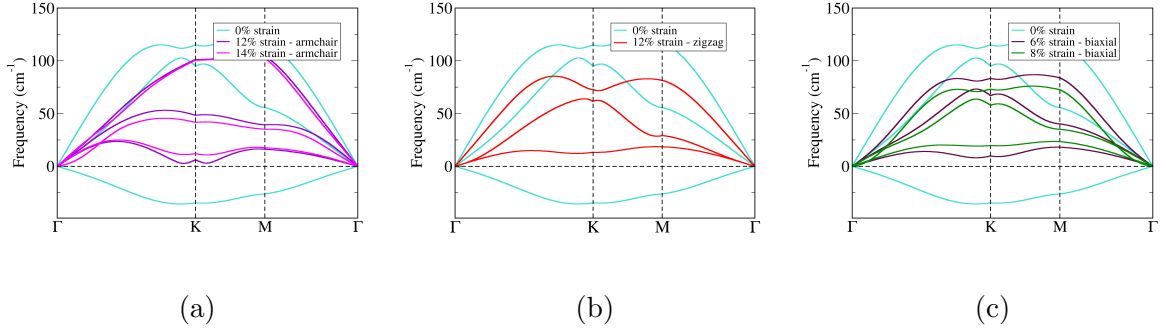


Figure 3.9: Phonon dispersions of (a) armchair, (b) zigzag and (c) biaxially strained  $\gamma$ -In. Strain percentages are given in legends.

## Aluminene

Both studied freestanding aluminene allotropes have an unstable phonon mode, as seen in Fig. 2.11. When strained in the armchair direction,  $\alpha$ -Al unstable phonon mode becomes stable only for strains of 14 and 18%. However, when strained in zigzag direction, the phonon mode is stable as soon as 4% strain is applied. This is reflected on lattice dynamics stability when strained biaxially - it has the same strain stability range as the zigzag direction - from 4% and on. In Fig. 3.10 we show the phonon dispersions with stable lattice dynamics for armchair directions, as well as the first percentage of strain that lead to stable lattice dynamics in zigzag and biaxial directions.

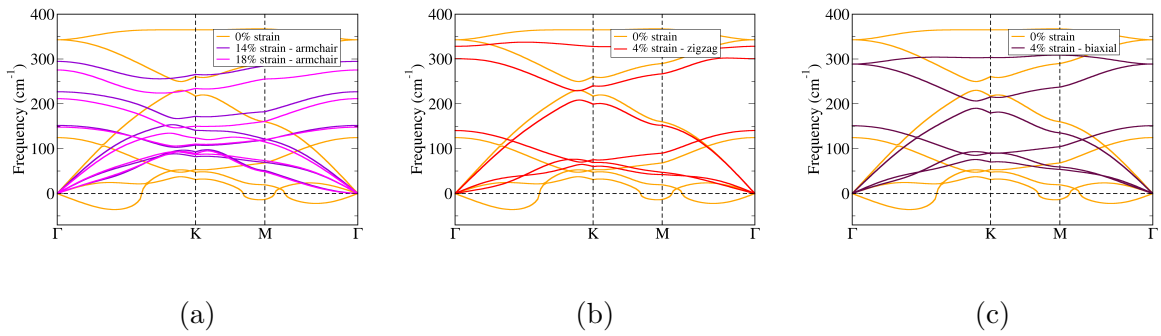


Figure 3.10: Phonon dispersions of (a) armchair, (b) zigzag and (c) biaxially strained  $\alpha$ -Al. Strain percentages are given in legends.

When  $\gamma$ -Al is strained in the armchair direction, we find a range of a stable phonon mode for strains of 4-16%, while in zigzag direction it is for strains of 2-14%. When strained biaxially, the phonon mode is stable for a small range of strains of 2-4%. In



Fig. 3.11 we show the phonon dispersions of first percentage of strain that lead to stable lattice dynamics for armchair and zigzag directions, as well as the percentages of strains with stable lattice dynamics in biaxial direction.

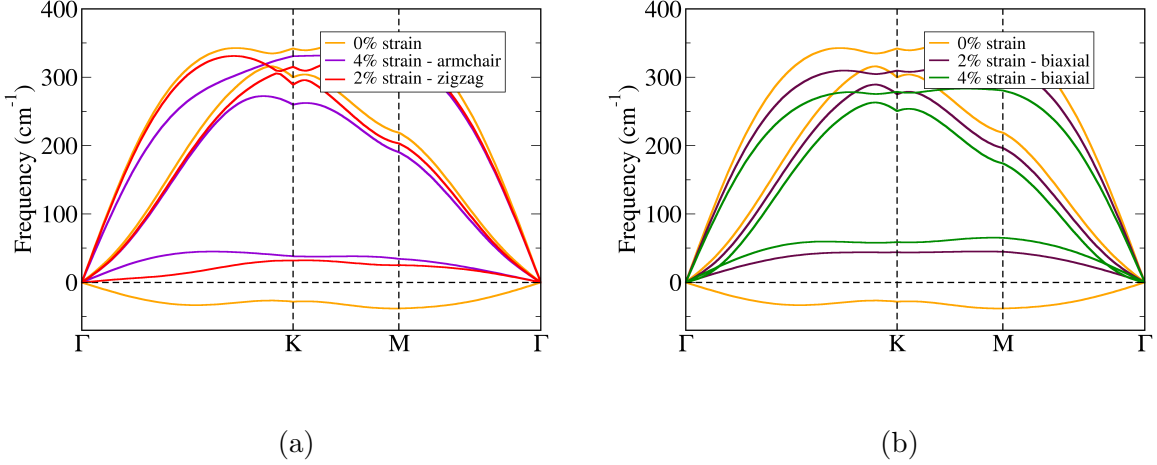


Figure 3.11: Phonon dispersions of (a) armchair and zigzag and (b) biaxially tensile strained  $\alpha$ -Al. Strain percentages are given in legends.

From the results of this section, it can be seen that it is quite possible to stabilize the lattice dynamics of 2D allotropes in several cases. This observation leads to the hypothesis that unstable free-standing 2D allotropes could be experimentally found under strained conditions. These conditions can be readily achieved using the suitable substrates which interact with the monolayers deposited on them. The next step is, thus, to simulate the behaviour of the studied 2D allotropes deposited on substrates.

As a final note, we condensed all the results presented in this chapter in a convenient way in Fig. 3.12, showing ranges of lattice dynamics stability of each studied structure.

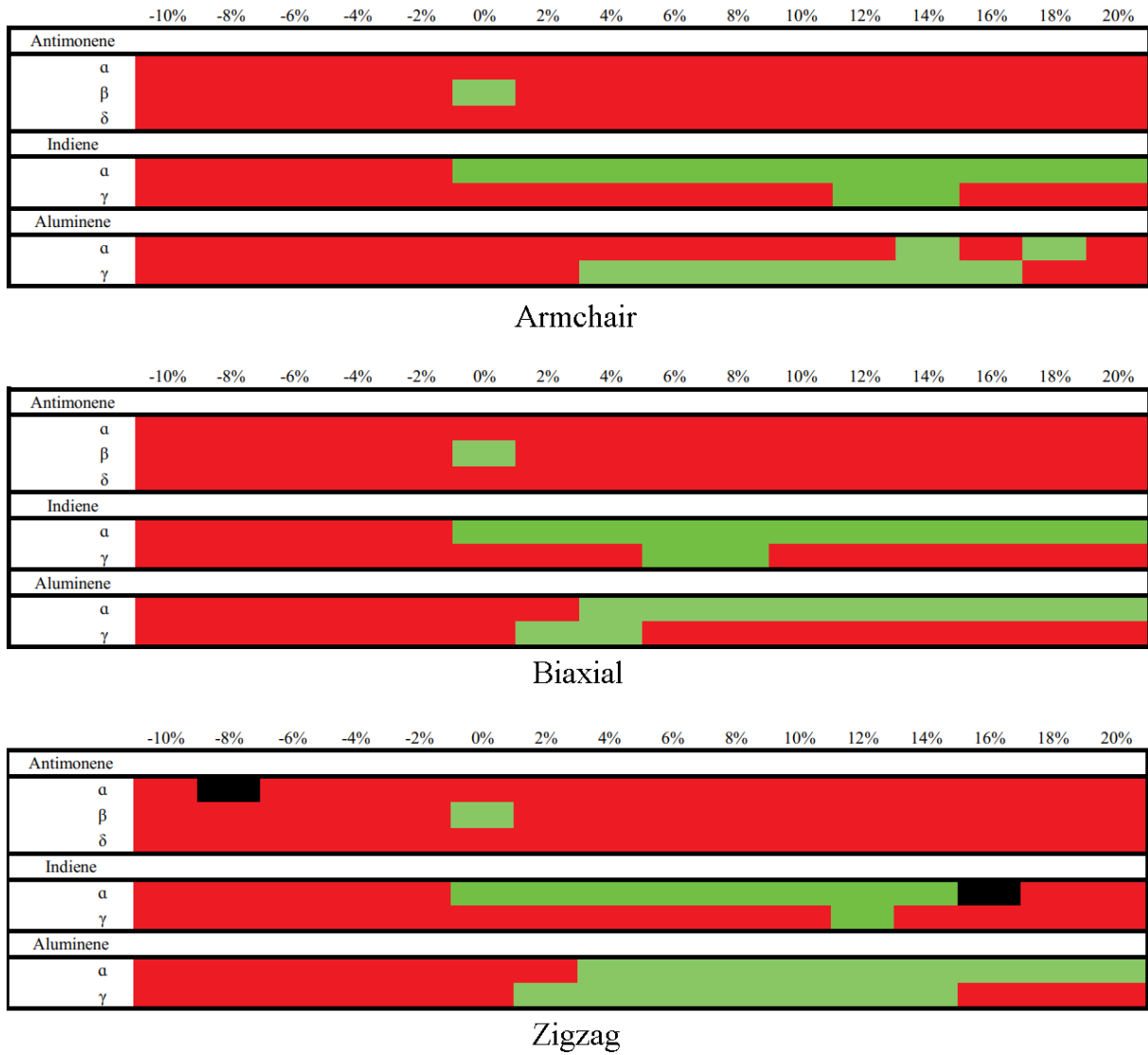


Figure 3.12: Lattice dynamics stability of two-dimensional allotropes in relation to strain imposed. Red areas denote unstable lattice dynamics, green areas stable lattice dynamics, while black areas are errors in the calculations.

# Chapter 4

## Substrates

It is not expected that any allotrope of indiene or aluminene could be obtained by the method of mechanical exfoliation, as it requires an already layered material, such as graphite or phosphorus. Antimonene on the other hand, whose bulk counterpart has a  $\beta$ -antimonene type structure with the unit cell formed from an ABC stacking of individual  $\beta$ -antimonene layers, which in theory enables the process of mechanical exfoliation, was experimentally obtained in all three allotropes proposed in this thesis [13–16]. However, only  $\beta$ -antimonene was obtained through exfoliation [10]. Thus, for experimental realization of indiene, aluminene and other allotropes of antimonene, a type of chemical synthesis is needed with the help of a suitable substrate. We also note that of several other monoelemental two-dimensional monolayers have been successfully synthesized on top of substrates, mostly metallic surfaces or other monolayers, which possess hexagonal symmetry [13, 15, 59].

Metallic surfaces are especially suitable, as they do not form chemical bonds with the synthesized monolayers, but they can induce strain through the substrate-monolayer interaction. The choice of the substrate has to satisfy two conditions: (i) sixfold hexagonal symmetry and (ii) the lattice mismatch of the substrate and the monolayer has to induce suitable strain upon the monolayer to induce the required changes in the lattice dynamics, as per previous chapter. We have chosen several promising substrates as candidates [60], however within the theoretical framework and chosen approximations we have been able to converge calculations only for Ag(111) and Cu(111), as well as graphene.

We have simulated the metallic surfaces by considering a slab unit cell with five layers of atoms, with the two-dimensional monolayer on top of it. As we do not expect large

changes in the surface of the metal, we have fixed the unit cell and only allowed the relaxation of atomic positions inside it. We have fixed bottom two substrate layers, as it was indicated (in previous theoretical research) that there is no significant interaction between the bottom substrate layers and the monolayer [59]. In this picture, the atoms of the monolayer move on the potential surface formed by the metallic surface and settle into the energetically most favoured positions: the ones that atoms would supposedly occupy in an experiment (Fig. 4.1). With graphene as the substrate, we do not expect a simple picture as with the metallic surface. Atoms of a deposited monolayer influence graphene's atoms and vice versa, so we have allowed full unit cell optimization of a such unit cell. We have included van der Waals interaction for both cases in our calculations [61].

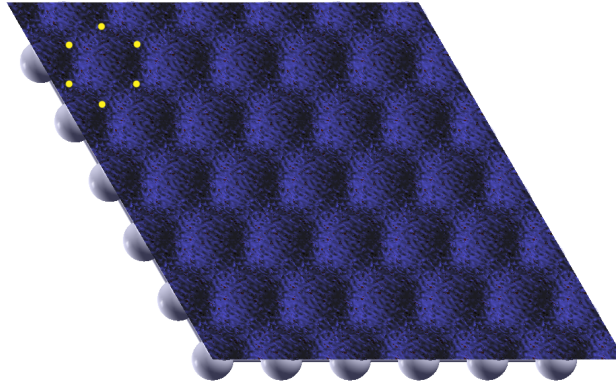


Figure 4.1: Surface potential of Ag(111). Ag atoms are coloured in gray. Hexagon tips coloured in yellow represent the minima of the potential energy.

Upon placing the monolayer atoms in the unit cell of the substrate, a natural lattice mismatch occurs. This lattice mismatch is the strain that is applied to the freestanding monolayer and it is purely biaxial in the beginning of the relaxation. Using this strategy we were able to circumvent using the supercells of the heterogeneous monolayer-substrate systems, which are very time consuming taking into account the available computational resources. However, the initial strain can morph into an armchair or zigzag strain, depending on how the atoms of the monolayer settle on the surface. The settling of the atoms will be a consequence of the monolayer-substrate interactions, i.e. interatomic forces which will effectively lead to the strained monolayer lattice. The settling of atoms on the substrate surface was simulated by the relaxation of the atomic positions via

---

BFGS algorithm described in section 1.2.1. Table 4.1 gives the initial lattice mismatches between the surfaces of Ag(111), Cu(111) and 2x2 graphene supercell we have used as the substrates, as well as the bond lengths  $R_1$ ,  $R_2$  and bond angles  $\alpha$ ,  $\beta$  after the relaxation.

At room temperature, the thermal effects could perturb the structural geometry of monolayers. This has to be taken into account in order to at least qualitatively assess the monolayer structures prior to their synthesis on the substrates and fabrication toward potential Sb, In or Al-based devices. We, thus, conducted *ab-initio* molecular dynamics simulations at 300 K of antimonene, indiene and aluminene on suitable substrates. We have taken time steps on different timescales and total time of simulation: 1 fs for the total time of 0.1 ps and time steps of 1 ps for the total time of 1 ns.

Table 4.1: Lattice mismatch, bond lengths  $R_1$ ,  $R_2$  and bond angles  $\alpha$ ,  $\beta$  after relaxation of monolayers on substrates.

Struct.	Elem.	Ag(111)			Cu(111)			2x2 graphene		
		Lattice mismatch (%)	$R_1$ , $R_2$ (Å)	$\alpha$ , $\beta$ (degrees)	Lattice mismatch (%)	$R_1$ , $R_2$ (Å)	$\alpha$ , $\beta$ (degrees)	Lattice mismatch (%)	$R_1$ , $R_2$ (Å)	$\alpha$ , $\beta$ (degrees)
Planar - $\alpha$										
	Al	40	5.05, 2.92	90.01	16	2.96, 2.95	119.89, 119.82	10	2.83	120.00
	In	16	3.42, 3.34	119.24, 121.52	2	2.99, 2.93	119.34, 121.32	-2	2.85	120.00
	Sb	17	3.70, 3.22	114.92, 130.16	2	2.96, 2.95	119.88, 120.24	-1	2.84	120.00
Buckled - $\beta$										
	Sb	42	3.70, 3.20	115.33, 130.21	24	2.95	120.00	19	3.09	104.34
Triangular - $\gamma$										
	Al	118	5.83	60.00	91	5.11	60.00	84	*	60.00
	In	84	5.83	60.00	62	5.11	60.00	56	4.93	60.00

## 4.1 Results and discussion

### 4.1.1 Structures on substrates

#### Antimonene

As we have seen from section 3.2, no amount of strain stabilizes the unstable phonon modes of the two unstable antimonene allotropes ( $\alpha$ -Sb and  $\delta$ -Sb) and even, in the case of  $\beta$ -Sb, unstabilizes the stable phonon modes of the unstrained structure. However, as proven by the experiments, all three allotropes should be stable when synthesized on a substrate. This was done for  $\alpha$ -Sb in ref. [13],  $\beta$ -Sb in ref. [14] and [15], and  $\delta$ -Sb in ref. [16]. It is clear that the stability of antimonene is ensured through its interaction with the substrate upon which it is deposited. Aim of this section is, thus, to verify what governs the antimonene synthesis on the substrates.

$\alpha$ -Sb was synthesized on the surface of Ag(111) [13]. Its lattice mismatch in our simulation is 17%, which is just inside the critical strain range for biaxial strain (table 3.1). After structural relaxation of the initial unit cell, we acquire two bond lengths of 3.70 Å and 3.22 Å, with bond angles of 114.92° and 130.16°. These results imply a case of zigzag strained  $\alpha$ -Sb, with atoms placed above the middle points of triangles formed by Ag atoms. Comparing these results with experiment, we notice disagreement with ref. [13], as the Authors obtain perfectly biaxial  $\alpha$ -Sb. However, as we have allowed the relaxation of top three layers of the substrate, this results in a surface potential that is not perfectly biaxial, as seen in the placement of monolayers. When  $\beta$ -Sb is placed on the same surface, we acquire almost the same final picture - atoms from the top  $\beta$ -Sb sublattice descend, forming an  $\alpha$ -Sb structure with almost exactly the same structural parameters. Ag atoms of the top layer undergo some movement, but preserve their hexagonal symmetry (Fig. 4.2), with some of the Ag atoms protruding above the surface giving various distances between substrate and the monolayer from 1.901 Å to 2.349 Å. This is repeated when  $\alpha$ -Sb and  $\beta$ -Sb are placed on Cu(111). Due to a smaller lattice mismatch (17% for Ag(111) and 2% for Cu(111)), the final structure of antimonene is nearly perfectly hexagonal on Cu(111), with negligible differences in bond lengths and bond angles of almost exactly 120°. The top layer of Cu(111) is slightly perturbed, giving various distances between the substrate and the monolayer from 2.169 Å to 2.249 Å.

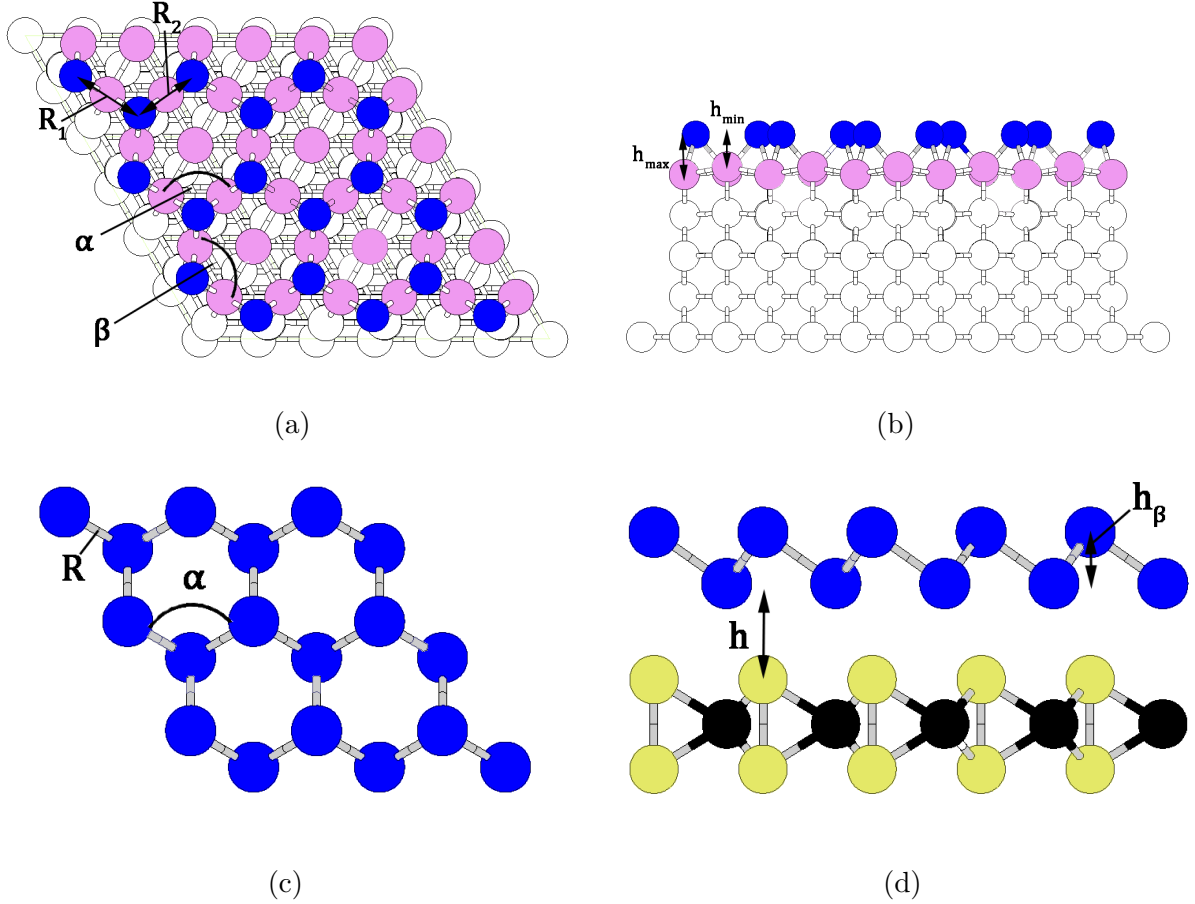


Figure 4.2: (a) top and (b) side view of relaxed  $\alpha$ -Sb and  $\beta$ -Sb structures on Ag(111). Sb atoms are coloured in blue, while the top layer of Ag atoms are coloured in pink. The remaining Ag atoms are coloured in white. (c) top and (d) side view of relaxed  $\alpha$ -Sb and  $\beta$ -Sb structures on PdTe<sub>2</sub>. Sb atoms are coloured in blue, Pd atoms are coloured in black, while Te atoms are coloured in yellow. Bond lengths are designated with  $R_1$  and  $R_2$  ( $R$  if they are the same), the bond angles are designated as  $\alpha$  and  $\beta$ . Minimum and maximum distances between the substrate and the monolayer are designated as  $h_{min}$  and  $h_{max}$  ( $h$  if they are the same), while  $h_\beta$  is the  $\beta$ -Sb interlayer distance.

The transformation of antimonene from  $\beta$ - to  $\alpha$ - structure upon synthesis on a flat substrate indicates that  $\alpha$ -Sb is the preferred antimonene allotrope if placed on such a substrate, as was the case in ref [13]. On the other hand, the synthesis of  $\beta$ -Sb obviously depends on a usage of non-flat substrate, such as the ones used in refs. [14] (PdTe<sub>2</sub>) and [15] (germanium). It would seem that the non-flat nature of the surface helps maintain the  $\beta$ -Sb buckled nature. Additional contribution comes from the fact that both substrates used in our work, Ag(111) and Cu(111), are much closer to lattice parameters of  $\alpha$ -Sb



(and within its elastic regime governed by critical strains) leading itself to  $\alpha$ -Sb as the preferred allotrope formed on such a surface.

Our view that the influence of the substrate, beyond only strain, is what stabilizes any allotrope of antimonene could be supported by deposition on PdTe<sub>2</sub>, as in ref. [14]. We have performed structural cell relaxation of  $\alpha$ -Sb and  $\beta$ -Sb on PdTe<sub>2</sub>. The structure of the monolayer at the end of relaxation is in both cases the structure of  $\beta$ -Sb, as seen in Fig. 4.2. The substrate and the monolayer have an exact AA stacking, with the bottom sublayer of  $\beta$ -Sb above Pd atoms and the top layer above the Te atoms. The bond lengths between Sb atoms are 2.85 Å with bond angles of 88.49°. The interlayer distance of two Sb sublayers,  $h$ , is 1.69 Å and the distance between the PdTe<sub>2</sub> and the  $\beta$ -Sb monolayer is 3.06 Å. Both distances are in agreement with theoretical results, from [14], of 1.65 Å and 2.49 Å. The lattice constant of  $\beta$ -Sb is 3.98 Å, differing from the experimental value by 4%.

From table 3.1, we can see that the lattice mismatch of 2x2 graphene and  $\beta$ -Sb falls just outside the range of critical strains, at 19%, but  $\beta$ -Sb preserves its buckled structure after the unit cell undergoes optimization. Graphene bond lengths shorten by a small amount, from 1.423 Å to 1.410 Å, while the buckling height of  $\beta$ -Sb decreases from 1.62 Å to 1.27 Å. With  $\alpha$ -Sb on graphene, changes in graphene bond lengths remain nearly the same, with no changes in  $\alpha$ -Sb. We do note different distances between graphene and the deposited layer of antimonene: in  $\alpha$ -Sb case it is 3.537 Å, while in  $\beta$ -Sb case it is 3.455 Å.

When  $\delta$ -Sb is placed on Ag(111) surface, it does not maintain its puckered structure. We acquire a bilayer of  $\alpha$ -Sb with near AA stacking. The bottom  $\alpha$ -Sb layer has the bond lengths of 3.07 Å and 4.08 Å with bond angles 143.01° and 108.47°. The top  $\alpha$ -Sb has bond length of 2.77 Å and 3.70 Å with bond angles 128.08° and 103.89°. Protrusions of Ag atoms are seen in this case, with distances ranging from 1.879 Å to 2.517 Å. These values are close to distances between the Ag atoms and the monolayer in the  $\alpha$ -Sb case. The distance between two  $\alpha$ -Sb layers is 2.767 Å. The breakdown of puckered structure is again seen when Cu(111) acts as a substrate. However, we obtain a bilayer composed of  $\alpha$ -Sb at the bottom and  $\beta$ -Sb on top. Type of stacking is AB, with lower atoms of the  $\beta$ -Sb above empty space of the  $\alpha$ -Sb hexagon below it. Both are nearly perfectly biaxial, with the bond lengths of  $\alpha$ -Sb 2.95 Å and bond angles of nearly 120.00°. The

bond lengths of top  $\beta$ -Sb are 3.03 Å with bond angles of 115.10°. Distance between the substrate Cu atoms and  $\alpha$ -Sb atoms is 2.265 Å with extremely small variations, which is in agreement with single  $\alpha$ -Sb monolayer on Cu(111), while the distance between the  $\alpha$ -Sb and  $\beta$ -Sb layers is 2.394 Å. The interlayer distance,  $h$ , of  $\beta$ -Sb is 0.678 Å. On graphene, the resulting structure is a bilayer of  $\beta$ -Sb, with AA stacking. The bond angles of  $\beta$ -Sb are 2.91 Å with bond angles of 116.87°. The distance from graphene to bottom  $\beta$ -Sb layer is 3.22 Å, while distance between two monolayers is 2.89 Å. Graphene bond lengths increase by a small amount, from 1.423 Å to 1.434 Å. The interlayer distance,  $h$ , of  $\beta$ -Sb is 0.469 Å.

## Indiene

Looking at the lattice mismatch of  $\alpha$ -In and two metallic substrates, 16% for Ag(111) and 2% for Cu(111), we expect that  $\alpha$ -In deposited on them could form stable monolayer structure, as  $\alpha$ -In lattice dynamics remain stable for strains of up to 14% in the zigzag direction (and more in armchair and biaxial directions). After relaxation of  $\alpha$ -In on Ag(111) and Cu(111) surfaces, we obtain an almost purely biaxially strained lattice, unlike  $\alpha$ -Sb on Ag(111) where we see strain that is more zigzag in nature. We also notice the atomic protrusions of surface atoms, though they are larger than in the case of  $\alpha$ -Sb, with the varying distance between substrate and the monolayer from 1.798 Å to 2.600 Å. Indium atoms also relax above the triangles formed by the Ag or Cu atoms on the (111) surface (Fig 4.3).

As the lattice mismatch of  $\gamma$ -In is too large (table 4.1) and the strain imposed to it is far outside the range of critical strains, we do not believe  $\gamma$ -In could possess stable lattice dynamics on these substrates.

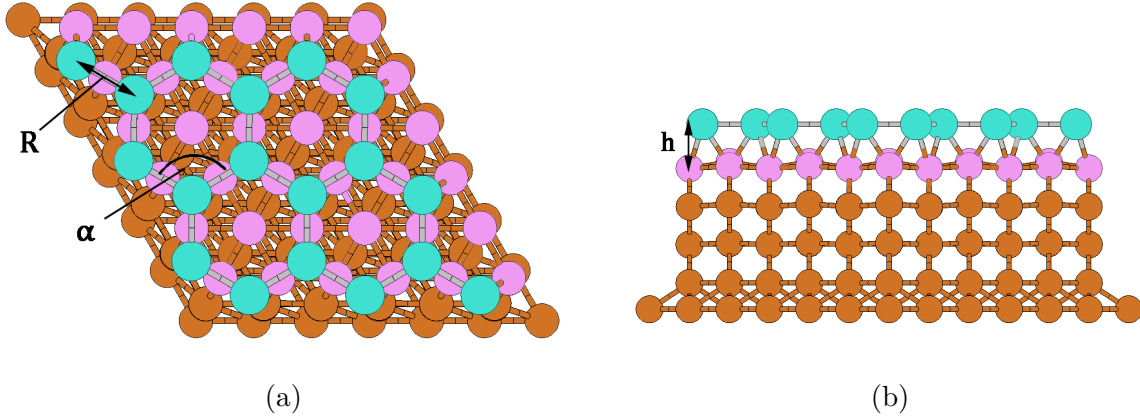


Figure 4.3: (a) top and (b) side view of relaxed  $\alpha$ -In on Cu(111). In atoms are coloured in turquoise, while the top layer of Cu atoms are coloured in pink. The remaining Cu atoms are coloured in brown. The Bond length is designated with R, the bond angle is designated with  $\alpha$  and the distance between the substrate and the monolayer is designated as h.

### Aluminene

With Ag(111) as a substrate,  $\alpha$ -Al is not expected to form a stable structure, as the lattice mismatch between the substrate and an unstrained  $\alpha$ -Al is far outside the range of critical strains (tables 3.1 and 4.1. However, Cu(111) and 2x2 graphene could possibly serve as the substrates, as the lattice mismatches are 16% and 10%, respectively. When  $\alpha$ -Al is placed on top of Cu(111) surface, it experiences almost purely biaxial strain, with bond lengths between atoms of an average 2.95 Å, and bond angles of 119.8° and 120.2°. The Cu atoms again show protrusions from the substrate top layer, with the substrate-monolayer distance varying from 1.719 Å to 2.046 Å. As with the  $\alpha$ -Sb and  $\alpha$ -In case, the monolayer remains in its planar geometry.

With  $\alpha$ -Al on graphene, it also experiences biaxial strain of 10%, leading to stable lattice dynamics. The stress is perfectly biaxial, with bond angles of 120.0°. The graphene bonds lengths shorten from 1.423 Å to 1.416 Å, which corresponds to small compressive strain in graphene. The distance between graphene and  $\alpha$ -Al is 3.7 Å. Relaxed structure of  $\alpha$ -Al on graphene is shown in Fig. 4.4.

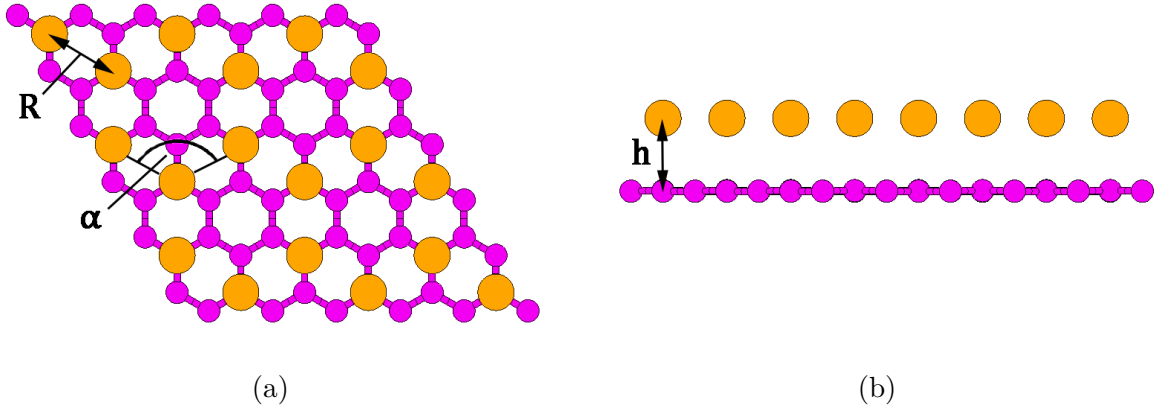


Figure 4.4: (a) top and (b) side view of relaxed  $\alpha$ -Al on graphene. Al atoms are coloured in orange, while the C atoms are coloured in pink. The Bond length is designated with  $R$ , the bond angle is designated with  $\alpha$  and the distance between the substrate and the monolayer is designated as  $h$ .

We also placed a ' $\beta'$ -Al (bilayer triangular) structure on top of a Cu(111) substrate. It relaxes to a structure identical to  $\alpha$ -Al on Cu(111), drawing similarities with the case of  $\alpha$ -Sb and  $\beta$ -Sb on Ag(111) and Cu(111), in which  $\beta$ -Sb relaxes to a structure almost identical to  $\alpha$ -Sb. It would seem that non-corrugated Ag(111)- and Cu(111)-like metallic surfaces favour structures of planar geometries, regardless of the type of element or initial structure placed on the substrate.

As the lattice mismatch of  $\gamma$ -Al is too large (table 4.1.1) and strain imposed to it is far outside the range of critical strains, we do not believe  $\gamma$ -Al could possess stable lattice dynamics on these substrates.

### 4.1.2 Molecular dynamics on substrates

Molecular dynamics simulations performed for Sb, In or Al allotropes on substrates show stability at finite temperature, regardless of timescale chosen. Monolayer and substrate atoms carry out thermal movements around the equilibrium positions, with changes in bond lengths, bond angles and interlayer separations. However, both the monolayer and substrate structures preserve their crystalline structures. As an example, in Fig. 4.5 we show  $\alpha$ -Al on Cu(111) at different time steps during the molecular dynamics simulation.

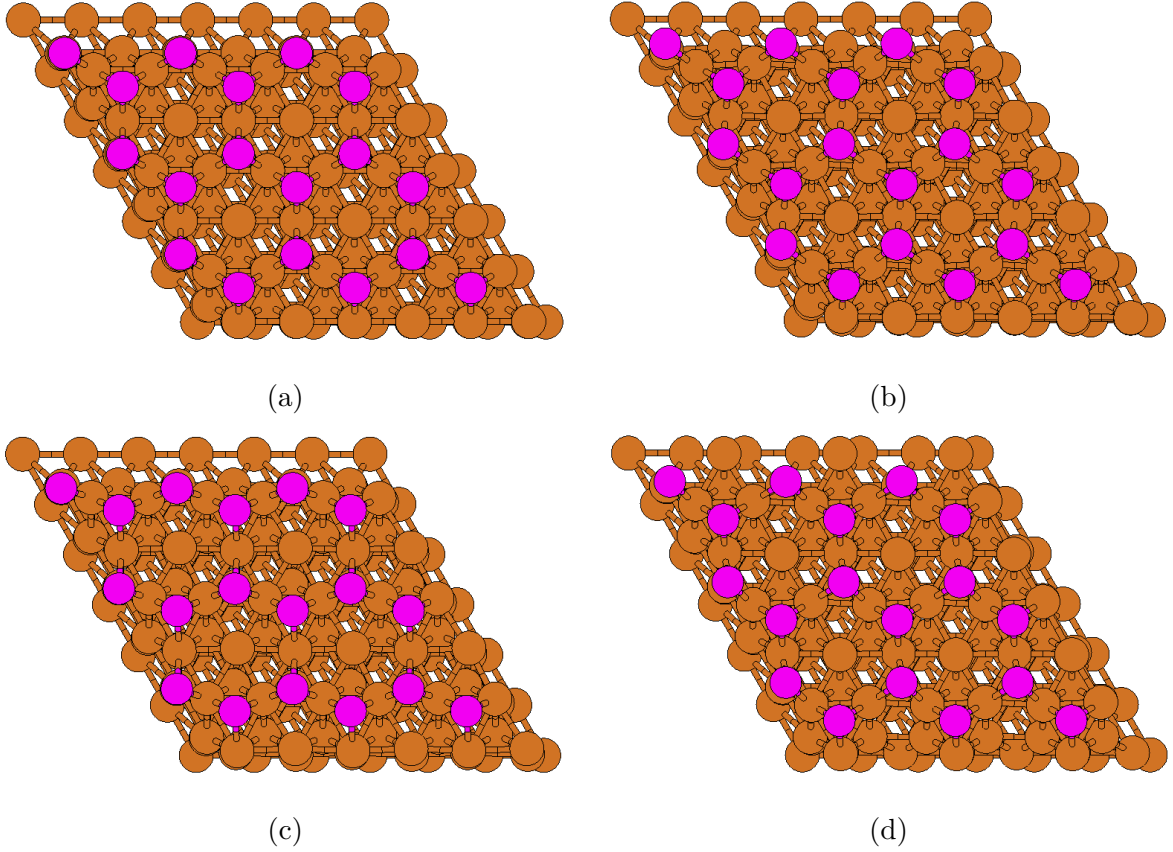


Figure 4.5: Molecular dynamics of  $\alpha$ -Al on Cu(111). Al atoms are coloured in pink, while Cu atoms are coloured in brown. (a)  $t = 1$  ps (b)  $t = 350$  ps (c)  $t = 700$  ps (d)  $t = 1000$  ps

To prove that the studied monolayers retain their crystallinity, we have plotted the radial distribution functions  $g(r)$  of  $\alpha$ -Sb,  $\alpha$ -In and  $\alpha$ -Al on the suitable substrates (Fig. 4.6). They show sharp peaks at particular interatomic distances. As there are no diffuse characteristics in the radial distributions, these results show that the studied monolayers on the substrates remain in their crystalline forms with respect to the thermal fluctuations.

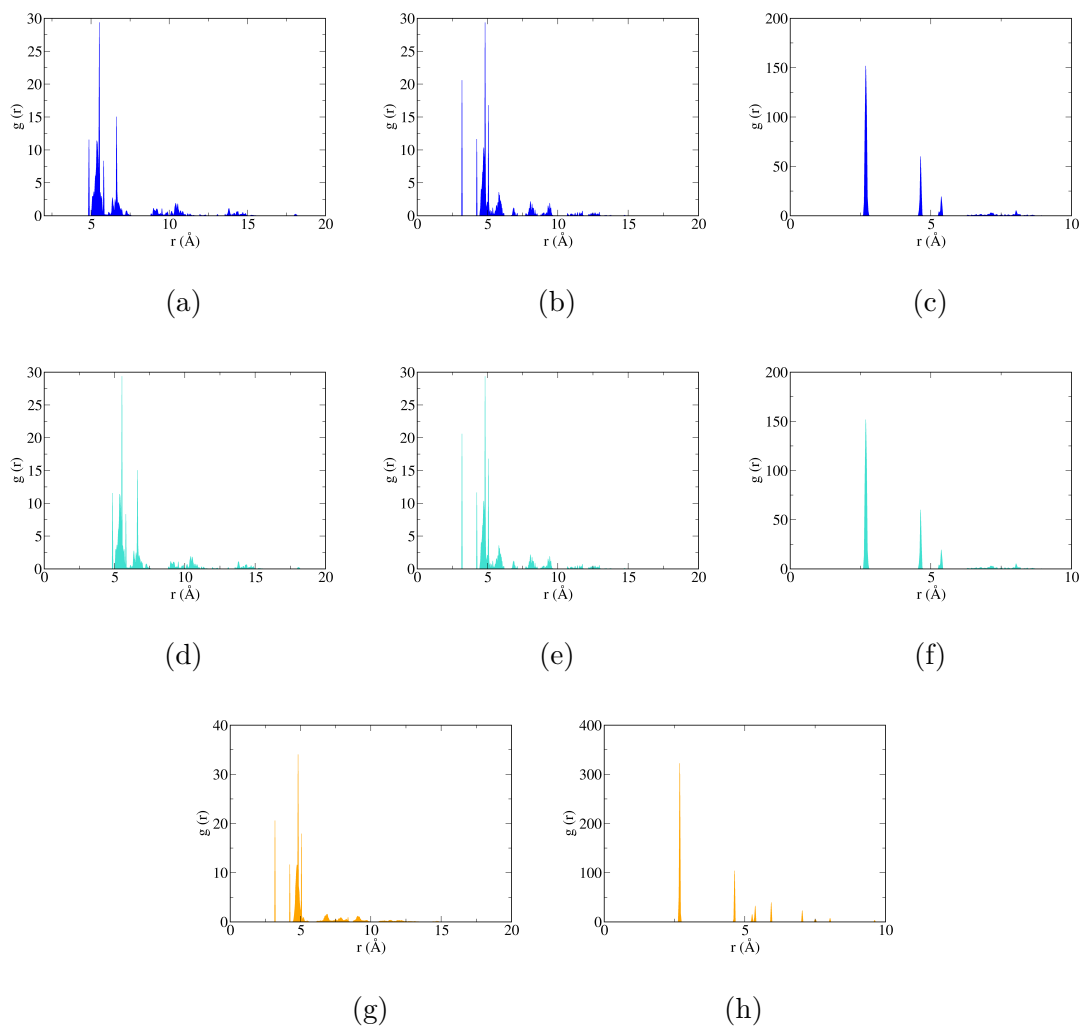


Figure 4.6: Radial distribution functions  $g(r)$  of  $\alpha$ -Sb on (a) Ag(111), (b) Cu(111) and (c) graphene;  $\alpha$ -In on (d) Ag(111), (e) Cu(111) and (f) graphene and  $\alpha$ -Al on (g) Cu(111) and (h) graphene.

# Chapter 5

## Characterization of predicted structures

As physical characteristics of 2D materials are important for their potential applications, we have performed *ab initio* calculations of their electronic, optical and elastic properties. In chapter 5 we show the results only for allotropes that we have determined are experimentally potentially viable, as per previous chapter. The results for the remaining allotropes are shown in Appendix D.

### 5.1 Electronic band structure

#### Antimonene

As known from previous published studies,  $\beta$ -Sb and  $\delta$ -Sb are semiconductors [17]. We have also in part reproduced these results, as shown in Fig. 5.1. Per our calculations,  $\alpha$ -Sb has metallic character. Band gap  $E_g$  of  $\beta$ -Sb is an indirect band gap with the value of 1.31 eV, while  $\delta$ -Sb has a small direct band gap of 0.06 eV.

Comparing the results with previous theoretical results from [17], we can see some discrepancy as the Authors report indirect bands gaps 0.76 eV and 0.28 eV for  $\beta$ -Sb and  $\delta$ -Sb, respectively. The differences for  $\beta$ -Sb could be attributed to different levels of approximation used for the exchange-correlation energy, as it is known that LDA underestimates the band gap, compared to GGA. We are unable to reproduce the band gap of  $\delta$ -Sb in both in the nature and the band gap value, however, we do note the difference in pseudopotentials used as well as difference in obtained lattice parameters of  $\delta$ -Sb.

Authors from ref. [17] have also included spin-orbit coupling in their calculations.

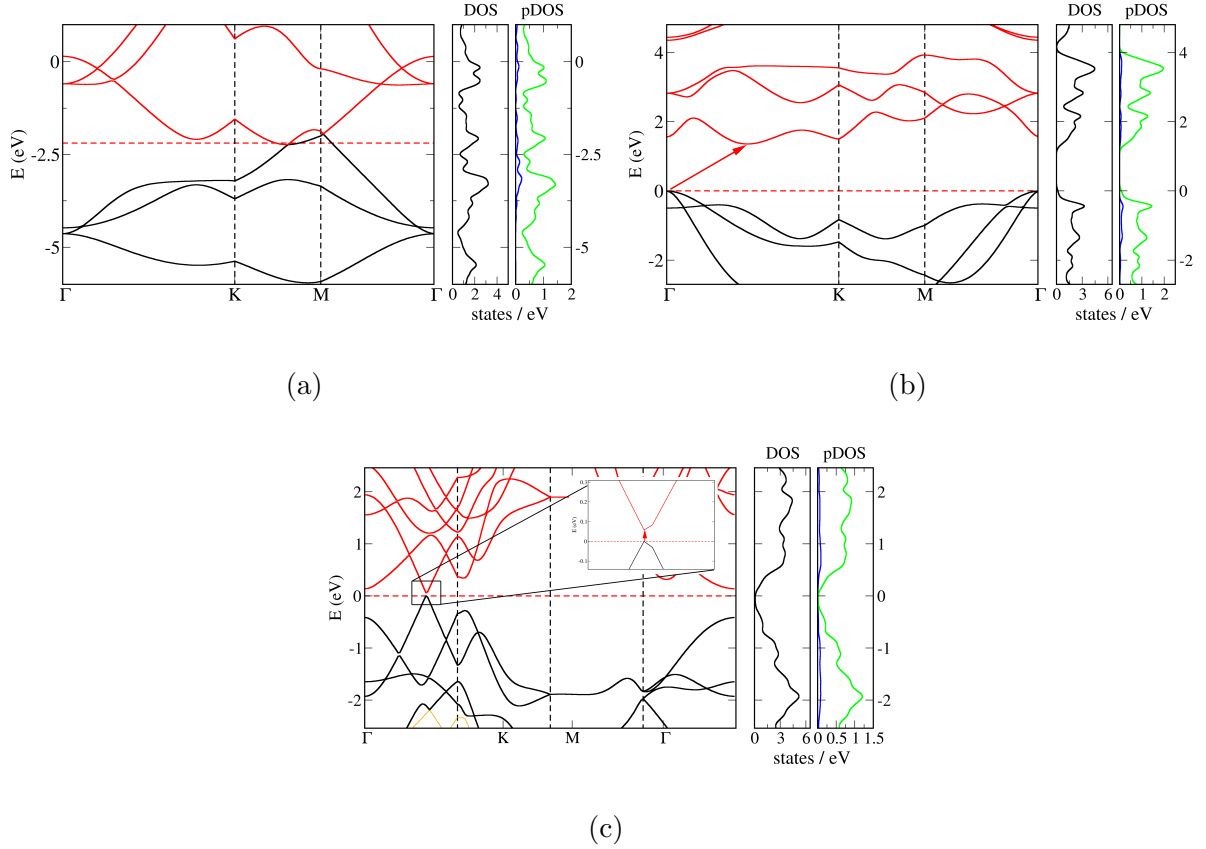


Figure 5.1: Electron band structure and density of states (DOS) of (a)  $\alpha$ , (b)  $\beta$  and (c)  $\delta$  antimonene. Black lines in the electronic band structure graph represent valence bands, while red lines represent conduction bands. Blue lines in the pDOS graph represent the s-orbitals, while green lines represent the p-orbitals. d-orbitals do not contribute to DOS in the shown energy range. The inset in (c) shows the band gap of  $\delta$ -Sb. Dashed red line represents the Fermi level  $E_F$  while the red arrow shows the band gap  $E_g$ .

### Indiene and aluminene

The electronic band structures of indiene and aluminene were given in refs. [41] and [42], respectively. Our results (Fig. D.1) also show metallic character, but we are unable to reproduce the Dirac cones at the  $K$ -point the Authors have reported in both cases. As both results were obtained within GGA, we can only attribute the differences to the pseudopotentials and parameters of the calculations used. Our pseudopotential for In contained thirteen valence electron while the one the Authors used in ref. [41] contained only three. The Authors in ref [42] used the same pseudopotential, but a much larger



$\mathbf{k}$ -mesh for integrations inside the Brillouin zone.

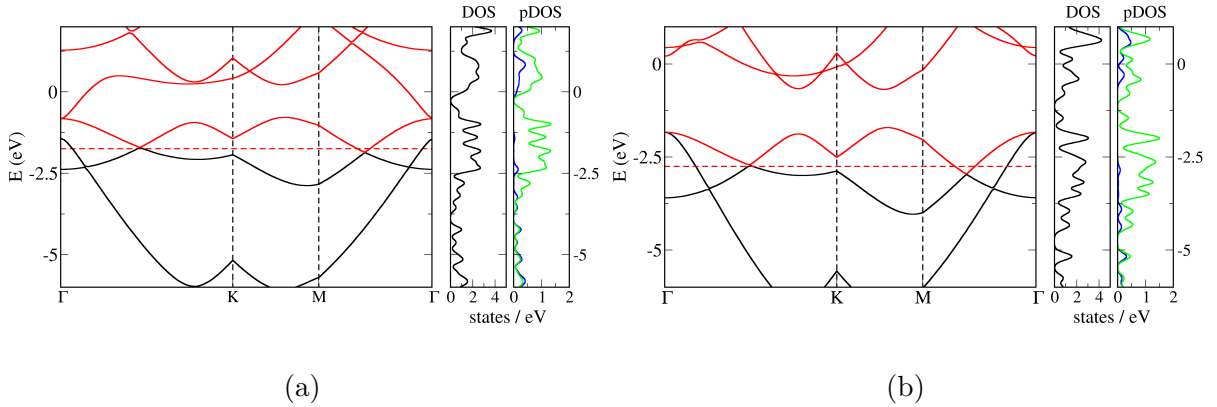


Figure 5.2: Electron band structure and density of states (DOS) of (a)  $\alpha$ -In and (b)  $\alpha$ -Al. Black lines in the electronic band structure graph represent valence bands, while red lines represent conduction bands. Blue lines in the pDOS graph represent the s-orbitals, while green lines represent the p-orbitals. d-orbitals do not contribute to DOS in the shown energy range. Dashed red line represents the Fermi level  $E_F$ .

## 5.2 Optical properties

For potential optic and optoelectronic application, optical characteristics of materials are of prime importance. Although calculated within the random phase approximation (RPA), calculated spectra can serve as a guidance for further research that would improve the results, such as including the hybrid functional corrections or excitonic effects using, for example, GW approach.

### Antimonene

We have calculated the dielectric function of antimonene allotropes (Fig. 5.3) and optical properties of antimonene allotropes (Fig. 5.4). All spectra show high degree of anisotropy with regard to the polarization of incident electromagnetic (EM) wave, which is to be expected from the strong in-plane/out-of-plane anisotropy in two-dimensional materials.  $xx$  components are virtually the same as  $yy$ , so we have included only the  $xx$  ones.  $zz$  components show almost constant values throughout the visible part of the spectrum (1.8-3.1 eV), with variations in the ultra-violet coming from high energy transitions.

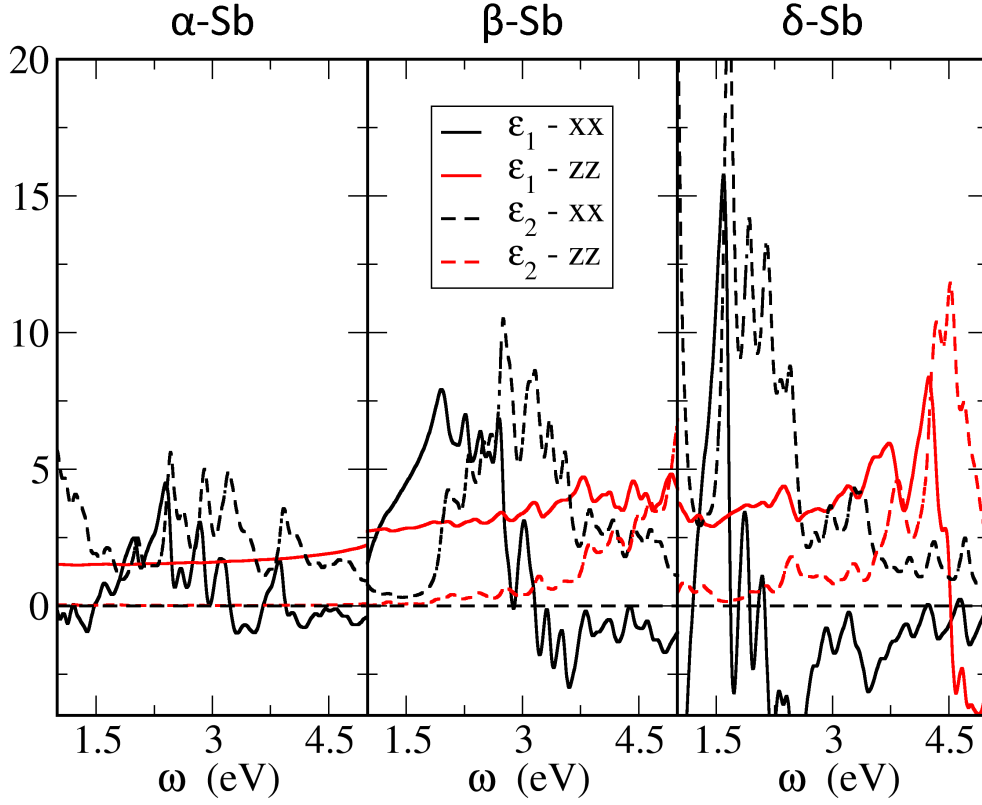


Figure 5.3: Dielectric function  $\varepsilon$  of antimonene allotropes.

The absorption spectra of all three allotropes show values below  $10^6$ , meaning none of them have extremely high absorption qualities [62]. As  $\alpha$ -Sb and  $\delta$ -Sb are a metallic and extremely small gap semiconductor, respectively, they both show absorption from small photon energies.  $\beta$ -Sb absorption starts around 1.8 eV, which is in-line with its semiconducting character.

The reflection spectra of  $\alpha$ -Sb and  $\beta$ -Sb show low values of below 40% in the visible part, increasing slightly in UV for  $\beta$ -Sb.  $\delta$ -Sb shows values in the visible part of the spectrum between 40% and 70%.

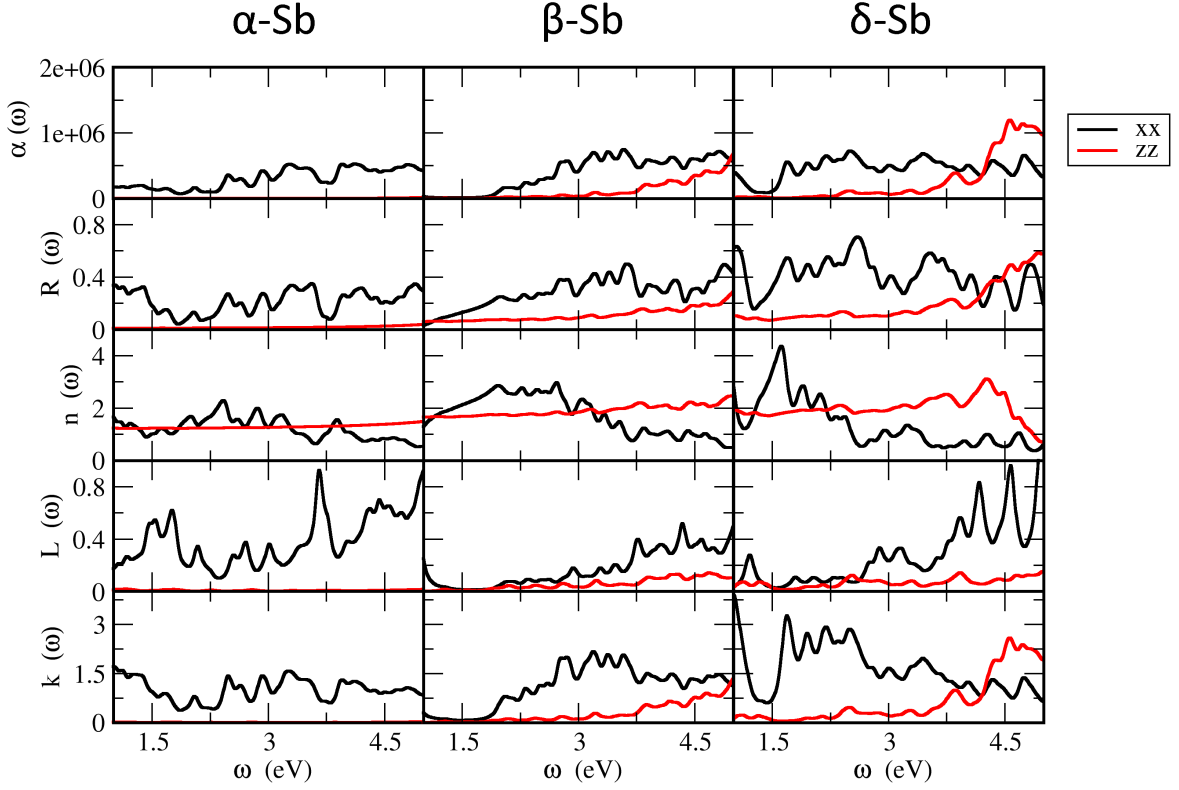


Figure 5.4: Optical properties within random phase approximation (RPA) of antimonene allotropes.  $xx$  denotes electric field polarized in-plane, while  $zz$  denotes electric field polarized out-of-plane.

The  $zz$  component of the refractive index,  $n$ , of antimonene allotropes are nearly constant throughout IR and visible parts of the spectrum, with the values 1.2, 1.7 and 1.85 for  $\alpha$ -Sb,  $\beta$ -Sb and  $\delta$ -Sb, respectively. The  $xx$  component shows some variation, though the average value for  $\alpha$ -Sb is near its  $n_z$  value. In the visible part,  $\beta$ -Sb  $n_x$  value is higher, with the average of 2.5, decreasing to below 1 in the UV.  $\delta$ -Sb shows a high peak at 1.5 eV, reaching the value of 4.2, however, quickly decreasing to below 1 values of  $\beta$ -Sb. This peak can be also seen in [18], with the value being somewhat smaller.

The peaks in the electron energy loss spectrum (EELS),  $L(\omega)$ , represent the characteristics associated with the plasma resonance and the corresponding frequency is known as plasma frequency [18]. If the incident EM wave has lower frequency than plasma frequency, plasma oscillations screen the electric field. Thus, energy loss spectrum is con-

nected with reflection, as edges in reflection spectrum correspond to peaks in  $L(\omega)$ . This is seen in all three allotropes of antimonene, but none of them are of significance, since the value of the highest peak is in the UV, per [18].

Extinction coefficient  $k(\omega)$  gives the depth at which the incident EM wave loses a portion of its intensity. The highest peaks give the shortest absorption lengths, however at considered energies the absorption lengths are significantly greater than the thickness of the monolayers, similar to the results presented in [18].

### Indiene and aluminene

The dielectric function and the optical spectra of  $\alpha$ -In and  $\alpha$ -Al are shown in Fig. 5.5-5.6. They also show anisotropic characteristics as antimonene and other two-dimensional materials. However, unlike antimonene, the  $zz$  components of the spectra show peaks at certain photon energies, around 3.8 eV in  $\alpha$ -In and around 4.3 in  $\alpha$ -Al case. The peaks are smaller or equivalent in intensity to peaks in the  $xx$  direction.

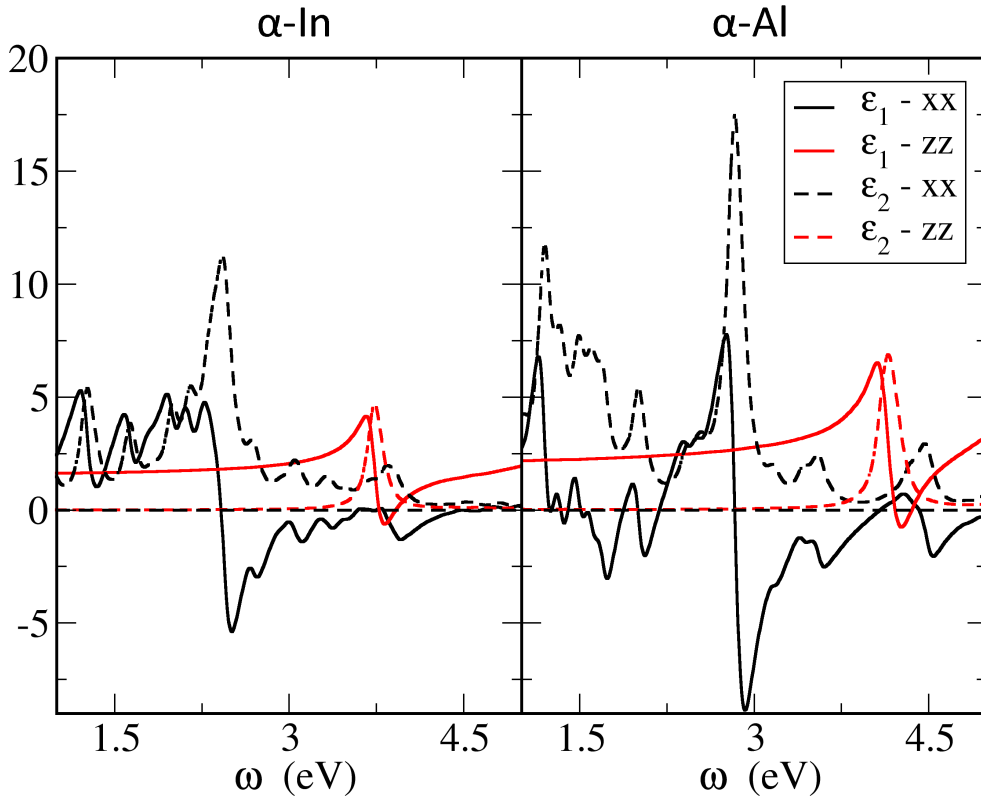


Figure 5.5: Dielectric function  $\varepsilon$  of  $\alpha$ -In and  $\alpha$ -Al allotropes.

The absorption spectrum of  $\alpha$ -In is low, with the most active region being the visible part of the spectrum. In the  $\alpha$ -Al case, the absorption peak is somewhat higher at the start of UV, but still below the value of  $10^6$  [62].

Both  $\alpha$ -In and  $\alpha$ -Al are more active regarding the reflectance, compared to antimonene.  $\alpha$ -In show reflectivity of around 60% in the visible, while  $\alpha$ -Al shows highest values of around 70% in the near-UV, with lower values in the visible part of the spectrum.

The  $zz$  component of refractive index of  $\alpha$ -In and  $\alpha$ -Al is nearly constant in the visible part of the spectrum, around 1.5. At the aforementioned energies, we can see a jump in the refractive index, but after that it returns to the same constant value. The  $xx$  component for  $\alpha$ -In drops from the average  $\sim 1.9$  to  $\sim 0.7$  in the visible part, further decreasing in the UV.  $\alpha$ -Al also has high variance in the  $xx$  component of  $n$ , going from low 0.7 in the red part to high 3.4 in the blue part of the visible spectrum, dropping to similar levels as  $\alpha$ -In in the UV.

As with the antimonene case, the electron energy loss spectrum  $L(\omega)$  and extinction  $k(\omega)$  follow the same behaviour, with the extinction coefficient giving absorption depths much larger than the thickness of the material.

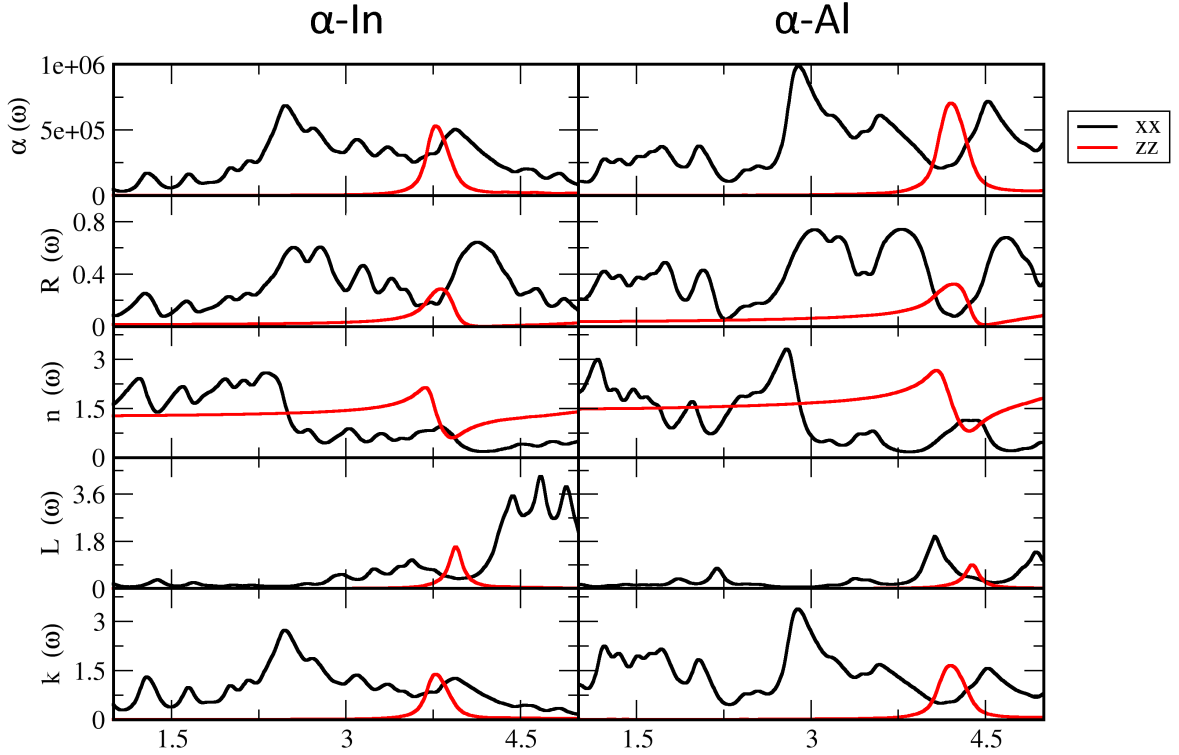


Figure 5.6: Optical properties within random phase approximation (RPA) of  $\alpha$ -In and  $\alpha$ -Al.  $xx$  denotes electric field polarized in-plane while  $zz$  denotes electric field polarized out-of-plane.

### Comparison

In this section we bring a short comparison with optical properties of other monoelemental two-dimensional materials, calculated using the same level of theory. We present previous studies on graphene [63], silicene [64], germanene[63] and borophene[65], who all show strong anisotropic properties regarding incident EM wave polarization. Comparing the absorption coefficients, all are the order of  $10^6$  and lower in the visible part of the spectrum, similar to all of our presented allotropes. Nevertheless, even this lower absorption coefficient could lead to extraordinary absorption properties of devices using 2D materials as absorbers. The reason is that a device of usual thickness would contain much larger number of monolayers than a bulk material, scaled down to the same

size [66]. The reflection of compared materials reaches maximum values of around 30%, pointing out that our allotropes  $\alpha$ -In and  $\alpha$ -Al have improved reflection properties, given that the reflection values of  $\alpha$ -In in the visible part are around 60% and  $\alpha$ -Al has high reflection values in the UV. The refraction index behaviour of our allotropes with respect to the incident EM wave shows the same behaviour as in the compared materials. Almost constant refraction index is seen with the  $zz$  component, while the  $xx$  component shows varying values throughout the sampled range of the EM spectrum. The electron energy loss spectrum values,  $L(\omega)$ , also show connection to the reflection spectrum, with  $L(\omega)$  peaks corresponding to trail ends of reflection peaks.

### 5.3 Elastic properties

We have calculated the linear elastic properties of proposed Sb, In and Al two-dimensional structures using DFPT, as per Chapter 1[67]. The results are given in table 5.1, with calculated elastic properties of other two-dimensional materials given for reference. As we can see, the stiffness given by the 2D Young modulus,  $Y_{2D}$ , is low for all calculated structures, with the most similar other materials being silicene and phosphorene. To obtain the  $Y_{2D}$  we have multiplied  $Y$  with unit cell size (20 Å). This is the method used in some studies [33], while some other studies multiply it with the monolayer thickness of 1 Å [68]. We have chosen the former method as it is unclear what should be the thickness of the monolayer material with planar geometry. This in itself gives variations in results acquired between different studies. Poisson's ratio  $\nu$ , the ratio of decrease in length of material in the direction perpendicular to the increase of length in the direction of an applied tensile strain, has much more variation. Most of the materials are closest in elastic properties with silicene, with the two exceptions of  $\alpha$ -In and  $\alpha$ -Sb.  $\alpha$ -In has very low  $\nu$ , meaning it does not shrink in the direction perpendicular to the strain, as with the armchair  $\nu$  of phosphorene.  $\alpha$ -Sb, however, has a large  $\nu$ , larger than the rest of compared 2D materials, meaning that applying tensile strain in one direction of  $\alpha$ -Sb will shrink the perpendicular length by a large amount. For reference, perfectly incompressible 3D material (constant volume) would have a Poisson's ratio of 0.5. In the two-dimensional case, a material that has constant surface when strained, meaning perpendicular axis to tensile strain shrinks by the same amount, has a Poisson's ratio of 1.

Table 5.1: Linear elastic properties of the proposed structures and other similar 2D materials.  $C_{11}$  and  $C_{12}$  are the elastic constants relevant to materials with hexagonal symmetry,  $Y_{2D}$  is the two-dimensional Young modulus, while  $\nu$  is the Poisson's ratio.

Struct.	Elem.	$C_{11}$ (GPa)	$C_{12}$ (GPa)	Y (GPa)	$Y_{2D}$ (N/m)	$\nu$	Ref.
Planar - $\alpha$							
	Al	0.170	0.052	0.154	31	0.308	
	In	0.143	0.012	0.142	28	0.085	
	Sb	0.178	0.131	0.082	13	0.734	
	C				345	0.149	[69]
	hBN				271	0.211	[69]
	MoS <sub>2</sub>				118 -141	$\sim 0.3$	[69]
Buckled - $\beta$							
	Sb	0.256	0.033	0.252	53	0.129	
	Si				60	0.4	[69]
	Sb				208	0.22	[19]
Triangular - $\gamma$							
	Al	0.242	0.118	0.184	37	0.489	
	In	0.145	0.054	0.125	25	0.372	
Puckered - $\delta$							
	P				23.0 - 92.3	0.064 - 0.703	
Bulk							
	Al			69		0.334	[70]
	In			10-13		0.445-0.455	[71]
	Sb			79-83		0.16-0.46	[19]
				55		0.25-0.33	[72, 73]

Looking at the elastic constants,  $C_{11}$  and  $C_{12}$ , from table 5.1, we can see why the values of  $Y_{2D}$  and  $\nu$  are different for each of the materials. The  $C_{11}$  notation is shorthand



for  $C_{xx,xx}$  meaning it is the force constant that depends on the variation of the position of the two atoms along the same axis, while  $C_{12}$  notation is shorthand for  $C_{xx,yy}$ , meaning it is the force constant that depends on the variation of the position of the two atoms along one axis for the first atom and along the perpendicular axis for the second atom. For the allotropes with large  $\nu$ , for example  $\alpha$ -Sb, the  $C_{12}$  is larger than in the rest of the cases, and close to the values of  $C_{11}$ . On the other hand, for  $\alpha$ -In we see a low value of  $C_{12}$ , giving a small  $\nu$ . To explain this difference in different  $\alpha$  allotropes, we turn to stress-strain relations. In Fig. 5.7, we have shown dependence of stress up to 6% tensile strain.

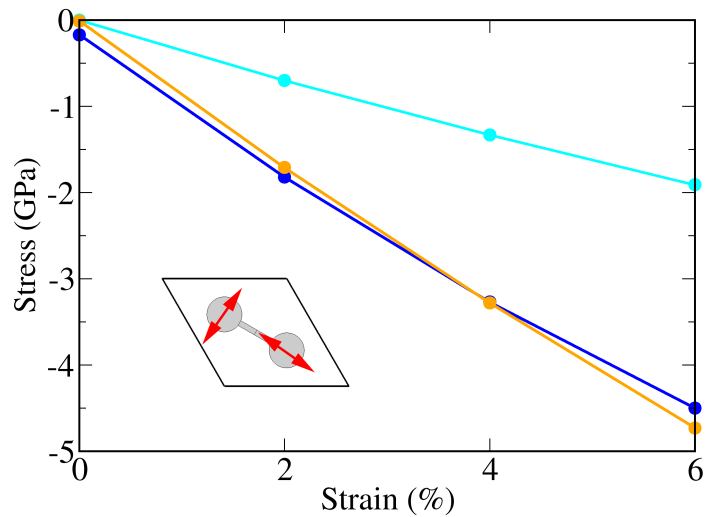


Figure 5.7: Dependence of stress on uniaxial strain (armchair and zigzag values are the same in this range). Blue line corresponds to  $\alpha$ -Sb, cyan corresponds to  $\alpha$ -In and orange corresponds to  $\alpha$ -Al. The inset shows displacements of atoms that determine the elastic constant  $C_{12}$ .

As we can see, the stress imposed on the strained structure is more than twice as much in the case of  $\alpha$ -Sb than  $\alpha$ -In, which means the bonding of individual atoms is greater in  $\alpha$ -Sb than  $\alpha$ -In - we need to impose more stress (and consequently use more energy) on the structure to deform it by the same amount - pointing to stronger overall bonding in Sb case than in In case in this type of structure. The low  $\nu$  of  $\alpha$ -In is also an indication of a more covalent type of bond [74].  $\alpha$ -Sb shows more smeared type of bonding, giving an indication to a metallic character. As the bonding is more spread out, so is the influence on the  $C_{12}$  greater.

# Chapter 6

## Conclusions

In this thesis, we have studied two-dimensional allotropes of antimony, indium and aluminium using *ab initio* simulations based on the density functional theory. Considering the lattice dynamics of proposed structures, according to our predictions only, antimonene and indiene could form stable freestanding structures,  $\beta$ -Sb and  $\alpha$ -In. Our results confirmed the results from previous studies for these allotropes, while differing in the lattice dynamic stability of  $\delta$ -Sb and  $\alpha$ -Al.

As strain influences the lattice dynamics of crystals, we have inspected the behaviour of lattice dynamics of the proposed allotropes by imposing strain in the armchair, zigzag and biaxial directions. We have used a strained hexagonal unit cell in this approach. Our results demonstrate that all antimonene allotropes have unstable lattice dynamics, which is in contrast with experimental results where all three considered allotropes were synthesized. This brought us to the conclusion that substrate-monolayer interaction beyond the imposed strain is what influences the stability of two-dimensional antimonene. Metallic substrates Ag(111) and Cu(111) only allowed the formation of  $\alpha$ -Sb, PdTe<sub>2</sub> only allowed the formation of  $\beta$ -Sb, while graphene allowed the formation of both. For indium and aluminium allotropes, we have found that a wide range of strains stabilizes their lattice dynamics, paving a way for experimental synthesis of  $\alpha$ -In and  $\alpha$ -Al by choosing a suitable substrate. Based on our calculations, Ag(111), Cu(111) and graphene are such substrates for  $\alpha$ -In, while Cu(111) and graphene are suitable for  $\alpha$ -Al. On those substrates, strains imposed on the monolayer are within the critical strains of each structure. The range of stability for  $\gamma$ -In is small, so a substrate with exact lattice mismatch is unlikely. However,  $\gamma$ -Al has a range of strains which show stable lattice dynamics, so a substrate with suit-

---

able lattice mismatch could possibly be used for experimental synthesis. Unfortunately, such substrates were not considered in this thesis.

As strain proved to be critical in stabilizing lattice dynamics of certain monolayers, it is not expected that their free-standing form could be acquired. If such a monolayer is etched from the surface of the substrate, without the imposed strain it would relax into its unstrained form, becoming unstable in the process. However, since  $\alpha$ -In has stable lattice dynamics even at 0% strain, it would be feasible to expect that it will remain in its monolayer form even after removal from the substrate.

Molecular dynamics were performed to test the substrate and monolayer stabilities at finite temperature. In our simulations, both show only thermal fluctuations at femtosecond and nanosecond scales, giving promise to their experimental realization. For allotropes which show potential for experimental synthesis, we have simulated their electronic, optical and elastic properties.

Further predictions on stable indium and aluminium allotropes could be obtained using stochastic approaches coupled with density functional theory [75]. The advantages of such an approach are speed and unbiased nature of the algorithm for generating structures only within symmetry constrains. Thus, the entire energy landscape is sampled, ensuring that acquired structures are truly the energetically most favoured ones. However, these approaches are beyond the scope of this thesis.

Also, we would like to highlight the issue of high tendency of considered elements to oxidise in the atmosphere, forming oxide compounds. For their use in potential devices, developing methods and supporting materials that decrease its oxidation sensitivity is a crucial task and possible aim of future studies. One of the solutions could be enveloping the monolayers in suitable non-reactive materials to prevent oxidation or functionalizing their surfaces with appropriate elements, like hydrogen. In contrast to this, studying oxidised forms of antimonene, indium and aluminene could be important for their possible application. Surface functionalization of the monolayers could also serve as a another way of stabilizing lattice dynamics, independent of the strain and the substrates studied in this thesis.

To further expand on the results of our research, a wider range of metallic substrates could be taken into account using the methods outlined and applied in this thesis. Since we were unable to converge the results for metallic substrates expect for Ag(111) and

---

Cu(111), perhaps another approach should be taken instead of cell relaxation, guided by the results of experiments for already synthesized two-dimensional materials.

The results of this thesis have expanded on the knowledge of mono-element single-layer structures and predicted experimental conditions for their possible synthesis. We have used a novel method for straining the crystal lattice to find the ranges of lattice stability for proposed new two-dimensional materials. By studying the monolayers on substrates, we have identified the conditions of their experimental synthesis: (i) type and the symmetry of the substrate, (ii) required strain for acquiring their stable lattice dynamics and (iii) appropriate temperature conditions for their synthesis. Characterization of the proposed structures revealed their optical activity in visible and UV parts of the electromagnetic spectrum, while they also showed wide range of elastic properties. We hope the results of this thesis will guide the new studies of their experimental synthesis, as well as further expanding their characteristics with improved theoretical methods.

# Appendix A

## Computational details

In this appendix we present computational details used in the making of this thesis. Calculations were performed within formalism presented in Chapter 1, using computer codes Quantum ESPRESSO and ABINIT. Exchange-correlation energy was calculated within the GGA approach. Results were obtained using the plane-wave approach and integrations over the Brillouin zone were replaced by a sum over discrete set of points as per ref. [21].

### A.1 Pseudopotentials

Pseudopotentials used are available online at pseudopotential repository of QUANTUM ESPRESSO [36]. They were used without alterations. We have used ultrasoft pseudopotentials for obtaining structural parameters and the phonon dispersions of the ground state, strain, substrate, electron band structures, density of states (DOS), charge density and molecular dynamics calculations. Certain calculations were repeated with norm-conserving pseudopotentials. Norm-conserving pseudopotentials were used for obtaining the optical properties.

Ultrasoft pseudopotentials used for Sb atoms were obtained using Perdew-Wang parametrization [28], while ultrasoft pseudopotentials for In, Al, Ag, Cu and C atoms were obtained using Perdew-Burke-Ernzerhof parametrization [29]. All the norm-conserving pseudopotentials were obtained using the procedure outlined in [76], with Perdew-Burke-Ernzerhof parametrization. Valence electron configurations of the used pseudopotentials are given in table A.1.

Table A.1: Valence electron configurations of used pseudopotentials. Index NC denotes norm-conserving pseudopotentials, while the index US denotes ultrasoft pseudopotentials.

Element	Configuration
Al <sub>NC</sub>	$1s^2 2s^2 2p^6 3s^2 3p^1$
Al <sub>US</sub>	$3s^2 3p^1$
Ag	$5s^1 5p^0 4d^{10}$
C	$2s^2 2p^2$
Cu	$4s^1 4p^0 3d^{10}$
In <sub>NC</sub>	$5s^2 5p^1 4d^{10}$
In <sub>US</sub>	$5s^2 5p^1 4d^{10}$
Sb <sub>NC</sub>	$5s^2 5p^3 4d^{10}$
Sb <sub>US</sub>	$5s^2 5p^3 4d^{10}$

## A.2 Convergence

We have tested total energy convergence for cut-off energy of plane wave basis  $E_{cut}$  and the  $\mathbf{k}$ -mesh for the sampling of the Brillouin zone. We have set the total energy convergence threshold at 0.001 eV. As phonon frequencies depend on higher derivatives of total energy, we have tested their convergence on the parameters of  $E_{cut}$  and the  $\mathbf{k}$ -mesh. Converged parameters are shown in table A.2. We have only presented the convergence parameters for phonon convergence, as all the parameters for the total energy convergence are lower. As phonon dispersion calculations demand sequence of calculations - unit cell optimization, self-consistent calculation and phonon dispersion calculations - with subsequent calculations depending on the results of the previous, we have shown the results only for the structural parameters obtained at the higher convergence parameters. All the phonon dispersion under strain were calculated for the convergence parameters of the unstrained structure. Converged parameters for calculations on substrates are shown in table A.3. During the structural relaxation, we have set the scf convergence threshold for forces acting on atoms at  $0.005 \text{ eV} / \text{\AA}^{-1}$  and stresses at  $0.5 \times 10^{-4} \text{ kbar}$ . As the height of the unit cell  $c$  is large, the corresponding dimension in the reciprocal space is small, so 1 k-point is enough to sample it.

Table A.2: Results of the ground state energy and phonon frequencies convergence for free-stranding monolayers.

Struct.	Elem.	$E_{cut}$ (Ry)	$\mathbf{k}$ -mesh
Planar - $\alpha$			
	Al	80	$8 \times 8 \times 1$
	In	70	$10 \times 10 \times 1$
	Sb	60	$16 \times 16 \times 1$
Buckled - $\beta$			
	Sb	80	$20 \times 20 \times 1$
Triangular - $\gamma$			
	Al	40	$16 \times 16 \times 1$
	In	100	$16 \times 16 \times 1$
Puckered - $\delta$			
	Sb	70	$14 \times 14 \times 1$

Table A.3: Results of the ground state energy convergence for substrates.

Struct.	Elem.	$E_{cut}$ (Ry)	$\mathbf{k}$ -mesh
Sb on substrate			
	Ag	70	$10 \times 10 \times 1$
	C	70	$8 \times 8 \times 1$
	Cu	80	$8 \times 8 \times 1$
In on substrate			
	Ag	80	$8 \times 8 \times 1$
	C	70	$10 \times 10 \times 1$
	Cu	80	$10 \times 10 \times 1$
Al on substrate			
	Ag	80	$8 \times 8 \times 1$
	C	120	$10 \times 10 \times 1$
	Cu	80	$8 \times 8 \times 1$

# Appendix B

## Indiene and aluminene in buckled and puckered allotropic modifications

To further show what happens with the structures  $\beta$ - and  $\delta$ - of Al and In during structural relaxation, we calculated total electronic energy per atom,  $E_{tot}$ , and cohesive energies,  $E_{coh}$ . The final, relaxed structures, in the main text referred to as the bilayers of the  $\gamma$  structure, all have total energies and cohesive energies lower than the starting 'true'  $\beta$  and  $\delta$  structures, showing that the bilayer is energetically preferred structure.

Table B.1: Total and cohesion energy of buckled honeycomb and puckered indium and aluminium structures initially and post relaxation.

		<i>Initially</i>		<i>Post</i>	
Structure	Element	$E_{tot}$ (eV/atom)	$E_{coh}$ (eV/atom)	$E_{tot}$ (eV/atom)	$E_{coh}$ (eV/atom)
Buckled					
	Al	-73.417	-2.39	-74.163	-3.13
	In	-1970.101	-1.62	-1970.560	-2.08
Puckered					
	Al	-72.879	-1.85	-74.084	-3.06
	In	-1970.343	-1.87	-1970.543	-2.08



# Appendix C

## Lattice dynamics under compressive strain

Imposing a compressive strain on all of the proposed allotropes yielded imaginary phonon frequencies. As an example, we provide the behaviour of the lowest phonon mode of  $\alpha$ -In when strained in the armchair, zigzag or biaxial directions up to -10% (Fig. C.1).

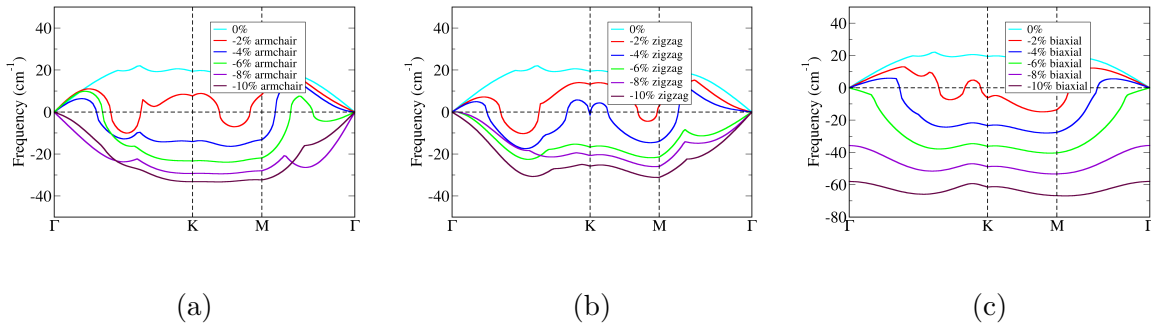


Figure C.1: Lowest phonon mode of (a) armchair, (b) zigzag and (c) biaxially strained  $\alpha$ -In.

We have noticed development of instabilities with compressive strain in similar research of other two-dimensional materials [77, 78].

# Appendix D

## Characterization of triangular structures

### D.1 Electronic band structure

Both  $\gamma$ -In and  $\gamma$ -Al have metallic character, as seen in Fig. D.1. Unlike  $\alpha$ -In and  $\alpha$ -Al, s-orbitals and p-orbitals both contribute to valence and conduction bands, revealing s-p hybridization. In  $\alpha$ -In and  $\alpha$ -Al, valence and conduction bands are made mostly of p-orbitals. Dirac cones are seen at three different points of the Brillouin zone.

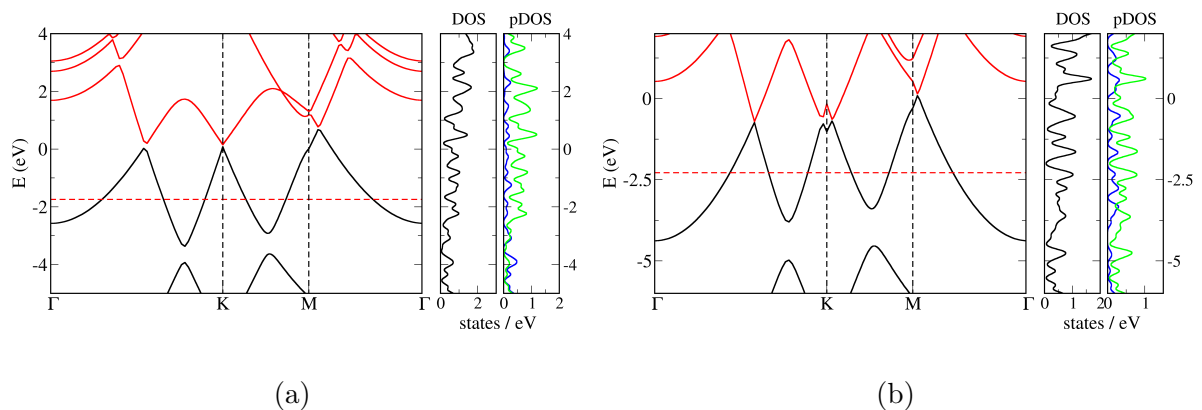


Figure D.1: Electron band structure and density of states (DOS) of (a)  $\gamma$ -In and (b)  $\gamma$ -Al. Black lines in the electronic band structure graph are valence bands, while red lines are conduction bands. Blue lines in the pDOS graph are the s-orbitals, while green lines are the p-orbitals. d-orbitals do not contribute to DOS in the shown energy range. Dashed red line is the Fermi level  $E_F$ .

## D.2 Optical properties

Optical properties of  $\gamma$ -In and  $\gamma$ -Al also show anisotropy, as other two-dimensional materials. Due to smaller amount electronic bands, the spectra have lower amount of features. The peaks in the  $zz$  components at photon energies of 4.2 eV and 3.8 eV, for  $\gamma$ -In and  $\gamma$ -Al respectively, are also present. All spectra show periodic properties in the  $xx$  component.

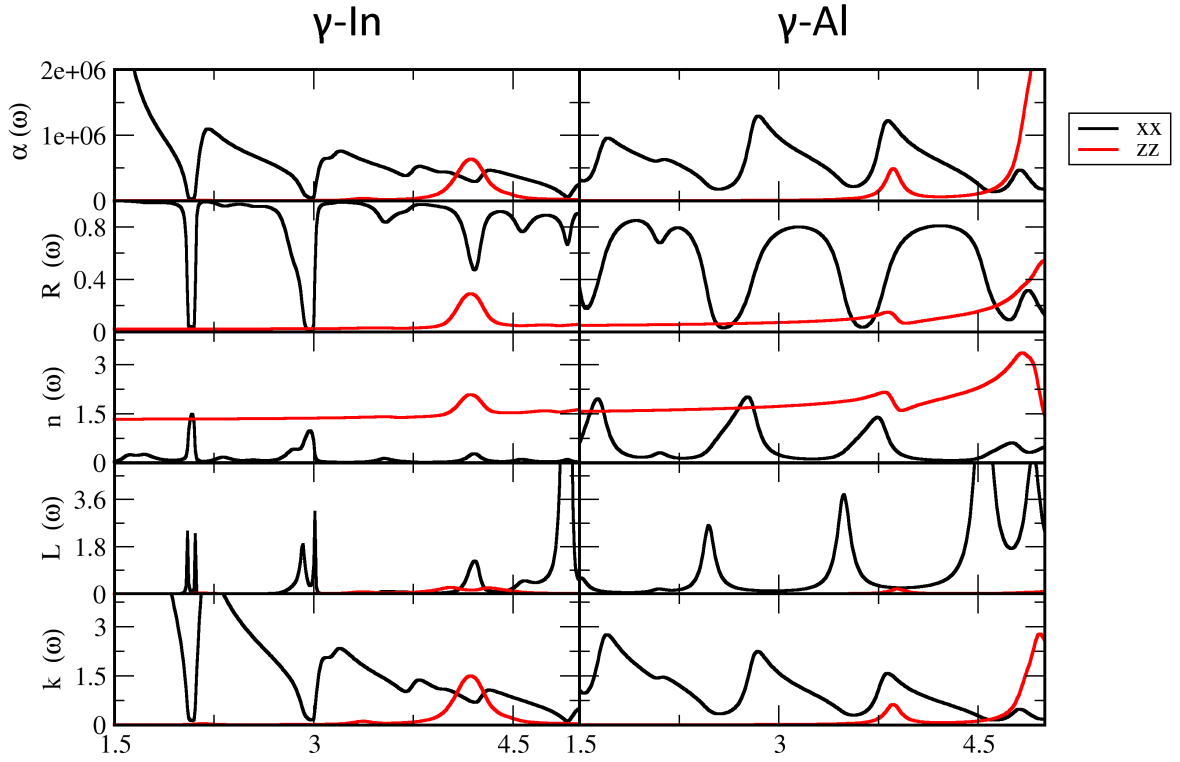


Figure D.2: Optical properties within random phase approximation (RPA) of  $\gamma$ -In and  $\gamma$ -Al.  $xx$  denotes electric field polarized in-plane while  $zz$  denotes electric field polarized out-of-plane.

# List of Figures

1.1	Algorithm for iterative self-consistent solution to Kohn-Sham equations. Taken from reference [32]. . . . .	13
1.2	Illustration of an all-electron wavefunction and potential (solid lines) and pseudowavefunction and pseudopotential (dashed lines). Radius beyond which they match is designated with $r_c$ . Taken from reference [32]. . . . .	14
2.1	(a) top and (b) side view of $\alpha$ -structure, with in-plane unit cell vectors $\mathbf{a}_1$ and $\mathbf{a}_2$ , and bond angle $\alpha$ . Unit cell is shaded gray. Numbers denote atomic positions from 2.2. . . . .	24
2.2	The first Brillouin zone of hexagonal unit cell and its high symmetry points.	25
2.3	(a) top and (b) side view of $\beta$ -structure, with in-plane unit cell vectors $\mathbf{a}_1$ and $\mathbf{a}_2$ . Two sublattices are designated with different colors. Bottom sublattice atoms are coloured yellow, while top sublattice atoms are coloured blue. Bond length is designated as $R$ and the angle between bonds is designated as $\alpha$ . Unit cell is shaded gray. Numbers denote atom positions from 2.5. . . . .	26
2.4	Top view of $\gamma$ -structure, with in-plane unit cell vectors $\mathbf{a}_1$ and $\mathbf{a}_2$ , and bond angle $\alpha$ . Unit cell is shaded gray. Numbers denote atom positions from 2.8.	27
2.5	(a) top and (b) side view of $\delta$ -structure, with in-plane unit cell vectors $\mathbf{a}_1$ and $\mathbf{a}_2$ . Two sublattices are designated with different colors. Yellow colour is the bottom, while blue is the top sublattice. Bonds are designated with $R_1$ and $R_2$ , while bond angles are designated as $\alpha$ and $\beta$ . Unit cell is shaded gray. Numbers denote atom positions from 2.11. . . . .	28
2.6	The first Brillouin zone of orthorombic unit cell and its high symmetry points. . . . .	29

2.7	Dependence of total electronic energy $E_{tot}$ per atom (coloured triangles) and pressure (black squares) on lattice constant for (a) $\alpha$ , (b) $\beta$ , (c) $\delta$ antimonene allotropes, (d) $\alpha$ and (e) $\gamma$ indiene allotropes and (f) $\alpha$ and (g) $\gamma$ aluminene allotropes from table 2.1. Dashed lines give equilibrium lattice constants $a_0$ (blue for Sb, cyan for In, orange for Al) and $b_0$ (purple for Sb). . . . .	31
2.8	(a) Dependence of total electronic energy $E_{tot}$ (black squares) and interlayer distance $h$ (brown triangles) on lattice constant $a$ for the proposed structure of $\beta$ -In. Equilibrium $E_{tot}$ and $h$ are emphasized with broken lines. Insets show the relaxed structures for a given lattice constant. Red arrows indicate progression of the starting, two intermediate and the final $\beta$ -In structure. (b) Charge density between sublayers of fully relaxed " $\beta$ -In", showing no charge in the interlayer space. . . . .	33
2.9	Phonon dispersions of (a) $\alpha$ , (b) $\beta$ and (c) $\delta$ antimonene allotropes. Phonon modes with imaginary frequencies are shown in red colour. . . . .	35
2.10	Phonon dispersions of (a) $\alpha$ and (b) $\gamma$ indiene allotropes. Phonon mode with imaginary frequencies are shown in red colour. . . . .	37
2.11	Phonon dispersions of (a) $\alpha$ and (b) $\gamma$ aluminene allotropes. Phonon modes with imaginary frequencies are shown in red colour. . . . .	38
3.1	Armchair and zigzag strain directions. Left cut of the lattice is the zigzag termination of the crystal, while on the bottom (top) one is the armchair termination. . . . .	40
3.2	Strain directions for (a) puckered and (b) triangular structure. . . . .	41
3.3	Strain-modified unit cell of honeycomb and triangular structures in (a) armchair and (b) zigzag directions. $a$ is the unstrained lattice constant while $a'$ is the new, strained, lattice constant. Unstrained unit cell is shaded in gray. . . . .	41
3.4	Stress-strain relations for (a) $\alpha$ -Sb, (b) $\beta$ -Sb and (c) $\delta$ -Sb allotropes, (d) $\alpha$ -In and (e) $\gamma$ -In allotropes and (f) $\alpha$ -Al and (g) $\gamma$ -Al allotropes. Critical strains are denoted as $\varepsilon_{crit}$ . Missing points indicate failures in the convergence of the calculations. . . . .	43

3.5	(a) Phonon dispersions of (a) armchair, (b) zigzag and (c) biaxially strained $\alpha$ -Sb. A stabilization of one of the modes can be seen. Strain percentages are given in legends. . . . .	45
3.6	(a) Phonon dispersions of armchair strained $\beta$ -Sb. (b) Phonon dispersions of zigzag strained $\beta$ -Sb. Strain percentages are given in legends. . . . .	46
3.7	(a) Phonon dispersions of armchair strained $\delta$ -Sb. (b) Phonon dispersions of zigzag strained $\delta$ -Sb. Strain percentages are given in legends. . . . .	46
3.8	(a) Phonon dispersions of armchair and zigzag strained $\alpha$ -In. (b) Phonon dispersions of $\alpha$ -In strained in the zigzag direction by 18%, showing imaginary frequencies near the $\Gamma$ point in the M- $\Gamma$ direction. Strain percentages are given in legends. . . . .	47
3.9	Phonon dispersions of (a) armchair, (b) zigzag and (c) biaxially strained $\gamma$ -In. Strain percentages are given in legends. . . . .	48
3.10	Phonon dispersions of (a) armchair, (b) zigzag and (c) biaxially strained $\alpha$ -Al. Strain percentages are given in legends. . . . .	48
3.11	Phonon dispersions of (a) armchair and zigzag and (b) biaxially tensile strained $\alpha$ -Al. Strain percentages are given in legends. . . . .	49
3.12	Lattice dynamics stability of two-dimensional allotropes in relation to strain imposed. Red areas denote unstable lattice dynamics, green areas stable lattice dynamics, while black areas are errors in the calculations. . . . .	50
4.1	Surface potential of Ag(111). Ag atoms are coloured in gray. Hexagon tips coloured in yellow represent the minima of the potential energy. . . . .	52
4.2	(a) top and (b) side view of relaxed $\alpha$ -Sb and $\beta$ -Sb structures on Ag(111). Sb atoms are coloured in blue, while the top layer of Ag atoms are coloured in pink. The remaining Ag atoms are coloured in white. (c) top and (d) side view of relaxed $\alpha$ -Sb and $\beta$ -Sb structures on PdTe <sub>2</sub> . Sb atoms are coloured in blue, Pd atoms are coloured in black, while Te atoms are coloured in yellow. Bond lengths are designated with $R_1$ and $R_2$ (R if they are the same), the bond angles are designated as $\alpha$ and $\beta$ . Minimum and maximum distances between the substrate and the monolayer are designated as $h_{min}$ and $h_{max}$ (h if they are the same), while $h_\beta$ is the $\beta$ -Sb interlayer distance. . . . .	56

4.3	(a) top and (b) side view of relaxed $\alpha$ -In on Cu(111). In atoms are coloured in turquoise, while the top layer of Cu atoms are coloured in pink. The remaining Cu atoms are coloured in brown. The Bond length is designated with R, the bond angle is designated with $\alpha$ and the distance between the substrate and the monolayer is designated as h. . . . .	59
4.4	(a) top and (b) side view of relaxed $\alpha$ -Al on graphene. Al atoms are coloured in orange, while the C atoms are coloured in pink. The Bond length is designated with R, the bond angle is designated with $\alpha$ and the distance between the substrate and the monolayer is designated as h. . . . .	60
4.5	Molecular dynamics of $\alpha$ -Al on Cu(111). Al atoms are coloured in pink, while Cu atoms are coloured in brown. (a) $t = 1$ ps (b) $t = 350$ ps (c) $t = 700$ ps (d) $t = 1000$ ps . . . . .	61
4.6	Radial distribution functions $g(r)$ of $\alpha$ -Sb on (a) Ag(111), (b) Cu(111) and (c) graphene; $\alpha$ -In on (d) Ag(111), (e) Cu(111) and (f) graphene and $\alpha$ -Al on (g) Cu(111) and (h) graphene. . . . .	62
5.1	Electron band structure and density of states (DOS) of (a) $\alpha$ , (b) $\beta$ and (c) $\delta$ antimonene. Black lines in the electronic band structure graph represent valence bands, while red lines represent conduction bands. Blue lines in the pDOS graph represent the s-orbitals, while green lines represent the p-orbitals. d-orbitals do not contribute to DOS in the shown energy range. The inset in (c) shows the bang gap of $\delta$ -Sb. Dashed red line represents the Fermi level $E_F$ while the red arrow shows the band gap $E_g$ . . . . .	64
5.2	Electron band structure and density of states (DOS) of (a) $\alpha$ -In and (b) $\alpha$ -Al. Black lines in the electronic band structure graph represent valence bands, while red lines represent conduction bands. Blue lines in the pDOS graph represent the s-orbitals, while green lines represent the p-orbitals. d-orbitals do not contribute to DOS in the shown energy range. Dashed red line represents the Fermi level $E_F$ . . . . .	65
5.3	Dielectric function $\varepsilon$ of antimonene allotropes. . . . .	66
5.4	Optical properties within random phase approximation (RPA) of antimonene allotropes. $xx$ denotes electric field polarized in-plane, while $zz$ denotes electric field polarized out-of-plane. . . . .	67

---

5.5	Dielectric function $\varepsilon$ of $\alpha$ -In and $\alpha$ -Al allotropes. . . . .	68
5.6	Optical properties within random phase approximation (RPA) of $\alpha$ -In and $\alpha$ -Al. $xx$ denotes electric field polarized in-plane while $zz$ denotes electric field polarized out-of-plane. . . . .	70
5.7	Dependence of stress on uniaxial strain (armchair and zigzag values are the same in this range). Blue line corresponds to $\alpha$ -Sb, cyan corresponds to $\alpha$ -In and orange corresponds to $\alpha$ -Al. The inset shows displacements of atoms that determine the elastic constant $C_{12}$ . . . . .	73
C.1	Lowest phonon mode of (a) armchair, (b) zigzag and (c) biaxially strained $\alpha$ -In. . . . .	81
D.1	Electron band structure and density of states (DOS) of (a) $\gamma$ -In and (b) $\gamma$ -Al. Black lines in the electronic band structure graph are valence bands, while red lines are conduction bands. Blue lines in the pDOS graph are the s-orbitals, while green lines are the p-orbitals. d-orbitals do not contribute to DOS in the shown energy range. Dashed red line is the Fermi level $E_F$ . . . . .	82
D.2	Optical properties within random phase approximation (RPA) of $\gamma$ -In and $\gamma$ -Al. $xx$ denotes electric field polarized in-plane while $zz$ denotes electric field polarized out-of-plane. . . . .	83



# List of Tables

2.1	Optimised parameters of aluminium, indium and antimony in the relaxed monolayer structures, where $E_{coh}/\text{atom}$ is the cohesion energy per atom of the unit cell, $a$ and $b$ are lattice constants, $h$ is the interlayer distance, $\alpha$ and $\beta$ are angles between bonds and $R_1$ and $R_2$ are bond lengths as denoted in Section 2.1. . . . .	30
3.1	Critical strains in armchair and zigzag strain directions of antimonene, indiene and aluminene allotropes. . . . .	44
4.1	Lattice mismatch, bond lengths $R_1$ , $R_2$ and bond angles $\alpha$ , $\beta$ after relaxation of monolayers on substrates. . . . .	54
5.1	Linear elastic properties of the proposed structures and other similar 2D materials. $C_{11}$ and $C_{12}$ are the elastic constants relevant to materials with hexagonal symmetry, $Y_{2D}$ is the two-dimensional Young modulus, while $\nu$ is the Poisson's ratio. . . . .	72
A.1	Valence electron configurations of used pseudopotentials. Index NC denotes norm-conserving pseudopotentials, while the index US denotes ultrasoft pseudopotentials. . . . .	78
A.2	Results of the ground state energy and phonon frequencies convergence for free-stranding monolayers. . . . .	79
A.3	Results of the ground state energy convergence for substrates. . . . .	79
B.1	Total and cohesion energy of buckled honeycomb and puckered indium and aluminium structures initially and post relaxation. . . . .	80

# Bibliography

- [1] K. S. Novoselov, A. K. Geim, S. V. Morozov, et al. “Electric Field Effect in Atomically Thin Carbon Films”. *Science* 306.5696 (2004), pp. 666–669.
- [2] S. Das Sarma, S. Adam, E. H. Hwang, et al. “Electronic transport in two-dimensional graphene”. *Rev. Mod. Phys.* 83 (2 2011), pp. 407–470.
- [3] A. S. Mayorov, R. V. Gorbachev, S. V. Morozov, et al. “Micrometer-Scale Ballistic Transport in Encapsulated Graphene at Room Temperature”. *Nano Lett.* 11.6 (2011), pp. 2396–2399.
- [4] C. Lee, X. Wei, J. W. Kysar, et al. “Measurement of the Elastic Properties and Intrinsic Strength of Monolayer Graphene”. *Science* 321.5887 (2008), pp. 385–388.
- [5] A. A. Balandin. “Thermal properties of graphene and nanostructured carbon materials”. *Nat. Mater.* 10 (2011), pp. 569–581.
- [6] Manzeli S., Ovchinnikov D., Pasquier D., et al. “2D transition metal dichalcogenides”. *Nature Reviews Materials* 2.17033 (2017).
- [7] J. Zhao, H. Liu, Z. Yu, et al. “Rise of silicene: A competitive 2D material”. *Prog. Mater. Sci.* 83 (2016), pp. 24–151.
- [8] M. E. Dávila, L. Xian, S. Cahangirov, et al. “Germanene: a novel two-dimensional germanium allotrope akin to graphene and silicene”. *New J. Phys.* 16.9 (2014), p. 095002.
- [9] J. Yuhara, H. Shimazu, K. Ito, et al. “Germanene Epitaxial Growth by Segregation through Ag(111) Thin Films on Ge(111)”. *ACS Nano* 12.11 (2018), pp. 11632–11637.
- [10] Z.-Q. Wang, T.-Y. Lu, H.-Q. Wang, et al. “Review of borophene and its potential applications”. *Front. Phys.* 14.2 (2019), p. 23403.

- 
- [11] H. Liu, A. T. Neal, Z. Zhu, et al. “Phosphorene: An Unexplored 2D Semiconductor with a High Hole Mobility”. *ACS Nano* 8.4 (2014), pp. 4033–4041.
- [12] S. Zhang, S. Guo, Z. Chen, et al. “Recent progress in 2D group-VA semiconductors: from theory to experiment”. *Chem. Soc. Rev.* 47 (3 2018), pp. 982–1021.
- [13] Y. Shao, Z-L. Liu, C. Cheng, et al. “Epitaxial Growth of Flat Antimonene Monolayer: A New Honeycomb Analogue of Graphene”. *Nano Lett.* 18.3 (2018), pp. 2133–2139.
- [14] Y. Shao X. Wu, H. Liu, and Z. Feng. “Epitaxial Growth and Air-Stability of Monolayer Antimonene on PdTe<sub>2</sub>”. *Adv. Mater.* 29.11 (2017), p. 1605407.
- [15] M. Fortin-Deschenes, O. Waller, T. Onur Menten, et al. “Synthesis of Antimonene on Germanium”. *Nano Lett.* 17.8 (2017), pp. 4970–4975.
- [16] H. Li Z.-Q. Shi, Q.-Q. Yuan, and Y.-H. Song. “Van der Waals Heteroepitaxial Growth of Monolayer Sb in a Puckered Honeycomb Structure”. *Adv. Mater* 31 (2019).
- [17] G. Wang, R. Pandey, and S. P. Karna. “Atomically Thin Group V Elemental Films: Theoretical Investigations of Antimonene Allotropes”. *ACS Appl. Mater. Interfaces* 7 (2015), pp. 11490–11496.
- [18] D. Singh, S. K. Gupta, Y. Sonvane, et al. “Antimonene: a monolayer material for ultraviolet optical nanodevices”. *J. Mater. Chem. C* 4 (26 2016), pp. 6386–6390.
- [19] D. R. Kripalani, A. A. Kistanov, Y. Cai, et al. “Strain engineering of antimonene by a first-principles study: Mechanical and electronic properties”. *Phys. Rev. B* 98 (8 2018), p. 085410.
- [20] H. Liu, J. Gao, and J. Zhao. “From Boron Cluster to Two-Dimensional Boron Sheet on Cu(111) Surface: Growth Mechanism and Hole Formation”. *Sci. Rep.* 3.3238 (2013).
- [21] H. J. Monkhorst and J. D. Pack. “Special points for Brillouin-zone integrations”. *Phys. Rev. B* 13 (12 1976), pp. 5188–5192.
- [22] R. P. Feynman. “Forces in Molecules”. *Phys. Rev.* 56 (4 1939), pp. 340–343.
- [23] C. G. Broyden. “The Convergence of a Class of Double-rank Minimization Algorithms”. *IMA J. Appl. Math.* 6 (1 1970), pp. 76–90.

- 
- [24] R. M. Martin. *Electronic structure. Basic theory and practical methods*. Cambridge University Press, Cambridge, 2004.
- [25] P. Hohenberg and W. Kohn. “Inhomogeneous Electron Gas”. *Phys. Rev.* 136 (3B 1964), B864–B871.
- [26] A. Szabo and N. S. Ostlund. *Modern quantum chemistry. Introduction to advanced electronic structure theory*. Dover publications, inc., New York, 1947.
- [27] W. Kohn and L. J. Sham. “Self-Consistent Equations Including Exchange and Correlation Effects”. *Phys. Rev.* 140.A1133 (1965).
- [28] K. Burke, J. P. Perdew, and Y. Wang. “Derivation of a generalized gradient approximation: The PW91 Density functional”. *Electronic density functional theory: Recent Progress and New Directions*. Springer US, 1998, pp. 81–111.
- [29] J. P. Perdew, K. Burke, and M. Ernzerhof. “Generalized Gradient Approximation Made Simple”. *Phys. Rev. Lett.* 77.18 (1996).
- [30] J. Hubbard. “Electron Correlations in Narrow Energy Bands”. *Proc. Roy. Soc. London* 276 (1365 1965).
- [31] A. Cohen, P. Mori-Sánchez, and W. Yang. “Challenges for Density Functional Theory”. *Chem. Rev.* 112.1 (2011).
- [32] M. C. Payne, M. P. Teter, D. C. Allan, et al. “Iterative minimization techniques for ab initio total-energy calculations: molecular dynamics and conjugate gradients”. *Rev. Mod. Phys.* 64.4 (1992).
- [33] R. C. Andrew, R. E. Mapasha, and A. M. Ukpong. “Mechanical properties of graphene and boronitrene”. *Phys. Rev. B* 85.125428 (2012).
- [34] D. R. Hamman, X. Wu, and K. M. Rabe. “Metric tensor formulation of strain in density-functional perturbation theory”. *Phys. Rev. B* 71.035117 (2005).
- [35] H. Kuzmany. *Solid-State Spectroscopy*. Springer, Berlin, 2009.
- [36] P. Gianozzi, O. Andreussi, and T. Brumme. “Advanced capabilities for materials modelling with Quantum ESPRESSO”. *J. Phys.: Condens. Matter* 29.465901 (2017).
- [37] X. Gonze, F. Jollet, and F. Abreu Araujo. “Recent developments in the ABINIT software package”. *Comput. Phys. Commun.* 205 (2016), pp. 106–131.

- [38] A. K. Geim. “Graphene: Status and Prospects”. *Science* 324.5934 (2009), pp. 1530–1534.
- [39] A. H. Woomer, T. W. Farnsworth, J. Hu, et al. “Phosphorene: Synthesis, Scale-Up, and Quantitative Optical Spectroscopy”. *ACS Nano* 9.9 (2015), pp. 8869–8884.
- [40] H. Şahin, S. Cahangirov, M. Topsakal, et al. “Monolayer honeycomb structures of group-IV elements and III-V binary compounds: First-principles calculations”. *Phys. Rev. B* 80 (15 2009), p. 155453.
- [41] D. Singh, S. K. Gupta, I. Lukačević, et al. “Indiene 2D monolayer: a new nanoelectronic material”. *RSC Adv.* 6 (10 2016), pp. 8006–8014.
- [42] C. Kamal, A. Chakrabarti, and M. Ezawa. “Aluminene as highly hole-doped graphene”. *New. J. Phys.* 17.083014 (2015).
- [43] E. Scalise, M. Houssa, G. Pourtois, et al. “Vibrational properties of silicene and germanene”. *Nano Research* 6.1 (2013), pp. 19–28.
- [44] C. Kamal and M. Ezawa. “Arsenene: Two-dimensional buckled and puckered honeycomb arsenic systems”. *Phys. Rev. B* 91 (8 2015), p. 085423.
- [45] B. Cai, S. Zhang, Z.u Hu, et al. “Tinene: a two-dimensional Dirac material with a 72 meV band gap”. *Phys. Chem. Chem. Phys.* 17 (19 2015), pp. 12634–12638.
- [46] A. J. Mannix, X.-F. Zhou, B. Kiraly, et al. “Synthesis of borophenes: Anisotropic, two-dimensional boron polymorphs”. *Science* 350.6267 (2015), pp. 1513–1516.
- [47] Y. Sun, D. Wang, and Z. Shuai. “Puckered Arsenene: A Promising Room-Temperature Thermoelectric Material from First-Principles Prediction”. *J. Phys. Chem. C* 121 (2017), pp. 19080–19086.
- [48] Q. Wei and X. Peng. “Superior mechanical flexibility of phosphorene and few-layer black phosphorus”. *Appl. Phys. Lett.* 104.251915 (2014).
- [49] M. Born and K. Huang. *Dynamical Theory of Crystal lattices*. Oxford: Clarendon Press, 1954.
- [50] G. Tsoukleri, J. Parthenios, K. Papagelis, et al. “Subjecting a Graphene Monolayer to Tension and Compression”. *Small* 5.21 (2009), pp. 2397–2402.
- [51] H. J. Conley, B. Wang, J. I. Ziegler, et al. “Bandgap Engineering of Strained Monolayer and Bilayer MoS<sub>2</sub>”. *Nano Lett.* 13.8 (2013), pp. 3626–3630.

- 
- [52] R. Roldán, A. Castellanos-Gomez, E. Cappelluti, et al. “Strain engineering in semi-conducting two-dimensional crystals”. *J. Phys. Condens. Matter* 27 (2015), p. 313201.
- [53] G. G. Naumis, S. Barraza-Lopez, M. Oliva-Leyva, et al. “Electronic and optical properties of strained graphene and other strained 2D materials: a review”. *Rep. Prog. Phys* 80.9 (2017), p. 096501.
- [54] Z. Dai, L. Liu, and Z. Zhang. “Strain Engineering of 2D Materials: Issues and Opportunities at the Interface”. *Adv. Mater.* (), p. 1805417.
- [55] M. Mužević, M. Varga Pajtler, S. K. Gupta, et al. “Enhancement of UV optical activity in two-dimensional materials under external strain”. *In preparation* (2019).
- [56] D. Roundy and M. L. Cohen. “Ideal strength of diamond, Si, and Ge”. *Phys. Rev. B* 64.212103 (2001).
- [57] F. Liu, P. Ming, and J. Li. “Ab initio calculation of ideal strength and phonon instability of graphene under tension”. *Phys. Rev. B* 76 (2007), p. 064120.
- [58] R. Qin, C.-H. Wang, W. Zhu, et al. “First-principles calculations of mechanical and electronic properties of silicene under strain”. *AIP Advances* 2 (2012), p. 022159.
- [59] B. Feng, Z. Ding, S. Meng, et al. “Evidence of Silicene in Honeycomb Structures of Silicon on Ag(111)”. *Nano Lett.* 12 (2012), pp. 3507–3511.
- [60] N. Gao, H. Liu, S. Zhou, et al. “Interaction between Post-Graphene Group-IV Honeycomb Monolayers and Metal Substrates: Implication for Synthesis and Structure Control”. *J. Phys. Chem. C* 121 (2017), pp. 5123–5129.
- [61] M. Petrović, I. Šrut Rakić, S. Runte, et al. “The mechanism of caesium intercalation of graphene”. *Nat. Commun.* 4.2772 (2013).
- [62] V. A. Milichko, A. S. Shalin, I. S. Mukhin, et al. “Solar photovoltaics: current state and trends”. *Physics-Uspekhi* 59.8 (2016), pp. 727–772.
- [63] M.L. Ould NE, A.G. El hachimi, M. Boujnah, et al. “Comparative study of electronic and optical properties of graphene and germanene: DFT study”. *Optik* 158 (2018), pp. 693–698.
- [64] C. Suman and J. Debnarayan. “A theoretical review on electronic, magnetic and optical properties of silicene”. *Rep. Prog. Phys.* 79.12 (2016), p. 126501.

- [65] B. Peng, H. Zhang, H. Shao, et al. “The electronic, optical, and thermodynamic properties of borophene from first-principles calculations”. *J. Mater. Chem. C* 4 (16 2016), pp. 3592–3598.
- [66] M. Bernardi, M. Palummo, and J. C. Grossman. “Extraordinary Sunlight Absorption and One Nanometer Thick Photovoltaics Using Two-Dimensional Monolayer Materials”. *Nano Lett.* 13.8 (2013), pp. 3664–3670.
- [67] M. Varga Pajtler, M. Mužević, S. K. Gupta, et al. “Anisotropic superelasticity in two-dimensional allotropes of indium and aluminium”. *In preparation* (2019).
- [68] Y. Z. Abdullahi, T. Leong Yoon, and T. Leng Lim. “Elastic and electronic properties of C<sub>2</sub>N monolayer: first-principles calculation”. *Materials Research Express* 6.2 (2018), p. 025601.
- [69] D. Akinwande, C. J. Brennan, J. S. Bunch, et al. “A review on mechanics and mechanical properties of 2D materials - Graphene and beyond”. *Extreme Mechanics Letters* 13 (2017).
- [70] <https://www.engineeringtoolbox.com/>. accessed on 13th of May 2019.
- [71] <https://www.azom.com/properties.aspx?ArticleID=1522>. accessed on 13th of May 2019.
- [72] <https://periodictable.com/Properties/A/YoungModulus.al.html>. accessed on 13th of May 2019.
- [73] <http://www.goodfellow.com/A/Antimony.html>. accessed on 13th of May 2019.
- [74] I. Lukačević and S. K. Gupta. “Nature of low compressibility and anisotropic elasticity in YbB<sub>2</sub>”. *J. Alloys Compd.* 597 (2014), pp. 148–154.
- [75] X. Luo, J. Yang, H. Liu, et al. “Predicting Two-Dimensional Boron–Carbon Compounds by the Global Optimization Method”. *J. Am. Chem. Soc.* 133 (2011), pp. 16285–16290.
- [76] D. R. Hamann. “Optimized norm-conserving Vanderbilt pseudopotentials”. *Phys. Rev. B* 88 (2013), p. 085117.
- [77] T. Björkman, V. Skakalova, S. Kurasch, et al. “Vibrational Properties of a Two-Dimensional Silica Kagome Lattice”. *ACS Nano* 10.12 (2016), pp. 10929–10935.

- [78] Y. Gan and H. Zhao. “Chirality and vacancy effect on phonon dispersion of MoS<sub>2</sub> with strain”. *Phys. Let. A* 380.5 (2016), pp. 745–752.



# Curriculum vitae

Matko Mužević was born on 24th of March 1990 in Osijek, Croatia. He finished primary school in Belišće, Croatia, and secondary school in Valpovo, Croatia. In 2013 he was granted MSc degree in physics and computer science from Department of Physics, Josip Juraj Strossmayer University of Osijek. In 2013 he started a PhD study in the field of Atomic and Molecular Physics at the Faculty of science, University of Zagreb. Since 2013, he has been working at the Department of Physics, Josip Juraj Strossmayer University of Osijek as a teaching assistant.

In 2018 he spent three months as a visiting PhD student at the Cardiff University, under the supervision of Prof. Nora de Leeuw, working on HPCEuropa-3 project "Optical properties of ultra-thin monoelemental semiconductors".

## List of published work

- Mužević, Matko; Varga Pajtler, Maja; Gupta, Sanjeev Kumar; Lukačević, Igor. "Modulation Of Optical Properties With Multilayer Thickness In Antimonene And Indiene". *Advanced Materials Letters*, 10 (2019), 4; 270-274
- Lukačević, Igor; Varga Pajtler, Maja; Mužević, Matko; Gupta, Sanjeev K. "Prospects for experimental realization of two-dimensional aluminium allotropes". *Journal of Materials Chemistry C*, 7 (2019) , 9; 2666-2675
- Radolić, Vanja; Miklavčić, Igor; Stanić, Denis; Poje, Marina; Krpan, Ivana; Mužević, Matko; Petrincec, Branko; Vuković, Branko. "Identification and mapping of radon-prone areas in Croatia— preliminary results for Lika-Senj and the southern part of Karlovac Counties". *Radiation protection dosimetry*, 162 (2014), 1/2; 29-33